UNIVERSIDADE ESTADUAL PAULISTA
"JÚLIO DE MESQUITA FILHO"
Campus Ilha Solteira

PROGRAM OF GRADUATION IN MATERIALS SCIENCE

STRUCTURAL AND LOCAL PHYSICAL PROPERTIES OF RELAXOR FERROELECTRIC THIN FILMS

A thesis in

Materials Science

By

2017 Michael de Melo

Submitted in Partial Fulfilment
of the Requirements
for the Degree of

Doctor of Philosophy

September 2017

Michael de Melo

Structural and local physical properties of relaxor ferroelectric thin films

Thesis presented as a partial fulfillment for the degree of Ph.D. to Sao Paulo State University "Júlio de Mesquita Filho" – Program of graduation in materials science, subarea Condensed Physics Matter, under the supervision of Professor Dr. Eudes Borges de Araújo.

Ilha Solteira - SP

September 2017

FICHA CATALOGRÁFICA
Desenvolvido pelo Serviço Técnico de Biblioteca e Documentação

M528s

Melo, Michael de.
Structural and local physical properties of relaxor ferroelectric thin films / Michael De Melo. -- Ilha Solteira: [s.n.], 2017
145 f. : il.

Tese (doutorado) - Universidade Estadual Paulista. Faculdade de Engenharia de Ilha Solteira. Área de conhecimento: Física da Matéria Condensada, 2017

Orientador: Eudes Borges De Araujo
Inclui bibliografia

1. Thin films. 2. Relaxors. 3. Piezoresponse force Microscopy (PFM).

UNIVERSIDADE ESTADUAL PAULISTA

Câmpus de Ilha Solteira

CERTIFICADO DE APROVAÇÃO

TÍTULO DA TESE: STRUCTURAL AND LOCAL PHYSICAL PROPERTIES OF RELAXOR FERROELECTRIC THIN FILMS

AUTOR: MICHAEL DE MELO
ORIENTADOR: EUDES BORGES DE ARAUJO

Aprovado como parte das exigências para obtenção do Título de Doutor em CIÊNCIA DOS MATERIAIS, área: FISICA DA MATERIA CONDENSADA pela Comissão Examinadora:

Prof. Dr. EUDES BORGES DE ARAUJO
Departamento de Física e Química / Faculdade de Engenharia de Ilha Solteira

Prof. Dr. JOSE DE LOS SANTOS GUERRA
Instituto de Física / Universidade Federal de Uberlândia

Prof. Dr. JEAN-CLAUDE M'PEKO
Instituto de Física de São Carlos / Universidade de São Paulo - USP

Prof. Dr. ANDREI LEONIDOVITCH KHOLKINE
Department of Materials and Ceramic Engineering / Universidade de Aveiro

Prof. Dr. MICHAEL TEXIER
Departement Materiaux et Nanosciences / Aix Marseille Université

Ilha Solteira, 11 de setembro de 2017

DEDICATION

I dedicate this work to my parents. My mother, Gisele, and my father, Nilton. You gave me love, taught me how to surpass hard times, and helped me to become a man of value.

ACKNOWLEDGEMENT

To my supervisor Prof. Dr. Eudes Borges de Araújo, for the teaching and for the valuable guide, either in academic and personal aspects, contributing to my development. Besides being my supervisor, I can entirely assure that just made a friend for the rest of my life.

To Dr. Andrei L. Kholkin and Dr. Igor Bdikin from Aveiro University (AU), Aveiro-Portugal, for the help with the measurements in PFM and the analysis of our relaxor ferroelectric thin films. To my colleagues Dr. Maxim Ivanov, Dr. Sergey Luchkin, Dr. Konstantin Romaniuk and Dra. Svetlana Kopyl for the support and friendship that I received during my stay in Portugal.

To Prof. Dr. Vladimir Ya Shur, Elizaveta Neradovskaya, Dra. Elena and Dr. Dmitry Pelegov, Dr. Maxim Neradovskiy and Yana Mayorova for the contribution of my work supporting me with laboratories of the Ural Federal University, in Ekaterinburg-Russia.

To all the professors of the Physics and Chemistry Department (DFQ) and in special to the Prof. Dr. Antonio Seridônio, for the guidance and support as well, and for the colleagues of the Ferroelectric Group, and in special to the Dr. Bacus Nahime.

To my friends and Professor Dr. Osvaldo Gastaldon, Professor Esp. Rivelino Rodrigues, Professor Esp. Edson Carrilho, and the Professor Esp. Rodrigo Bertolozzi. To the current rector of the FEV, Dr. Rogério Rocha Mattaruco, for the opportunity to work with science education and the possibility to initiate my investigation in physics of condensed matter.

To my parents, Nilton and Gisele Melo, for the example of persistence on tough times and love. To my brothers Alan and Yasmin Melo for being available always when I needed. To my grandmother Judair Casonato for the assistance when it was needed simple tasks and certainly helped me a lot. To my partner Bruna Yamaguti for the patience and motivation, important to conclude this work. To Felipe Santana and Diego Rico that really contributed for my complementary skills that were essential to keep motivated during this important phase in my academic studies.

To CNPq for the scholarship and UNIFEV for the financial support in my doctoral research and for the opportunity given to me to complete my Ph.D.

RESUMO

Filmes policristalinos de $Pb_{0,91}La_{0,09}Zr_{0,65}Ti_{0,35}O_3$ (PLZT9/65/35) e de $Sr_{0,75}Ba_{0,25}Nb_2O_6$ (SBN75) foram preparados por uma rotina química polimérica para investigarmos as suas propriedades em nano- e macroescala. Difração de raios-X (DRX), microscopia de força atômica de piezoresposta (PFM), e microscopia eletrônica de varredura (SEM), foram utilizados como ferramentas investigativas. Os filmes finos de PLZT9/65/35 e de SBN75 exibiram estrutura peroviskita e tungstênio bronze, respectivamente, conforme esperado à temperatura ambiente e na composição nominal para estes materiais ferroelétricos relaxores. Além disso, o refinamento de Rietveld da estrutura revelou a dependência do tamanho do cristalito e do microstrain com a espessura. A temperatura de transição de fase do filme de SBN mostrou um deslocamento para valores menores de temperatura, sugerindo a presença de concentração de defeitos, tais como vacâncias de oxigênio, desordem química e defeitos de rede, maior no filme de SBN. Microscopia eletrônica de varredura (SEM) exibiu o caráter poroso de ambos os filmes. Propriedades ferroelétricas desses filmes foram investigados por meio da técnica de PFM. A piezoresposta mostrou ter uma dependência em função do tamanho do cristalito e da espessura. Neste trabalho, a dinâmica de reversão de domínios ferroelétricos e a relaxação de domínios induzidos foram estudados por meio do uso da espectroscopia de chaveamento (SS-PFM) em ambos os sistemas em função da tensão DC e do tempo de duração do pulso.

Palavras-chaves: Filmes Finos; Relaxores; Microscopia de Força Atômica de Piezoresposta (PFM)

ABSTRACT

Polycrystalline thin films of $Pb_{0.91}La_{0.09}Zr_{0.65}Ti_{0.35}O_3$ (PLZT9/65/35) and $Sr_{0.75}Ba_{0.25}Nb_2O_6$ (SBN75) were prepared by the chemical polymeric routine in order to investigate their physical properties at the macro- and nanoscale. X-ray diffraction (XRD), piezoresponse force microscopy (PFM), and scanning electron microscopy (SEM) were used as investigative tools. PLZT9/65/35 and SBN75 thin films have exhibited perovskite and tungsten bronze crystal structure at room temperature, as it was expected in this nominal composition for these relaxor ferroelectric materials. In addition, Rietveld method of the crystalline structure has revealed the thickness dependence of the crystallite size, grain size, and microstrain. The transition temperature of SBN thin film showed to shift to lower temperatures, suggesting the presence of a higher defect concentration, such as oxygen vacancies, chemical disorder, and lattice defects in this film. SEM has exhibited the porosity features in both thin films and has confirmed the existence of chemical elements (such as oxygen, niobium, lanthanum, strontium, platinum, silicon and barium) in film surface and near the substrate. Ferroelectric properties have been investigated by PFM and the results have suggested a thickness and crystallite size dependence of the piezoelectric response. Also in this work, the dynamic of ferroelectric domain switching and the induced domain relaxation were studied using the switching spectroscopy PFM (SS-PFM) in both relaxor systems as a function of variable DC applied voltages and pulse durations.

Keywords: Thin films; Relaxors; Piezoresponse Force Microscopy (PFM)

LIST OF FIGURES

Figure 1: Relationship between piezoelectrics, pyroelectrics, and ferroelectrics. 27

Figure 2: Unit cell of a cubic structure in the paraelectric state (PE) and tetragonal structure in the ferroelectric state (FE) of the perovskite structure. 27

Figure 3: Diagram of free energy versus atomic displacement of a system. 28

Figure 4: Representative hysteretic loop between the polarization and the applied DC voltage of FE materials. (The author) 29

Figure 5: Representative behavior of the Gibbs free energy as a function of polarization and the polarization as a function of α for a given FE material with a (a) first- and (b) second-order phase transition. (Figure adapted from reference [30]) 33

Figure 6: Schematics of the operation principle of SEM 55

Figure 7: In SS-PFM, local hysteresis loop and piezoresponse relaxation can be locally collected. In (a) we can observe the single-point probing waveform in SS-PFM and the data acquisition sequence for both local piezoloops and piezoresponse relaxation. In (b) is represented a schematic behavior of a PFM hysteresis loop obtained in a FE material. 60

Figure 8: Refined structure with observed (dots), calculated (red lines), and difference (bottom lines) XRD profiles of $Sr_{0.75}Ba_{0.25}Nb_2O_6$ thin film. 63

Figure 9: (a) Scanning electron microscopy (SEM) of the SBN thin film obtained at the edge using electron bean of 3 kV with approximately 20,000x of magnification and the top view SEM images obtained with (b) 85,000x magnification. 64

Figure 10: (a) Cross-sectional SEM image of the SBN thin film and (b) the representation of the distribution of the secondary electrons respective to the specific chemical element with the chemical composition in the cross section obtained inside the rectangle drawn in (a). 65

Figure 11: Real and imaginary dielectric permittivity of SBN thin film as a function of temperature at measurement frequencies of 10, 20, 30, 60, 100, 200, 300, and 600 kHz. 67

Figure 12: Temperature dependence of the frequency of the maximum permittivity in SBN thin film. 69

Figure 13: (a) Real and imaginary part of the dielectric permittivity as a function of the frequency in the SBN thin film, and (b) the modulus of the impedance and the conductivity, respectively. The behavior of (c) dielectric permittivity and (c) dielectric loss as a function of AC amplitude for different frequencies. 71

Figure 14: (a) *P-E* hysteresis loops of the SBN thin film measured at room temperature for different frequencies and (b) the behavior of the positive and negative coercive electric field and remnant polarization as a function of frequency. 73

Figure 15: Typical topography (a) and piezoresponse (b) image of the SBN75 thin film obtained in an area of 2×2 μm^2. 74

Figure 16: Topography (a) and piezoresponse (b) images and (c) cross-sections across the grains with different domain polarization vectors of SBN thin film and the histograms of the distribution of piezoelectric response inside the grains depicted in Figure 16(a-b). 75

Figure 17: The piezoresponse histograms referent to different regions of a PFM image. 77

Figure 18: (a) Topography and analysis of the piezoresponse in SBN thin film applying (b) $V_{dc} = 0$ V (before poling), (c) $V_{dc} = +5$ V, (d) $V_{dc} = -5$ V and (e) $V_{dc} = 0$ V (after poling). (f) Cross-sectional analysis of the grain boundary between two grains indicated in (a). 78

Figure 19: (a) Piezohistogram and (b) the self-polarization factor of the respective PFM images of SBN thin films referred to Figure 18. 79

Figure 20: A 1 μm ×1 μm scan of SBN75 thin film obtained at room temperature in DART-PFM mode (a) the sample topography, (b) the resonance contact frequency (f_0), and (c), (d), (e) and (f) the experimentally measured R_1, φ_1, R_2 and φ_2, where R and φ are amplitude and phase of the DART-PFM image. $\Delta f = (f_2 - f_1) = 20$ kHz was used for these measurements. A cross-section analysis of topography and mapping resonance contact frequency [indicated along the line *ab* in Figure 20a-b] is illustrated in (g). 81

Figure 21: (a) Topography and (b) piezoresponse images of the SBN thin film. (c) Local hysteresis loops recorded at three different grains is indicated in (a) and (d) Polarization relaxation of piezoresponse as a function of time at different grains for the magnitude of ±10 V and duration of DC voltage of 100 ms. 84

Figure 22: Piezoresponse relaxation curves of SBN thin film for (a) 5 and 20 V at 100 ms of pulse duration and (b) for 0.01 s, 0.5 s, and 3 s of pulse duration at 15 V of DC voltage amplitude. 86

Figure 23: (a) Local hysteresis loops of SBN thin film at DC pulses voltages of 10 V with pulse duration t_p = 10 ms, 500 ms, and 3000 ms. (b) Pulse duration dependence of local imprint effect $S = Ec + +Ec -$ at different voltages. (c) Effective coercive field $Ec = Ec + -Ec -/2$ as a function of DC amplitude voltages, and (d) coercive electric field as a function of pulse duration for positive and negative DC pulses. (Here the lines are guides for the eyes) 88

Figure 24: (a) Positive and negative coercive electric field $\boldsymbol{Ec+}$ as a function of t_p for 15 V of a DC applied voltage, fitted with simple exponential form, given by $E_c \cong E_{0c}\exp\left(-t_p/\tau_c\right)$. (b) Fitting parameter $\boldsymbol{\tau c}$ as a function of applied voltage. (Lines are just guides to the eyes). 89

Figure 25: XRD pattern diffractions of PLZT film deposited on Pt (100)/SiO_2/Si substrates prepared for (a) different film thickness (ranging from 240 nm to 540 nm) crystallized at 700 ºC for 1h and (b) different annealing temperature for the film with 550 nm in thickness. All films were pyrolyzed at 300 ºC for 30 min [138]. 93

Figure 26: SEM micrographs exhibiting the typical morphology of mesoporous PLZT thin films after thermal treatment at 400, 500, 600 and 700 ºC, respectively. As the temperature of the thermal treatment increases, the porosity order is increased, pores become interconnected and dense areas increase as well. A well-defined grain pattern with annealing temperature characterizes the crystallized PLZT thin film. 96

Figure 27: SEM images of the PLZT thin film in (a) a wide surface and (b) an area displaying the material and the bottom electrode (Pt) in which we can see several cracks over the film surface. In (c) is possible to observe another area illustrating the boundary between the bottom electrode and two different morphology layers of the film. In (d) an approached image of the thin film shows the remaining grains that are stuck on the substrate. SEM top view of PLZT revealing the interfaces between some individual crystallization steps is shown in (e) and a SEM side view of the crystallized grains through the film can be seen in (f). 97

Figure 28: (a) SEM image of the PLZT thin film surface pointing the top electrodes and the (inset) irradiated area used to mill the sample by FIB method. SEM micrograph revealing the morphology of the cross-section of the film is shown in (b). 99

Figure 29: P-E hysteresis loops in PLZT thin film: (a) at 183 K at a frequency range from 50 Hz to 5 kHz and (b) at 1 kHz frequency at temperatures in the range 183-293 K. Temperature dependence of the differences (c) $\Delta Pr = Pr+ - Pr-$ and (d) $\Delta Ec = Er+ - Er-$ at 1 kHz frequency. Lines in (c) and (d) are drawn as a guide to the eye. 100

Figure 30: Frequency dependence of the (a) remnant polarization at 273, 223, and 183 K and (b) coercive field at 273, 223 and 183 K of temperature. Temperature dependence of the (c) remnant polarization and (d) coercive field at 1, 3 and 5 kHz frequencies. The real and imaginary impedances as a function of the frequency is shown as inset in (b). (Lines are drawn as a guide to the eye). 101

Figure 31: Topography and VPFM piezoresponse images of PLZT thin films for the thicknesses 240, 350, 430 and 540 nm, respectively. The scan size of the images is 15×15 μm^2. 105

Figure 32: (a) Thickness dependence of average grain size of studied PLZT thin films. (b) Piezoelectric histogram distribution of PLZT thin films at different thicknesses. The line in (a) is drawn as a guide to the eye while lines in (b) refer to fit curves. 106

Figure 33: Thickness dependence of peak half-width of the piezohistograms. Lines in both curves are drawn as a guide to the eye...108

Figure 34: Thickness dependence of self-polarization factor (see text) of PLZT thin films. Lines in both curves are drawn as a guide to the eye. 109

Figure 35: Autocorrelation images (scan area 15×15 μm^2) of PLZT 9/65/35 thin films for film (*a*) with 240 nm, (b) 350 nm, (c) 430 nm, and (d) 540 nm in thickness. (e) The autocorrelation function <C(*r*)> average overall in-plane directions for PLZT thin films with 240, 350, 430, and 540 nm in thickness, respectively. 112

Figure 36: Thickness dependence of correlation length of PLZT films. Lines in (a) are best fits of <C(r)> while in (b) lines are drawn as a guide to the eye 114

Figure 37: Hysteresis loops measured for PLZT thin films at a different thickness as a function of applied voltage using 1 s of the pulse duration of the DC external bias (b) and the saturated piezoresponse as a function of thin film thickness. 115

Figure 38: Hysteresis loops measured at different pulse durations for PLZT thin films with a) 240 nm, b) 350 nm and c) 540 nm of thickness. 118

Figure 39: (a) Positive and negative $\boldsymbol{d}33,r$ remnant piezoresponse signal as a function of thin film thickness for different DC pulse durations. Average remnant piezoresponse $\boldsymbol{d}33,r = Pr+ - Pr-/2$ as (b) a function of the DC pulse duration for different thin film thicknesses and (c) as a function of the film thickness for different DC pulse durations. The DC pulse duration dependence on imprint effect $Ec+ + Ec-$ is shown in (d) and the coercive electric field (E_c) dependence with thickness and pulse duration are illustrated in (e) and (f), respectively. The lines are just guides to the eyes. 119

Figure 40: Time dependences of the positive and negative induced piezoresponse measured after applying a voltage pulse of V_{dc} = 10 V and pulse duration t_p = 1s for PLZT thin films with (a) 240 nm, (b) 350 nm, and (c) 540 nm of thickness. 121

Figure 41: (a) Effective relaxation times (s) as a function of the magnitude of the applied electric field for the PLZT thin films in different thickness and (b) electric field of maximum characteristic time as a function of the PLZT thin film thickness. 121

LIST OF TABLES

Table 1: Summary of Rietveld refinement for $Sr_{0.75}Ba_{0.25}Nb_2O_6$ film obtained at room temperature. 63

Table 2: Refined Structural parameters for the PLZT thin films at 240, 350, 430 and 540 nm in thickness. ..94

Table 3: Calculated cell parameters, R-factors from Rietveld refinement, and crystallite size and microstrain obtained from WH analysis of the PLZT thin films as a function of thickness. 95

SUMMARY

ABSTRACT .... **viii**
LIST OF FIGURES .... **ix**
LIST OF TABLES .... **xii**
1. INTRODUCTION **15**
1.1. *STRUCTURAL AND PHYSICAL PROPERTIES OF RELAXOR PLZT AND SBN MATERIALS* *17*
1.2. SCOPE OF THE THESIS AND OBJECTIVES *21*
2. FERROELECTRIC AND PIEZOELECTRIC PHENOMENA IN FERROELECTRICS MATERIALS **22**
2.1. POLARIZATION IN DIELECTRIC MATERIALS *23*
2.2. FERROELECTRIC MATERIALS *25*
2.2.1. Piezoelectricity 26
2.2.2. Ferroelectricity 28
2.2.3. Thermodynamic Theory of Phase Transition Phenomena 30
2.2.4. Ferroelectric Domains 33
2.3. RELAXOR FERROELECTRICS *35*
2.3.1. Phase Transition in Relaxor Ferroelectrics 37
2.3.2. Models and Theories about origin and evolution of PNRs in relaxors 40
2.3.3. Dielectric Response in Relaxors 43
3. EXPERIMENTAL TECHNIQUES AND MATERIALS PROCESSING **48**
3.1. SAMPLE PREPARATION *48*
3.1.1. PLZT Thin Films 48
3.1.2. SBN Thin Films 50
3.2. CHARACTERIZATIONS *51*
3.2.1. X-ray Diffraction Analysis 51
3.2.2. Scanning Electron Microscopy 54
3.2.3. Dielectric Characterization 55
3.2.4. Ferroelectric Hysteresis Measurements 56
3.2.5. Piezoresponse Force Microscopy (PFM) 57
4. RESULTS AND DISCUSSION **62**
4.1. NANOPOLAR DOMAIN STRUCTURE OF RELAXOR $Sr_{0.75}Ba_{0.25}Nb_2O_6$ *(SBN) THIN FILMS* *62*
4.1.1. Macroscopic and Physical Properties of SBN Thin Films 62
4.1.2. Microstructure Analysis of SBN thin films 64
4.1.3. Electrical Properties of SBN Thin Films 66
4.1.4. Nanoscale Domain Properties in Polycrystalline Strontium Barium Niobate Thin Films 74
4.1.5. Domain Switching and Local Piezoresponse Relaxation Dynamics of SBN Thin Films via SS-PFM 83
4.1.6. Summary 90
4.2. INVESTIGATION OF POLAR STRUCTURE IN RELAXOR THIN FILM OF $Pb_{0.91}La_{0.09}Zr_{0.65}Ti_{0.35}O_3$ *(PLZT)* *92*
4.2.1. Structural Properties of PLZT thin films 92
4.2.1. Microstructure and Morphologic Analysis of PLZT thin film 96
4.2.2. Ferroelectric Properties of PLZT thin films 100
4.2.3. Effects of thickness on structural, grain size and local piezoelectric properties of self-polarized PLZT thin films 105

4.2.4. Piezoelectric Hysteresis Loops and Local Polarization Relaxation in PLZT thin films by Switching Spectroscopy PFM 115
4.2.5. Summary 123
5. FINAL CONSIDERATIONS 125
REFERENCES 126

1. INTRODUCTION

A significant scientific and technological importance have been given to the effects at the nanoscale in ferroelectric materials over the last years [1]. Ferroelectric materials are a special class of dielectric materials that exhibit a specific property called spontaneous polarization and, necessarily, must be reversible with an application of an external electric field. The ferroelectricity phenomenon has shown an intrinsic dependence on sample dimensions and have been attributed to the different high degree of ordering existing on surfaces and interfaces [2]. The complexity of this phenomenon is characterized by the stronger interaction of the polarization in ferroelectric materials than other order parameters (e.g. composition and strain) resulting in a strong dependence of the structural, mechanical and electrical properties of thin films, thickness, grain size, microstructure, and residual stress [3, 4].

Because of the growing demand for portability of electronic devices, the investigations of these effects at very small scale have been increased considerably. However, the main purpose of these investigations is to understand the size effect on the physical properties of ferroelectric materials. This comprehension is essential to promote both the advancement of the nanoscience of ferroelectric materials and to obtain the maximum performance of certain devices based on ferroelectric thin film technologies which the miniaturization process is indispensable.

Most of the advances obtained in the comprehension of the ferroelectric phenomena at the nanoscale have been done with the intention of investigating the correlation between the physical properties related to the polarization and the size effects related to the thickness below the submicron level in thin films. Several studies have been carried out in ferroelectric thin films about the relationship of the physical properties with thickness [5], sample preparation, mechanical coupling in film/substrate [6], etc. Self-polarization effects observed in ferroelectric thin films have gained remarkable attention recently. These effects were explained initially using qualitative arguments in terms of the existence of space charges related to the Schottky barriers localized near film and substrate [7], or in terms of the electromechanical coupling between the film and the substrate [8]. Other models have been proposed to explain the mechanisms responsible for the appearance of the self-polarization in ferroelectric films, but the real nature of this phenomenon is uncertain and is the object of discussion. In this context, it is clear the relevance of this study and the necessity of progress in the comprehension of the phenomenology at nanoscale of ferroelectric materials.

Ferroelectric materials have been considered very important from the technological point of view and have been widely used for the development of different devices, such as capacitors [9], piezoelectric sensors [10] and actuators [11], micromechanical devices [12], non-volatile ferroelectric memories [13], and others. The application of thin-film nanoscale devices integrated onto Si chips have ignited the semiconductor industry [14]. These applications include ultrafast ferroelectric switching on femtosecond timescale [15], cheap room-temperature magnetic-field detector based on ferroelectric material [16], piezoelectric nanotubes for microfluidic systems [17], and three-dimensional trenched capacitors for dynamic random access memories [18]. However, from the scientific point of view, several questions remain unclear, especially those related to the effects at nanoscale due to the miniaturization process. Among the ferroelectric materials with great scientific and technological interest are the "*relaxor*" (RE) ferroelectrics [19]. RE materials are a special class of ferroelectrics in which a disorder is either introduced into the system by doping with different size and valence ions or is an intrinsic disorder, in order to maximize their useful properties in a wide range of temperature [20].

A typical characteristic of these materials is that at least two different cations have to be localized in the same crystallographic site [21]. Since their discovery in 60's [22], probably the RE ferroelectrics are the most interesting materials studied in solid state physics due to its exceptional dielectric and electromechanical properties. Unlike conventional ferroelectrics (barium titanate, represented by $BaTiO_3$, is a classic representative) which dielectric, ferroelectric, and piezoelectric properties are convincingly described by a phenomenological theory [23], RE materials exhibit peculiar features. Among these features, one can mention the diffusivity of dielectric permittivity near temperature of maximum (T_m), the absence of both macroscopic spontaneous polarization and structural symmetry breaking, pronounced non-ergodicity, and the existence of a dipolar glass behavior at low temperature [24]. Even though with these specific characteristics, notable piezoelectric properties arise because of the ferroelectric phase that develops in the RE material, especially in solid solutions after application of a strong enough electric field [25]. The dynamics of the polar nanoregions (PNRs) [26] under the influence of an external electric field have been one of the main mechanisms used to explain the dielectric and piezoelectric peculiar behavior of the RE ferroelectric materials. Nevertheless, the PNRs existence is still under discussion in the scientific community and the "*relaxor enigma*" has become one of the non-solved issue and opened to the debate.

Though several theories, supported by experimental results have been proposed, none of them can explain fully all properties of the RE ferroelectrics. Therefore, there are doubts concerning what type of dielectric relaxation qualifies a FE material as a "*relaxor*" one [19]. In addition, another fact to be considered is that the models proposed, which will be described in the next sections, inevitably fail at the nanoscale and, probably, there is a complicating factor related to the size reduction that cannot be neglected at this dimensional level [27]. With the advances of new experimental techniques, such as piezoresponse force microscopy (PFM) has been possible to map the polarization and main piezoelectric parameters on the surface of RE ferroelectrics within nanometer resolution [28]. Accessing the local properties, the origin of the relaxor phenomena and the correlation with the physical properties at the nanoscale of the ferroelectric thin films can be investigated using a new approach.

This work aims at detailed investigation of the size effects on the physical properties of the relaxor ferroelectric thin films. The RE materials studied here are the $Pb_{1-x}La_x(Zr_yTi_{1-y})_{1-x/4}O_3$ (PLZT) and $Sr_xBa_{1-x}Nb_2O_6$ (SBN) systems. The main purpose of this thesis is to contribute to the better comprehension and understanding of the relaxor phenomena origin from studies of the different physical properties at macroscale and from mapping of the piezoelectric properties at the nanoscale.

1.1. STRUCTURAL AND PHYSICAL PROPERTIES OF RELAXOR PLZT AND SBN MATERIALS

Introduction to SBN thin films

Ferroelectrics are essential components in a wide spectrum of applications. In thin film form, ferroelectrics and other polar materials are used for novel types of non-volatile memories, also being developed for various sensor and actuator applications as well as for tuneable microwave circuits [29]. Historically, ferroelectric thin films for piezoelectric applications have been formulated from a number of compositions and solid solutions including $BaTiO_3$, $PbTiO_3$, PbN_2O_6, $NaNbO_3$, PZT, and PLZT [30]. FE materials generally used in many types of detectors are mainly lead-based, such as lead titanate (PT)-based [31], lead zirconate titanate (PZT)-based [32] and lead magnoniobate (PMN)-based [33], due to its relative superior pyroelectric properties.

However, lead-based materials contain toxicity that can bring a serious concern to the health during manufacturing processing due to the lead evaporation as well as after be making the device, referring to the disposal in the nature [34]. Therefore, the development of lead-free

based materials for replacing the lead-based ones is of fundamental interest in various applications. In view of this, the ferroelectric strontium barium niobate ($Sr_xBa_{1-x}Nb_2O_6$, $0.2 < x < 0.8$) is an attractive material because it is a lead-free relaxor ferroelectric.

Due to its excellent piezoelectric, pyroelectric, electro-optic, photorefractive and non-linear optical properties, SBN is considered quite useful in different device applications [35, 36]. These niobates have structures related to the structure K_xWO_3, *i.e.*, tetragonal potassium tungsten bronze, also referred as TTB structure [37]. This type of structure consists of a framework of BO_6 octahedra, (in this case, $B = Nb^{5+}$) sharing corners so that this configuration results in three types of interstitial sites (A_1, A_2, and C sites) that can accommodate various metal atoms (different cations) with a general formula $(A_1)_2(A_2)_4(C)_4(B_1)_{12}(B_2)_{28}O_{30}$. The $Sr_xBa_{1-x}Nb_2O_6$ possess the TTB structure in space group P4bm at room temperature, with A2-sites being filled only by Ba^{2+} ions and both Ba^{2+} and Sr^{2+} ions occupying A1-sites, while in C-sites there is no occupancy [38]. Since there are six positions to be occupied in the A sites, one position remains unoccupied, being consequently responsible for a charge disorder in the structure [39]*.

RE ferroelectric materials are disordered crystals that display a broad phase transition and the temperature T_m of the maximum of dielectric permittivity $\varepsilon'(T)$ is strongly frequency-dependent. This transition does not necessarily connects to any macroscopic changes in the structure [40]. SBN is quite often used as a model of RE ferroelectric for experimental and theoretical investigations due to high crystal quality and simple domain structure [41].

The properties of SBN are very sensitive to the Sr^{2+}/Ba^{2+} molar ratio, as this molar ratio significantly influences the shift of the Curie temperature [42]. Cell dimensions decrease with increasing Sr^{2+}/Ba^{2+} ratio due to the smaller atomic radius of Sr^{2+} from $\{a = b \approx 12.48$ Å, $c \approx 3.98$ Å$\}$ when $x \approx 25\%$ to $\{a = b \approx 12.43$ Å, $c \approx 3.91$ Å$\}$ when $x \approx 75\%$ at room temperature [42]. The gradual reduction between the room and the Curie temperature is also observed with increasing Sr^{2+} content in the SBN solid solution, thus inducing a considerable increase in the dielectric permittivity, pyroelectric coefficient, and nonlinear optical properties. High values for the electro-optical coefficients were obtained for the composition with x = 75% [43, 44, 45].

The growing demand for size reduction in electronic and other integrated devices has encouraged the investigations of SBN materials in thin films form. In addition, such research on SBN thin films will allow a better understanding of the influence of size effects, defects, and

---

* For any additional information about the tungsten bronze structure of SBN material, please check Figure 1 from Ref. [283].

other extrinsic factors in their properties. Investigations at the nanoscale have already shown a distinctive correlation between grain size and physical properties of ferroelectric thin films [46]. These size effects are understood as changes of the material properties due to the change of their geometrical dimensions [47]. FE thin films are grown on substrates, which can also induce a large strain due to lattice mismatch and difference in thermal expansion coefficients [48]. In this way, thin films cannot be considered as an isolated system made solely of the ferroelectric film, rather the entire system of film, interfaces, electrodes, and substrates. Interface effects can be pronounced in thin films rather than bulk parent material, due to the influence of strain and formation of non-switching layers that significantly affect the physical properties as the film thickness decreases [49, 27].

In this context, SBN thin films at x = 75% have been prepared using the polymeric method in order to investigate the physical properties that can be tailored by this method using different characterization techniques.

Introduction to PLZT thin films

Lead zirconate titanate materials $Pb(Zr,Ti)O_3$ (PZT) of perovskite-type ABO_3 are quite known for their good piezoelectric properties and are ideal candidates for use as position sensors and actuators. In addition, PZT materials are generally used with a dopant, a modifier, or chemical constituents to improve and to optimize their physical properties for specific applications. Examples of these additives include an addition of SiC particle, ZrO_2 fibers and reinforcement with nanoscale particles to the PZT materials to improve their mechanical properties [50, 51]. The addition of Nb and Li atoms can also be helpful in both the dielectric and piezoelectric properties of PZT-based FE materials [52, 53].

Solid solutions of La-modified lead zirconate titanate, called here PLZT, with the La concentration between 5 and 14% and the Zr/Ti molar ratio of 65/35 are indeed RE ferroelectrics in a range of temperature [54, 55]. PLZT with La 9% content has been known due to their notable dielectric and piezoelectric properties that make these materials promising for several technological applications [56]. Due to their pronounced electro-optic properties and ability to be fully transparent, PLZT-based FE materials become rather useful for optical and photonic devices [57]. The relaxor properties found in PLZT materials are interesting, being responsible for their super dielectric, electro-optic, and electromechanical performance. Besides, PLZT are considered to be of theoretical interest [58] due to their large remnant

polarization (P_r), relatively small coercive field (V_c), and high relative permittivity (ε) [49] when compared with other FE materials.

The crystal structure of the PLZT family is a nearly cubic perovskite ABO_3 and can be viewed as interconnected BO_6 octahedra, where the B-site cations are inside the octahedra and the A-site cations are in between [59]. As the composition ratios of Zr/Ti and Pb/La are varied, a rich variety of structural distortions far from the cubic perovskite takes place. Replacing lead with lanthanum in PZT results in the relaxor behavior over narrow ranges of La composition that depends on the Ti/Zr ratio [60]. The La doping in PZT structure prevents the coupling of ferroelectrically active TiO_6 octahedra, breaking of the ferroelectric network into micro and nanodomains.

Due to the variation in the degree of coupling within the region, these ferroelectric microdomains are responsible for the distribution of the Curie temperatures, thus being responsible for a diffuse behavior of the macroscopic ferroelectric transition [59].When La is added to PZT, the charge neutrality is preserved by creating Pb vacancies, one vacancy for every two La atoms. The role of La in the development of the relaxational feature is likely due to the breaking the translational symmetry of the polarization within the FE domains, either by compositional disorder or by the electric field related to the defect structure [60].

1.2. SCOPE OF THE THESIS AND OBJECTIVES

In Chapter 2 of this thesis, there will be an introduction to the ferroelectric and piezoelectric phenomena in FE materials, presenting the theory about the ferroelectric and piezoelectric phenomena, the thermodynamic theory of the phase transition, and an introduction to RE ferroelectrics. In Chapter 3 we will present the experimental techniques and materials processing used in this thesis. Sample preparation of PLZT and SBN systems (nominal composition $Pb_{0,91}La_{0,09}(Zr_{0,65}Ti_{0,35})O_3$ and $Sr_{0,75}Ba_{0,25}Nb_2O_6$) and a very brief introduction about the techniques to characterize the samples, such as x-ray diffraction (XRD), scanning electron microscopy (SEM), dielectric characterization, ferroelectric hysteresis measurements, and piezoresponse force microscopy (PFM) are discussed. In Chapter 4 the results and discussion related to the PLZT and SBN thin films will be presented through the investigation of the local domain structure by PFM and correlation with physical properties at the macro scale (e.g. dielectric, ferroelectric, piezoelectric, and structural properties). The microstructure of both relaxor ferroelectric systems as a function of the annealing temperature was performed in order to study the effect of mesoporosity in the film. Visualization and manipulation of nanosized domains using PFM in the PZT-based system have been extensively studied during recent years [61]. However, the thickness effect on structural, grain size and local piezoelectric properties is not well understood yet in PLZT and SBN thin films. Furthermore, the switching properties of local ferroelectric domains in these films are investigated as a function of film thickness and for variable DC voltage pulses and different pulse durations. These investigations have the objective to contribute effectively to the understanding of the size effects on the physical properties (for example, structural, microstructural, mechanical, dielectric and piezoelectric properties) and contribute to the comprehension of the origin of the relaxor phenomena and the local polarization dynamics at the nanoscale in relaxor ferroelectric thin films.

2. FERROELECTRIC AND PIEZOELECTRIC PHENOMENA IN FERROELECTRICS MATERIALS

One of the most important groups of functional materials are ferroelectrics – a special class of dielectrics [62]. In general, most of the materials are divided in two large classes: conductors and insulators, which are also called dielectrics [63]. Dielectrics are the materials in which an electrostatic field can persist for a long time. This kind of material is quite different from metal, semiconductor, and superconductors due to its high resistance to the passage of direct current. Indeed, it is well known that the dielectric properties of materials depend on their composition, structure, and experimental conditions.

Crystalline dielectrics, in which polarization can be induced by an external electric field, are classified in polar dielectrics (or electric dipoles) and non-polar dielectrics (without net polarization).While in polar dielectrics a permanent polarization, described as P_S, exists even in the absence of an external force, in non-polar dielectrics there is no such permanent polarization [64]. Dielectrics are a group of materials that possess electric polarization when applied with external electric field and have the ability to store the charges. These materials have low electrical conductivity and they are consequently called insulators.

A very large range of non-metals is referred to as dielectrics when we take into account their interaction with electric, magnetic, or electromagnetic fields. Distinct dielectric properties are the storage and dissipation of electric and magnetic energies, polarization, and conduction [30]. Polarization and magnetization are defined as the electric and magnetic dipole moment per unit volume. The electrical properties of dielectric materials can be expressed in terms of some specific parameters, e.g. relative permittivity, displacement vector, and polarization vector.

The relative permittivity ε_r of a dielectric material is the relation between the electric permittivity of the medium ε and the electric permittivity of the free space ε_0, that is given by

$$\varepsilon_r = \frac{\varepsilon}{\varepsilon_0}. \tag{1}$$

The relative permittivity, that is typically frequency dependent, is a dimensionless number and it is in general a complex-valued, i.e.,

$$\varepsilon_r(\omega) = \varepsilon_r'(\omega) + i\varepsilon_r''(\omega), \tag{2}$$

where $\varepsilon_r'(\omega)$ and $\varepsilon_r''(\omega)$is the real and imaginary parts [65]. The measurement of the relative permittivity yields the properties of the dielectric material and indicates how easily a material can become polarized by the application of an external electric field. Sometimes, it is

convenient to use the relative permittivity as a function of the electric susceptibility to describe the dielectric properties, as follows

$$\varepsilon_r(\omega) = 1 + \chi(\omega), \tag{3}$$

where $\chi(\omega) = N\alpha(\omega)/\varepsilon_0$ is the electric susceptibility, N is the number of atoms (molecules) per unit volume and $\alpha(\omega)$ is the polarizability, that is also frequency dependent.

The displacement vector D is defined as the surface density of free charges. For a given charge Q located on parallel plates of a condenser, where A is the area of the each plate, we have

$$\vec{D} = \frac{Q}{A}\hat{n}, \tag{4}$$

where $\hat{n}$ is the unit vector pointed in the direction from the positive to the negative charges. Likewise, the electric field applied between the plates is related to the displacement vector as follows

$$\vec{D} = \varepsilon_0\vec{E} + \vec{P}. \tag{5}$$

The polarization vector P is defined as the amount of surface charge density of bound charges for the plate of area A, being given by

$$\vec{P} = \left(\frac{Q_b}{A}\right)\hat{n}, \tag{6}$$

where $\hat{n}$ here is the unit vector that is pointed from negative to positive induced charges, and d is the distance that separates the parallel plates.

2.1. POLARIZATION IN DIELECTRIC MATERIALS

The application of an external electric field to dielectric materials can create or realigns the dipoles, resulting in a polarization process. A dielectric material consists of atoms or molecules that giving rise to one or more of five basic types of electric polarization, that is: electronic polarization (or optical polarization); atomic (or ionic) polarization; orientational polarization; spontaneous polarization; and space charge polarization.

The electronic polarization (it can be as well optical polarization) arises when an application of an external electric field causes a deformation of the electronic distribution in atoms. This polarization is the displacement of the outer electron clouds with respect to the inner positive atomic cores.

The atomic polarization (or also called ionic polarization) occurs when the electric field causes a distortion of the original lattice, causing the atoms or ions of polyatomic molecules to be displaced relative each other.

The orientational polarization is a type of polarization which occurs only in a material consisting of molecules or particles that contain permanent dipole moments. The directions of these permanent dipole moments are randomly distributed inside of the material. The application of an external electric field can cause a reorientation of the dipoles toward the direction of the external field. After its removal, the net polarization in the bulk material will return to zero due to the thermal agitation that tends to randomize the dipole alignment. This is the explanation of why polarization decreases with increasing temperature.

Spontaneous polarization is another kind of polarization that occurs in materials whose crystalline structure exhibits some electrical order, meaning that spontaneous polarization occurs in single crystals or crystallites in polycrystalline materials with non-centrosymmetric structures. These are essentially structures in which the centroid of the negative charges does not coincide with that of positive ones. In ferroelectric materials, electric polarization occurs spontaneously due to a phase transition at a specific critical temperature, called Curie temperature T_c, without the aid of an electric field. Details of ferroelectric materials and its properties will be given further.

The space charge polarization is also very important kind of polarization mechanism that can occurs in dielectric materials. While the electronic, orientational, and spontaneous polarizations are due to the bound positive and negative charges within the atom or molecule itself, an electric polarization that can occur may also be associated to mobile and trapped charges. This kind of polarization is called space charge polarization and mainly occurs in amorphous or polycrystalline solids or in materials containing electron or hole [66]. In this way, charge carriers, such as electrons, holes or ions, may be trapped in the volume or at the interfaces [67]. The main effect of space charges is to distort the field distribution and consequently the average of the relative permittivity [30]. The space charge polarization can occurs in two possible ways: either through hopping polarization or interfacial polarization. The hopping polarization is described as a jump from one site to the neighboring one of localized charges, such as ions, vacancies, or electrons and holes [68]. The interface polarization is produced by the separation of the mobile charged particles under an external field, modifying as well the electric field distribution and affecting the dielectric properties of materials [69].

2.2. FERROELECTRIC MATERIALS

Ferroelectricity is a phenomenon whereby some crystals necessarily exhibit a spontaneous dipole moment that can be reverted under strong enough external electric field. A ferroelectric material is an insulating system with two or more discrete stable or metastable states of different nonzero electric polarization in zero applied electric field, referred as spontaneous electric polarization that can be reversed or reoriented between these states by an application of an external electric field [70]. A necessary criterion is the requirement of a spontaneous polarization with the exigence of reversibility or reorientation, being a sufficient criterion for a ferroelectric phase.

Ferroelectric crystals have been known for almost a century ago. The discovery was predated by the occurrence of two related phenomena that are piezoelectricity and pyroelectricity. The Jacques and Pierre Curie first discovered that putting force on certain materials could create electricity [71]. The name piezoelectricity comes from *piezein*, which means *squeeze* in Greek*. The brothers also have studied a relationship between temperature and surface charge intensity called pyroelectricity (from the Greek *pyr*, fire, and electricity). Though the Curie brothers did not predict the inverse phenomenon, that is the deformation under an electric field, it was just in 1881 after Lippmann calculations that they quickly completed the experiments and showed that converse piezoelectric effect was indeed present. In 1894, Pockels reported a large piezoelectric coefficient of Rochelle salt ($KNaC_4H_4O_6 \cdot 4H_2O$). Elie Seignette, an apothecary in La Rochelle, France, apparently first manufactured this material in 1665. The ferroelectricity in this salt was just discovered in 1917 by A.M. Nicholson, J.A. Anderson and W.G. Cady [72]. Later on, J. Valasek [73] verified the existence of ferroelectric hysteresis loops in Rochelle salt crystal and made the first analogy to magnetism. In 1935, the horizons were meaningly broadened by Busch and Sherrer's report of the occurrence of ferroelectricity in potassium dihydrogen phosphate (KH_2PO_4 - shortly named as KDP), and other crystals of the same family structure [74]. The discovery of ferroelectricity in barium titanate ($BaTiO_3$) brought a significant progress with the first ferroelectric material structure without hydrogen bonds and first ferroelectric material with more than on ferroelectric phase [75]. Ceramic materials were found very stable and hard with a simple perovskite crystal structure that facilitated the theoretical progress at the microscopic level. Many novel materials have been discovered since the 1960s, and researche focused on most promising materials, such as the perovskite and tungsten bronze structure oxides. The improvement of thin film deposition

* Further readings about the seminal articles can be found in ref. [278, 279].

techniques was essentially important for the development of ferroelectric thin film, mainly in the 1960s when progress in integrated Si devices triggered the interest of application in non-volatile memories [29].

The name of ferroelectricity comes from the similarity of the fundamental concept of ferromagnetic materials. In this kind of materials, there are the concepts of magnetization, magnetic domains, and magnetic hysteresis loops. Despite the similarity between both ferroelectric and ferromagnetic phenomena, the physics behind them are completely different. While in magnetism is explained by intrinsic quantum mechanics, ferroelectricity is, in general, described by means of classical physics.

2.2.1. Piezoelectricity

The piezoelectric effect is related to the charge asymmetry about the center of a unit cell. A unit cell is the smallest atomic structure that is repeated periodically throughout the crystalline structure, still exhibiting the crystal symmetry [76].

There are 21 classes of crystals that to not have a center of symmetry, with 20 of them being piezoelectric [30]*. Depending on the symmetry of the piezoelectric crystal class, the tensors of dielectric permittivity, elastic compliance, and piezoelectric constants are different†. Indeed, all the ferroelectric materials are piezoelectric and pyroelectric, whereas not all piezoelectric materials exhibit polar properties (Figure 1).

All ferroelectrics are indeed piezoelectric. Piezoelectricity is the ability of some crystalline materials to exhibit electric charge proportional to the mechanical stress [77]. This is often called direct piezoelectric effect. This kind of materials also shows a converse effect, in which the deformation is produced by application of an electric voltage. The direct and the converse piezoelectric effects can be expressed in tensor notation, given by

$$P_i = d_{ijk}\sigma_{jk} \text{ (direct piezoelectric effect)} \quad (7)$$

$$x_{ij} = d_{kij}E_k \text{ (converse piezoelectric effect),} \quad (8)$$

where P_i is the polarization resulted from the applied stress σ_{jk}, and the $d_{ijk}\left(= d_{kij}\right)$ is the piezoelectric coefficient. In the case of the converse piezoelectric effect, x_{ij} is the strain resulted in a specific displacement of the crystal in response to the applied electric field E_k.

* The remaining non-piezoelectric class is due to the combination of other symmetry elements.
† The piezoelectric effect *is not exclusive* of crystalline materials.

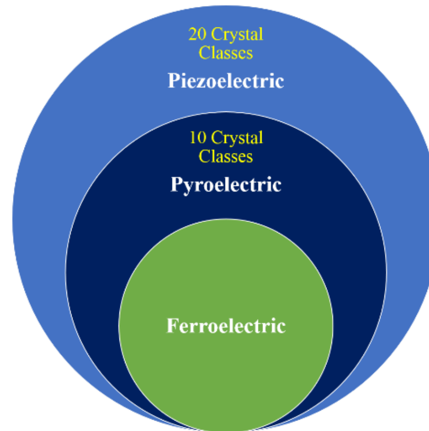

Figure 1: Relationship between piezoelectrics, pyroelectrics, and ferroelectrics.

In order to visualize the symmetry changes in crystal structure, Figure 2 illustrates a schematic representation of a cubic and tetragonal unit cell. The cubic unit cell is non-piezoelectric (also referred as the paraelectric phase) and is found above the material specific Curie point [78]. As the material cools down through the Curie point, a spontaneous polarization, P_s, is formed due to a phase transition into the tetragonal symmetry. The tetragonal structure enables six possible spontaneous polarization directions along the principal axes [79].

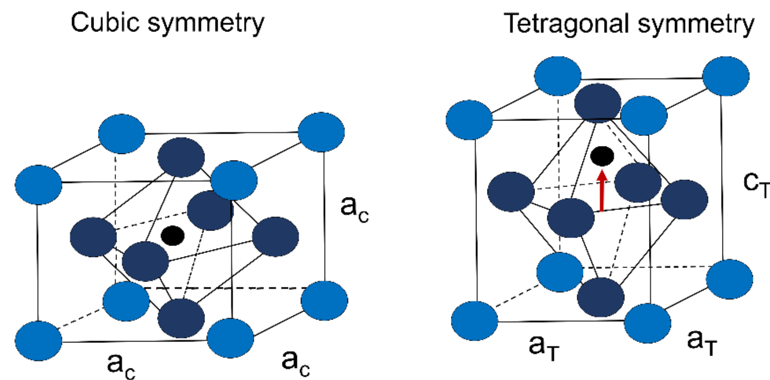

Figure 2: Unit cell of a cubic structure in the paraelectric state (PE) and tetragonal structure in the ferroelectric state (FE) of the perovskite structure.

For instance in the case of the $PbTiO_3$ material, the spontaneous polarization is associated with an ionic displacement (Figure 2). The dipole moment originates from the Ti ion displacement within the oxygen octahedral due to the minimization of the free energy as the materials experience the structural phase transition from symmetrical to asymmetrical phase.

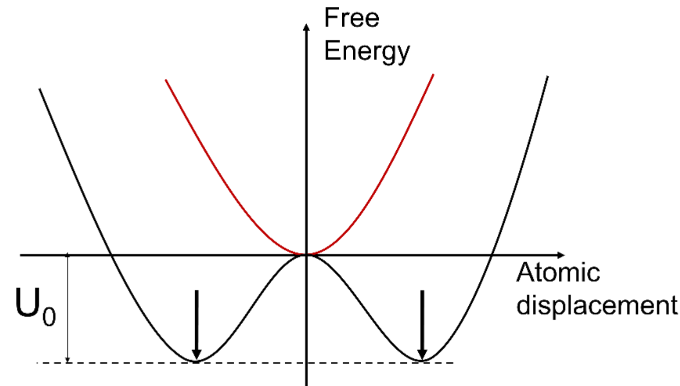

Figure 3: Diagram of free energy versus atomic displacement of a system.

The diagram of energy versus polarization for both possible states (PE - paraelectric and FE - ferroelectric state) can be seen in Figure 3. In the case of the material being in FE phase, there exist two equal energy minima (indicated in Figure 3 by two arrows) for the system with having equal, but opposite, polarizations. When the ferroelectric material is in the FE phase either of these configurations is energetically more stable than a non-polar configuration where $P = 0$ [80]. The presence of two or more stable polarization states, the ability of polarization switching by application of an external electric field, and the small domain wall width are beneficial for the high storage densities for applications in FE-based systems [81].

2.2.2. Ferroelectricity

FE materials are a subgroup of the piezoelectric materials. This class of materials has a spontaneous polarization within some temperature range and the ability to reorient (i.e. switch) their polarization by application of an external electric field [82]. A net remnant polarization can be produced in a multidomain FE material by application of an external DC voltage larger than the coercive field (this process is defined as poling). Domains are defined as specific regions in which there is only one spontaneous polarization direction. The boundary between two adjacent domains is called a domain wall. The motion of FE domain walls is important in the reorientation of spontaneous polarization in FE materials.

A reorientation of unit cells in an unconstrained ferroelectric single crystal by poling results in a translation of domain walls. Polarization reorientation within one phase may be induced by either application of stress (ferroelastic switching) or electric field (ferroelectric switching). In polycrystalline materials, the reorientation of ferroelectric domains is more complex. In these materials, each of the randomly oriented grains is a constrained single crystal subjected to local stress and electric field due to grain boundaries and local inhomogeneities.

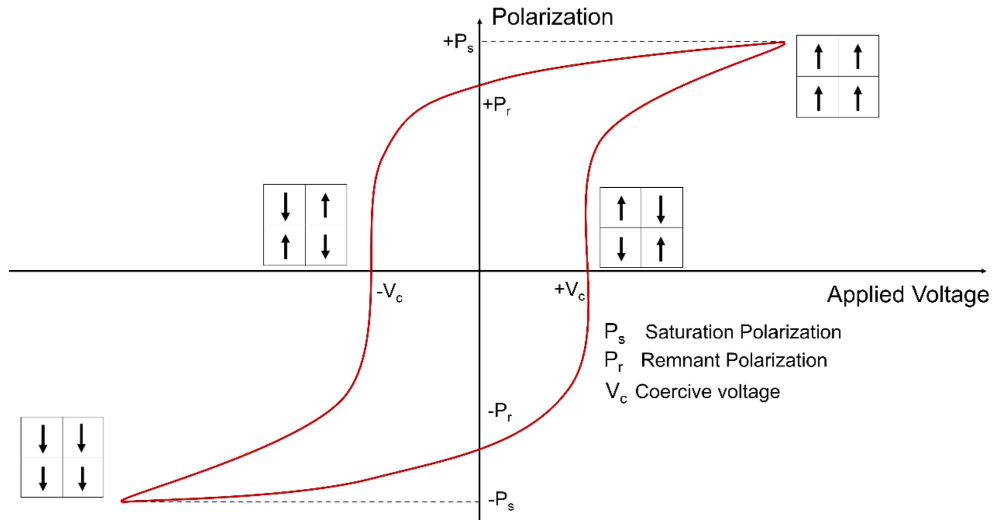

Figure 4: Representative hysteretic loop between the polarization and the applied DC voltage of FE materials. (The author)

The ability to switch the spontaneous polarization direction is the reason for the hysteretic relationship between the polarization and the external applied voltage (Figure 4). This feature is the main difference between normal (linear) dielectrics and FE materials. Even in absence of the external electric field, there is a finite polarization that is called remnant polarization, described as P_r, and the voltage, at which the net polarization is null, is called coercive voltage V_c.

When the FE material is nearby the Curie temperature, physical properties (such as dielectric, elastic, optic and thermal properties) show anomalies and the structure becomes unstable [83]. The relative permittivity, for example, in most ferroelectric crystals, has a very large value near their Curie points, and this phenomenon is often called the "dielectric anomaly". FE materials undergo a structural phase transition from high temperature non-ferroelectric phase (i.e. paraelectric (PE) phase) to low-temperature FE phase. This transition is a consequence of lowering the total free energy of the system. The temperature at which occurs the first transition (in the case of more than one transition) to a FE phase occurs is called Curie temperature (T_c). The dielectric permittivity follows the Curie-Weiss law, given by the relation

$$\varepsilon = \varepsilon_0 + \frac{C}{(T - T_0)} \tag{9}$$

where ε is the permittivity of the material, C is the Curie constant, and T_0 is the Curie-Weiss temperature. Because the term ε_0 is by far smaller than $C/(T - T_0)$ one, when $T \approx T_c$, we can neglect the temperature independent term. It is worth to notice that in the case of a first-order phase transition, the transition temperature is lower than the Curie temperature, i.e., $T_0 < T_c$.

However, in the second-order phase transition, we have that $T_0 = T_c$. The thermodynamic theory of the ferroelectric phase transition will be presented further in the next section.

2.2.3. Thermodynamic Theory of Phase Transition Phenomena

Twenty years after discovering the ferroelectricity in Rochelle salt by Valasek in 1920, the mechanism of ferroelectricity has remained a mystery. The very first model proposed to explain the ferroelectricity was made by Slater [84] and Takagi [85], independently, in KDP crystals. With the discovery of the ferroelectricity in $BaTiO_4$, Slater has proposed a model of Ti^{4+} ion displacement [86]. At the same time, Devonshire developed a phenomenological theory of the ferroelectricity based on Landau-Ginzburg of second-order phase transition to explain the phase transition of FE materials [23].

Phase transition is the transformation of a material from one thermodynamic phase to another one, which is followed by either an abrupt or gradual change of certain physical properties under the change of external parameters (such as temperature). The crystal structure of many dielectric materials change with temperature, i.e., they undergo a phase transition. The phase transition in crystals is mainly due to the changes in the interaction between atoms. The phase transition that produces or alter the spontaneous polarization is described as a ferroelectric phase transition (FPT). The FPT can be classified into two main categories: first- and second-order. In first-order phase transition, parameters such as entropy, volume, polarization, and structural parameters change discontinuously at the transition point, whereas in second-order phase transition these parameters change continuously.

Landau successfully explained the FPT by means of the thermodynamic theory [87]. In this theory, known as Landau theory of the phase transition, the behavior of a FE crystal can be obtained by considering the expansion of the Gibbs free energy as a function of the order parameter. By choosing the polarization P as the order parameter, it is convenient to treat the FPT using the uniaxial Gibbs free energy density (G) as a characteristic function of the FE system, given by the expansion

$$G = G_0 + \frac{\alpha}{2}P^2 + \frac{\beta}{4}P^4 + \frac{\gamma}{6}P^6 - EP, \tag{10}$$

where G_0 is the free energy density of the PE phase (considering $E = 0$), E is the electric field, and the expansion coefficients α, β, γ are in general temperature and pressure dependent [83]. These constants are found to be positive in all known ferroelectrics, while β can assume either positive and negative value depending on if the phase transition is of first- or second-order. The

odd terms were omitted due to the fact that the free energy can not be altered by polarization reversal.

The stable states of a thermodynamic system are characterized by the minima values of the free energy *G*, given by the conditions shown in Eq. (11.a) and (11.b). In order to obtain the electric susceptibility, it is necessary to differentiate the polarization with respect to the applied electric field, as it is described in Eq. (11.c),

$$\partial G / \partial P = 0 \tag{11.a}$$

$$\partial^2 G / \partial P^2 > 0, \tag{11.b}$$

$$\partial E / \partial P = \chi^{-1}. \tag{11.c}$$

In Landau-Ginzburg theory of second-order, the expansion coefficients of the Eq. (10) have the following values given by Eq. (12-14),

$$\alpha = \frac{1}{\varepsilon_0 C}\left(T - T_0\right) \tag{12}$$

$$\beta > 0 \tag{13}$$

$$\gamma = 0, \tag{14}$$

with $T_0 > 0$ (Curie temperature), $C > 0$ is the Curie-Weiss constant, and ε_0 is the electric permittivity of the vacuum. With the application of the equilibrium conditions given in Equations (11), and the values of the coefficients in Equations (12-14) to the free energy expansion [Equation (10)], we obtain the spontaneous polarization in FE phase, i.e.,

$$P_s = P(E = 0) = \pm\sqrt{-\frac{\alpha}{\beta}} = \pm\sqrt{-\frac{1}{\beta\varepsilon_0 C}\left(T - T_0\right)}, \quad T < T_0 . \tag{15}$$

The equilibrium temperature of transition from PE to FE phase is $T_c = T_0$. The signs "±" indicate both spontaneous polarization direction, corresponding to the two energetically equivalent states of the FE material at $E = 0$ (indicated by two arrows in Figure 3).

First-order phase transition is followed by a small jump of the order parameter *P*. In this case, it can be described by the free energy expansion with a $\beta < 0$ and ignoring terms higher than the sixth order of the expansion (P^6). Then, the Gibbs free energy becomes

$$G = G_0 + \frac{\alpha}{2}P^2 - \frac{|\beta|}{4}P^4 + \frac{\gamma}{6}P^6 \tag{16}$$

with $E = 0$. The minimum of *G* is obtained equating the condition used in Equation (11) to zero, i.e.

$$\alpha P - |\beta| P^3 + \gamma P^5 = 0 \,, \tag{17}$$

with solutions given by

$$P = 0$$

and . (18.1)

$$P = \pm \left(\frac{|\beta| \pm \sqrt{|\beta|^2 - 4\alpha\gamma}}{2\gamma} \right)^{1/2} \tag{18.2}$$

Worthy to notice that if the FE material is at the transition point, i.e., for $T = T_c$, we have that $P = \pm \left[\left(|\beta| \pm |\beta| \right) / 2\gamma \right]^{1/2}$, implying that the polarization P changes discontinuously from $P = +\left(|\beta| / \gamma \right)^{1/2}$ to $P = -\left(|\beta| / \gamma \right)^{1/2}$ or $P = 0$ abruptly at $T = T_c$, and the transition is considered to be of first order. However, if the term $|\beta|^2 - 4\alpha\gamma$ is null, we obtain another transition temperature given by $T_1 = T_0 + |\beta| \varepsilon_0 C / 4\gamma$, with $T_1 > T_0$ due to the second term be positive. In this case, we have that the spontaneous polarization can assume the values $P = \pm \left(|\beta| / 2\gamma \right)^{1/2}$ (considered unstable) and $P = 0$.

Figure 5 shows the schematic curves of the Gibbs free energy (G) as a function of the polarization for the first- and second-order phase transitions for FE materials. These curves are related to different temperature ranges, because α is a linear function of temperature, as we can see in the Equation (12).

Considering an application of an external electric field (i.e. applying a small ac field) and using the first-order approximation of the Gibbs free energy function expanded in power series of the polarization [Eq. (10)], we can obtain the *Curie-Weiss* relation, which describes the behavior of the electric susceptibility. Consequently, differentiating the Gibbs function relative to P,

$$E = \frac{dG}{dP} = \alpha P = a(T - T_c)P \,, \tag{19}$$

and P for $T > T_c$ is given by $P = (\varepsilon_r - 1)\varepsilon_0 E = \chi \varepsilon_0 E$. From Equation (12),

$$\chi^{-1} = a\varepsilon_0 (T - T_c) = \frac{(T - T_c)}{C}, \tag{20}$$

where $C = (a\varepsilon_0)^{-1}$. The temperatures $T_0, T_c, T_1,$ and T_2 are series of special temperatures that characterizes the transition from FE to PE phase.

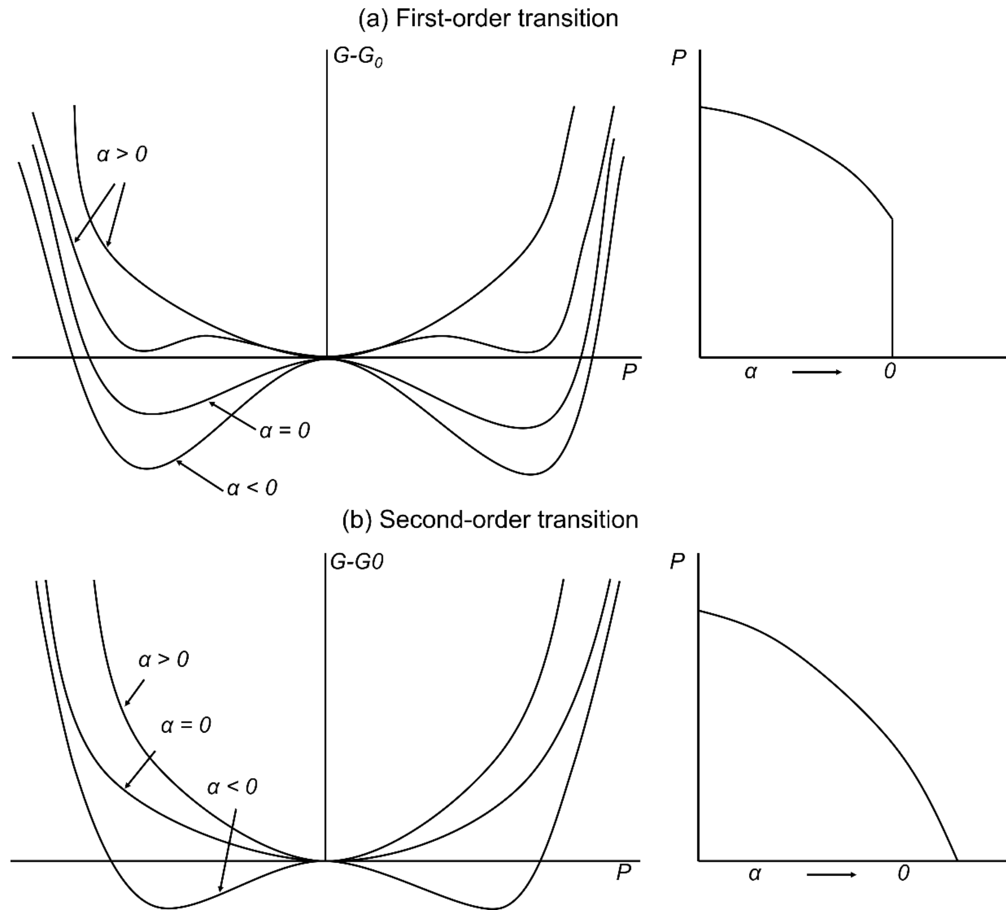

Figure 5: Representative behavior of the Gibbs free energy as a function of polarization and the polarization as a function of α for a given FE material with a (a) first- and (b) second-order phase transition. (Figure adapted from reference [30])

FE materials show a different type of a phase transition, which is called a "*diffuse phase transition*". Frequently the materials, which undergo such diffuse transitions, are denominated "*relaxors*" (RE) and these materials are the kernel of this work. The RE can be distinguished from canonical FE materials by the presence of a broad and diffuse dielectric peak on cooling over the so-called transition temperature T_m, at which the dielectric permittivity reaches a maximum value for a given frequency [6]. Worthy to notice that the Curie-Weiss relation is not obeyed close to T_m in RE ferroelectrics and, due to this fact, phase transitions in RE materials can not be described by the thermodynamic theory discussed here so far. The phase transition in RE ferroelectrics will be discussed further with more detail.

2.2.4. Ferroelectric Domains

FE materials are subdivided into regions with different spontaneous polarization directions when the materials cool down from high temperature above the transition point. These regions are denominated as ferroelectric domains (FE domains). This subdivision is due

to the minimization of the electrostatic energy of depolarizing fields and the elastic energy due to mechanical constraints. If all the dipoles of the polarization are directed towards in one direction, the electrostatic energy of the system is extremely large and the system becomes unstable [30, 88]. For a stable FE single crystal, a single FE domain state is the lowest free energy allowed. Nevertheless, different domain structures may form, depending on the electrical and mechanical boundary conditions. For instance, in the case of the $PbTiO_3$ ferroelectrics, six equivalent polarization states may occur, depending on the stress and electric field condition during cooling [89].

Domains with polarization parallel to c-axis are called *c*-domains, while other with perpendicular orientation are called *a*-domains, and the boundary between different domains is called *domain wall*. These domains are few unit cells thick and can be classified as 180º domain wall (if the angle between the spontaneous polarization orientations of adjacent domains is 180 degrees) and non-180º domain walls (if the angles are not 180 degrees). In the tetragonal structure, 180º and non-180º (90º) domain walls can be produced in the crystal, but their formation mechanisms are distinct in some aspects. Both domain walls can minimize the depolarization field by compensating the space charges on the surface in an unpoled material, but only non-180º domain walls can relieve the elastic energy in the material. The elastic energy associated with the creation of the spontaneous strain in the ferroelectric can be reduced by the creation of ferroelectric domains structures. The existence of external constraints (such as other grains or a substrate in the case of thin films) increases the amount of this elastic energy, promoting then the creation of non-180 domain walls [90].

It is important to notice that both 180º and non-180º domain wall motion will affect and increase the dielectric properties of the FE materials, whereas only non-180º domain wall motion will affect the piezoelectric response. This effect is explained by the fact that the lattice parameters of unit cells at both directions of the 180º domain wall are the same, not inducing piezoelectric strain. Nonetheless, due to the different lattice parameters along the non-180º domain wall, the piezoelectric strain is largely induced in the crystal [91]. However, it is known that 180º domain wall movement also can increase the piezoelectric contribution when the electric field applied is higher than the coercive field. This is because there will be more FE domains aligned with the electric field, sharing the same spontaneous polarization direction, resulting in an expansion along the electric field direction, whereas the remnant amount of domains in opposite direction will decrease and consequently will shrink [92].

It is established that FE domain structure, as well as domain nucleation and domain wall mobility, are the most important factor that characterizes the FE properties in FE materials. The

mechanical and electrical conditions of a FE material will rule the domain dynamics in the formation of the FE phase.

2.3. RELAXOR FERROELECTRICS

RE ferroelectric materials have been of great interest due to their particular physical properties, e.g., very large dielectric susceptibility. Therefore, RE ferroelectrics are used in several fields including optical applications, piezoelectric sensors, and actuators [93]. After the discovery by Smolenskii *et al.* in the 1950s [22, 94], the discussion about the nature of ferroelectric relaxor transitions has been initiated. Attention was given to the question of whether RE ferroelectrics are indeed phase transitions which can be described with critical exponents, or if they are more correctly described by noncritical approaches such as glass-like freezing of electric dipoles [95]. Due to their technical applications, the investigation of the nature of the RE phase transition has gained more interest since then. Applications ranging from piezoelectric sensors (e.g. ceramics of lead zirconate titanate (PZT) or lead lanthanum zirconate titanate (PLZT) [96]) to optical applications (in which the strontium barium niobate (SBN) was chosen [97]) were abundant.

RE ferroelectrics are a type of materials with a disordered structure exhibiting intriguing properties [98]. These materials are distinguished by their dispersive dielectric response around the temperature of maximum dielectric permittivity, T_m [99]. In addition, relaxors also show a decrease in hysteresis and remnant polarization as temperature increases over T_m, frequency dependent ferroelectric/dielectric properties, and optical isotropy in absence of an external electric field.

The relaxor behavior was first observed in perovskite structures, with disorder of non-isovalent ions [e.g. $Pb(Mg_{1/3}Nb_{2/3})O_3$ (PMN) [100] or $Pb(Sc_{1/2}Ta_{1/2})O_3$ (PST) [101], in which Mg^{2+}, Sc^{3+}, Ta^{5+} and Nb^{5+} ions are fully or partially disordered in the B-sublattice of the perovskite ABO_3 structure]. Also, compounds with nonstoichiometric solutions have also shown the relaxor behavior, such as $Pb_{1-x}La_x(Zr_{1-y}Ti_y)_{1-x/4}O_3$ (PLZT), in which the replacement of La^{3+} for Pb^{2+} ions lead to vacancies on the A-sites of the perovskite structure [102]. Structures other than perovskites were found to exhibit relaxor behavior as well, as compounds with tungsten-bronze-type structures exemplified by $Sr_{1-x}Ba_xNb_2O_6$ (SBN) [103].

In order to better understand the behavior of RE ferroelectrics, it is necessary to consider several models explaining the relaxor behavior. Among the main models, we will discuss the:

compositional fluctuation model, superparaelectric model, first-principle method, dipolar glass model, and random field theory.

The compositional fluctuation model suggests that RE ferroelectrics have a common characteristic of two or more cations occupying the equivalent crystallographic site in the lattice structure. This model gives a direct explanation of the broad diffuse phase transition by the basic ideas that have been related to the dynamics and formation of polar nanoregions (PNRs) [104, 105].

The superparaelectric model, in turn, is an extended model of one proposed in the Smolenskii's theory [105], in which the relaxor behavior to a thermally activated ensemble of superparaelectric clusters [106]. The superparaelectricity model theory views that polar clusters are metastable or kinetically disordered. This can explain the frequency dependence of the dielectric permittivity, dielectric aging, metastable switching from micro to macro domain states, and the nonlinear behavior of the thermoelastic and optical properties. The polar clusters are actually the same PNRs and the broad diffuse phase transition is attributed to the size distribution of the polar clusters.

The first-principle method applied to the relaxor phenomena is based on fundamental physics, with no essential input parameters other than the desired chemistry [107]. Most first-principle calculations for piezoelectrics are based on the density functional theory (DFT)*, and local density approximation (LDA) is frequently applied. The energy for any configurations of atoms is computed by solving a set of effective Schrödinger equations with an effective potential that includes many-body contributions quite similar to those of uniform electron gas at each point in space. Forces, phonon frequencies (through thermal matrix), effective charges, dielectric constants, elastic constants, piezoelectric constants, and polarization are all directly computable for the static lattice (zero absolute temperature) for ordered structures. For finite temperatures, it is necessary to use the primary first-principles results to parameterize an effective Hamiltonian or potential model, which can then be used to study the effects of temperature and simulate disordered materials like the RE ferroelectrics.

Viehland *et al.* [60] have also proposed a model suggesting cooperative interactions among polar clusters could produce a glass-like freezing behavior, commonly exhibited in magnetic spin glass systems. Burns and Dacol [108] have shown the existence of a local random polarization in the RE system when the temperature is up to hundreds of degrees above T_m. This

---

* *Density functional theory* (DFT) is a computational modelling method that uses quantum mechanical principles. Quite used in physics, chemistry and materials science, this method is essential to investigate the electronic structure of many-body systems (such as atoms, molecules, and the condensed phases).

local random polarization can be classified as a dipolar glass model, which is characterized by Burns temperature (T_B) and freezing temperature (T_f). At this temperature, which is below the T_m, the root mean square polarization is not zero, while the average polarization is zero. These models suggest that the polar regions interact with each other and they are polarized by the local random field, explaining the polar dynamics and their extreme slowing down at the diffuse phase transition [109].

The random field theory regards RE ferroelectrics as an intermediate state between dipole glassy-like systems and normal ferroelectrics. Unlike the dipolar glass model, in which elementary dipolar moments exist on the atomic scale, the RE state is featured by the presence of nanoscale polar clusters (the same type of PNRs) of variable sizes, considered to be spherical and interacting in a random way. The RE ferroelectrics, in this model, are considered as systems with random sites and orientations of electric dipoles and unavoidable lattice defects (e.g. lead and oxygen vacancies) as the sources of random electric field distribution in any disordered FE material, playing a crucial role in the phase diagram and specific properties of these materials [110].

2.3.1. Phase Transition in Relaxor Ferroelectrics

The ferroelectric nature of the materials arises mainly from the competition of the dipolar ordering and disorder due to the structural composition, leading to uncommon static and dynamical properties [24]. Strong relaxor materials can be categorized into two structural families: perovskites with a complex composition, and tungsten bronze structure [106]. Due to chemical disorder and lattice defects, there exist dipoles that can polarize the region around them forming nano and microdomains [24]. A distinct transition from high temperature with polar nanodomains to a ground state that exhibits merging and relaxation of these polar regions exist in the RE ferroelectrics. The nature of the transition and composition of the relaxor state are still under discussion in the scientific community.

Comparing with normal ferroelectrics, it is worthy to list three qualitatively distinct aspects in the temperature dependence of the dielectric susceptibility. Firstly, the real dielectric susceptibility $\chi'(T)$ in normal ferroelectrics follows a Curie-Weiss law (with Curie temperature T_c); however, in RE ferroelectric materials the peak of susceptibility does not diverge. This peak position occurs at T_m, marking the dynamic freezing temperature of a glass-like transition [24]. Secondly, there is a strong frequency dependence of the peak position of the electric permittivity [i.e., T_m of ε' is frequency dependent]; in normal ferroelectrics, the transition

temperature is very well defined and the relative permittivity as a function of temperature can be described by the Curie-Weiss law. Finally, the polarization in normal ferroelectric goes to zero at Curie temperature; in RE ferroelectrics, the polarization persists well above T_m [106]. The observation of zero polarization at T_c in normal ferroelectrics indicates that polar nanodomains vanish while in the relaxor the nanodomains extend well beyond the glassy transition temperature [24].

Other important aspect that is valid to emphasize in this section is the difference between the hysteresis loops (E-P hysteresis loops) of normal ferroelectrics and those of RE ferroelectrics. In normal ferroelectrics, the hysteresis loop suggests that at zero field, there is a large polarization remanence, while in relaxors this polarization is considerably smaller. This difference is because the PNRs are randomly distributed. If high enough external field is applied, it is possible to produce a large polarization, but once the field is removed, the polarization comes to small values due to the randomness of the PNRs. Another aspect that is important to note is that in normal ferroelectrics there is a macroscopic structural change at T_c, while in RE that does not occur across $T_{m.}$ [24]. One can not expect that the transitions in normal ferroelectrics should be the same as in the RE ferroelectric materials, apparently not following the Curie-Weiss law.

One of the most investigated RE ferroelectric materials is the lead magnesium niobate (PMN). Several experimental techniques were used to investigate the phase transitions in PMN, including pyroelectric measurements, magnetic resonance, dielectric spectroscopy, neutron scattering, etc. At a very high temperature, the thermal fluctuation are so strong that was not possible to observe any polar structure in PMN. Upon cooling down, dynamic polar nanostructures (called here as PNRs) start to form at a temperature T_B, conventionally called the Burns temperature. It was reported that the main characteristic of the Burns temperature is the off-centering of Pb ions from their special position, resulting in the dynamics of the polar regions [111]. The formation of these PNRs was evidenced by refractive index measurements as a function of temperature on cooling [24]. Evidence of PNRs well above T_m was also observed in dielectric susceptibility in PMN material. The deviation from Curie-Weiss law becomes much stronger as T decreases, because the PNRs increase both in polarization and size.

PNRs are considered to affect the behavior of the crystals dramatically, giving rise to specific physical properties. At high temperature, the RE ferroelectrics exist in a non-polar PE phase, similarly to the PE phase of normal ferroelectrics. Upon cooling, there is a transformation into the ergodic relaxor state (referred as ER state), in which is characterized by

the appearance of the PNRs with randomly orientation distribution of dipole moments [98]. This transformation occurs at T_B and it is associated with the formation of PNRs. However, investigation on PMN and 0.7PMN-0.3PT materials by Bobnar & Kutnjak [112] does not exhibit clearly the temperature at which there is a formation of PNRs, observing a manifestation of high dielectric constant at temperatures higher than the predicted temperature, i.e., higher than T_B. It is worthy to notice that though there is a significant change in the dielectric properties through the formation of PNRs, there is no change in crystal structure on macro- and mesoscale. However, temperatures below T_B are considered as a new phase different from the PE phase.

The PNRs are mobiles and their behavior are ergodic when they are close to T_B. Cooling down below T_B the PNRs dynamics slow down significantly. At a low enough specific temperature, so-called freezing temperature (T_f), the PNRs dynamics in canonical RE become frozen and the RE ferroelectrics experience a transition from ER state to non-ergodic state (called here as NR state). This non-ergodicity feature found in RE materials is also found in dipole glass phase (e.g. in spin glass materials). The NR state can be irreversibly transformed into a FE state by the application of a strong enough electric field [113]. Such a feature found in the RE materials is what actually distinguishes typical dipole glass materials. Upon heating, the FE phase transforms to the ER one at temperature T_c, which is close to T_f. In many other relaxors, the spontaneous phase transition (without application of an external field) from ER phase into a low-temperature FE phase still occurs at T_c and then the NR state does not exist [98].

Another characteristic temperature found in RE ferroelectrics is the so-called T^* [114], being considered remarkable feature in this class of materials. A sudden increase in the average correlation length (which is associated with the average PNRs sizes and identified as ξ) begins specifically at T^*. This temperature defines the onset of condensation and eventual freezing of the PNRs orientation on further temperature decreasing [114]. This freezing corresponds to a local phase transition which gives rise to the static polar nanoclusters [115].

The observation of T^* was evidenced by several measurements, including x-ray diffraction, acoustic emission, and Raman spectroscopy. The existence of such nanopolar entities was verified by using neutron and x-ray elastic diffuse scattering around the reciprocal lattice points [116, 117]. This effect is rather similar to those caused by ferroelectric critical fluctuations, but with the difference consisting essentially of the shape of the scattering intensity. The scattering is very strong and is related to very large deformations of the crystal lattice. These deformations result from the collective local lattice distortions as well as the

formation of the extended chemically ordered regions related to PNRs [117]. The shape of the wave vector dependence of the scattering intensity at large distances from reciprocal lattice points deviates from a lattice functions, meaning that PNRs are more compact than the usual ferroelectric critical fluctuation, possessing better-defined borders. According to experiments [118], the measurement of the correlation length ξ obtained by neutron elastic diffuse scattering in the PMN material has suggested that the size of the PNRs onset is very small [with $\xi \sim 1.5\,\mathrm{nm}$ and practically temperature independent at high temperatures].

The unit cell parameter in a perovskite structure is in general ~ 0.4 nm, which means that the PNR is composed of only a few unit cells. Below 300 K, ξ begins to increase on cooling, reaching ~ 7 nm at 10 K. The most significant growth of ξ occurs near the transition temperature T_c in PMN crystal. Similar observations were found in PZN crystals, but with PNRs size larger than PMN crystal, growing from ~7 nm at higher temperatures to ~18 nm at 300 K (near T_c) [119]. The local structures of both systems exhibit both polar and strain distortions. They are partially dynamic at high temperatures, gradually freeze with cooling, and coexist with the long-range polar phase (FE phase) at low temperature [120].

Through the analysis between ξ and the integrated intensity of scattering, it has suggested that the number of PNRs also increases on cooling. However, in contrast to the temperature evolution of ξ, the increase begins right from T_B and, at around T_f, a sharp decrease of this number has been observed. This is probably due to the merging of smaller PNRs into larger ones, increasing consequently the average correlation length of polarization ξ, i.e. increasing the polarization order. Below T_f, the number of PNRs remains practically the same at any temperature.

2.3.2. Models and Theories about origin and evolution of PNRs in relaxors

The cause and mechanisms of PNRs formation in relaxors are under discussion and they are not conclusively understood [98]. At temperatures higher than T_B, the structure and properties of RE ferroelectrics are quite similar to those of normal ferroelectrics. Experimental observations in relaxors suggest that the relaxor crystals tend to be Ferro- (FE) or Anti-ferroelectric (AFE) at low temperatures, but the quenched compositional disorder somehow prevents the occurrence of the normal transition into the phase with FE or AFE order in macro scale. Instead of this, occur the PNRs formation.

Among different approaches to explain the origin and evolution of PNRs, two of them will be presented herein: the compositional fluctuation model [121], and the random field theory [122]. The first model considers the PNRs as a result of the local phase transition or phase fluctuation, so that the crystal consists of islands of nanosized embedded into a cubic non-polar matrix that possesses symmetric structure (i.e. cubic structure). The second model assumes that the phase transition occurs in all regions of the crystal, possessing low-symmetry nanodomains separated by domain walls but without the regions of cubic symmetry [123]. Structural investigations have been done by Mathan *et al*. [124] and they showed that the two-phase model provides a good improvement in explaining experimental factors, leading to difficulty in distinguishing between the above models. This is mainly due to the local symmetry of the cubic matrix is not expected to be cubic and the thickness of domain walls is comparable with the size of nanodomains.

Concerning to the first model, the earliest version was developed by Isupov and Smolenskii [125, 105]. Due to the compositional disorder found in RE materials, the concentrations of different types of ions [e.g. Mg^{2+} and Nb^{5+} in PMN] are subject to quenched spatial fluctuations. Consequently, as T_c depends on the concentration, spatial fluctuations of local T_c are expected. The model suggests that local ferroelectric phase transitions occur first in those regions where Curie temperature is higher, while other regions of the crystal remain in the PE phase. Therefore, PNRs are simply regions with elevated Curie temperature.

The second model was proposed by Westphal, Kleemann, and Glinchuk (being known as the WKG model) and is represented by the random-field approach [126]. They applied the results of the earlier theoretical work to the RE ferroelectrics [127]. In this paper, it was demonstrated when the order parameter has a continuous symmetry, the ordered state is unstable against an arbitrary weak random field near T_c. Below T_c, the system undergoes a breakdown into small nanodomains instead of forming a long-range ordered state (which characterizes the FE state). In this model, the trivial case of the local spontaneous polarization, which is oriented in the same direction as the quenched electric field is not considered. Instead of this, the situation is determined by the interplay between the surface energy of domain walls and the bulk energy of domains in the presence of arbitrary weak random fields [127].

The quenched random electric fields may originate from the disordered distribution of the heterovalent ions, which is inherent to the compositional disordered structure [again, e.g. Nb^{5+} and Mg^{2+} in PMN]. It is important to mention that for displacive transitions, continuous symmetry means that the spontaneous deformation is incommensurate with the PE lattice. However, for perovskite ferroelectrics, in which the spontaneous deformation and the

polarization are aligned along defined crystallographic directions and depending on the number of allowed directions in a specific structure, the symmetry of the order parameter can be considered quasi-continuous. Therefore, this approach appears to be applicable.

The thermodynamic potential in the frame of Landau theory of phase transition (discussed in previous chapter) for the system with similar energies of the FE and AFE phases was investigated by Ishchuk [128]. The phenomenological description assumes that the state with coexisting FE and AFE domains might have lower thermodynamic potential than the homogeneous (FE or AFE) state. This effect is mainly due to interactions, such as electrostatic and elastic, between the FE and AFE domains. In summary, the nonpolar regions, coexisting with PNRs (FE domains), are actually domains of AFE structures.

Several other models use the microscopic approach and consider the structural evolution and formation of PNRs in terms of interatomic interactions. It is known that the balance between the electrostatic (dipole-dipole) interactions and the short-range repulsions determines the lattice distortion in ferroelectrics with ordinary perovskite structures. This balance is affected by the hybridization between the oxygen 2*p* states and electronic states of cations with covalent bonding, influencing, therefore, the phase transition temperature [129]. In the compositionally ordered crystals, i.e., possessing translational symmetry, exactly the same forces will affect all the atoms of a certain type because they have the same coordination neighborhood. Now, in the case of compositionally disorder the ions of different kinds may be found in the neighboring unit cells at the same crystallographic position. In this case, the interatomic interactions responsible for the appearance of FE- and AFE-order in the compositionally ordered state become random, resulting in a disturbance of the long-range polar order. The models emphasize the importance of different interactions: the interactions under random local electric fields only (including dipole-dipole interactions) [122]; and the dipole-dipole interactions together with random short-range repulsions [130] or random covalent bonding [131].

In the random field theory developed by Glinchuk and Farhi (GF model) for relaxors [122], the transition is regarded as an order-disorder one. In other words, at high temperature, the crystal is represented by a system of reorientable dipoles that are embedded in highly polarizable “host lattice”. The dipole-dipole interactions are indirect and random, occurring via lattice. However, according to the theory, they should lead to non-uniformly oriented local fields and then to FE ordering at low temperature, in contrast to direct dipole-dipole interactions, which can lead to a dipole glass state. Nevertheless, we know that in relaxors, there is an absence of macroscopic FE order and additional sources of random local electric fields have to be taken into account. These additional fields can be either static, i.e. coming from

quenched compositional disorder, lattice vacancies, impurities, and other imperfections, or dynamic, which in turn can be associated with shifts of non-ferroactive ions from their undisturbed positions [98]. These fields should be larger, in contrast to the fields considered in the WKG model, in order to destroy the long-range FE order.

FE order parameter, phase transition temperature T_c, and linear and nonlinear dielectric susceptibilities are calculated within the framework of statistical theory using the distribution function of local fields. It was shown that, depending on the parameters used in the model [e.g. concentration of dipoles, other field sources, and the host lattice correlation length], the low-temperature phase can be either FE, dipole glass, or a mixed state called Ferro-glass. In the temperature range between T_c and T_B, the short-range clusters may appear, in which the reorientable dipoles are ferroelectrically correlated (i.e. the PNRs). This might be related to the recently introduced T^* temperature. In the Ferro-glass (FG) state, these clusters coexist with the macroscopic regions in which the dipoles are coherently ordered.

2.3.3. Dielectric Response in Relaxors

A small-signal dielectric response has been investigated in a large number of RE materials, but most of the studies have been restricted to a very narrow frequency range of 10^1-10^9 Hz (or narrower). With an application of a larger frequency interval in relaxor investigations, it has been found that significant dielectric dispersion exists in the whole spectrum starting from the frequency of lattice vibration down to lowest practically measurable frequency of $f \sim 10^{-5}$ Hz.

The field-induced polarization in relaxors can be divided into several qualitatively different parts so that the total relative permittivity in the temperature range of maximum permittivity can be written as

$$\varepsilon = 1 + \chi_e + \chi_{ph} + \chi_R + \chi_U + \chi_{LF} \quad (21)$$

where $\chi_e, \chi_{ph}, \chi_R, \chi_U$ and χ_{LF} are the electric susceptibilities (complex numbers) describing the electronic, phonon, “conventional relaxor” (CR), “universal relaxor” (UR), and “low-frequency” contributions, respectively [30]. All the contributions are frequency dependent and they are ranked in the order of increasing typical characteristic time.

As many materials, the electronic contribution persists in relaxors all temperatures and high frequencies, i.e. 10^{15}-10^{17} Hz. At lower frequencies, the value of the electronic contribution

to dielectric susceptibility reaches a value of $\chi_e'(n^2-1)\sim 10$ is as small as compared with other susceptibilities.

The phonon susceptibility, also called lattice susceptibility that is caused by the mutual displacement of cation and anion sublattice, is active up to the frequencies of 10^{12}-10^{14} Hz. To determine the phonon contribution, χ_{ph}, infrared reflectivity spectra has been measured in relaxors at temperatures lower than the T_B. In PMN crystals, χ_{ph} increases from ~40 at 20 K to ~100 at 300 K [132]. In other words, it constitutes less than 1% of the total low-frequency permittivity measured neat T_m, only for lead-based relaxors.

The others susceptibilities, χ_R and χ_U related to the relaxation type polarizations, are the main contributions that give rise to the peculiar relaxor peaks in the temperature dependences of the dielectric permittivities*. The real part of χ_R is constant at low enough frequencies and decreases to zero when the frequency reaches the characteristic value, which is temperature dependent. The peak follows this decrease in the frequency dependence of the imaginary part. Both parts of the dielectric permittivity of the UR susceptibility decrease continuously in the whole frequency range available for measurements according to the power law

$$\chi_U' = \tan(n\pi/2)\chi_U'' \propto f^{\,n-1}, \tag{22}$$

in which n is close to unit but smaller. The values of χ_R and χ_U in relaxors are extraordinary large as compared to other dielectrics [98].

The CR dispersion is observed at the low-temperature slope of the permittivity peak, giving rise to the frequency shift of T_m, while the UR dispersion exists either at temperatures lower and higher than T_m. The UR dispersion was also observed in PMN with other compositions, at temperatures near and above T_m. The real part of the χ_U is only a small contribution to the total permittivity ε', but the imaginary part χ_U'' is the dominant contribution to the losses in a wide temperature range above T_m. In high-temperature phase, a divergent temperature behavior is observed, with $\chi_U'(T)\propto(T-T_0)^{-\gamma}$ and $\chi_U''(T)\propto(T-T_0)^{-\gamma}$ with $T_0 < T_m$ and $\gamma\cong 2$ [19]. The universal relaxor susceptibility is attributed to the polarization of PNRs, which are inherent to RE ferroelectrics.

* Cf. Figure 1(a) in ref. [20].

The last contribution χ_{LF} in Eq. (21) combines all possible relaxation contributions not related to the relaxor ferroelectricity, such as polarization of hopping of charge carriers, Maxwell-Wagner-type polarization, etc. In PMN crystals, the χ_{LF} contribution at lowest frequency leads to the significant increase of ε'' at temperatures above ~300 K.

In radio-frequency range, where the most dielectric properties of RE ferroelectrics are investigated, the value of χ'_R is much larger than χ'_U. The χ_U component was separated from the χ_R one by means of the analysis of dielectric spectra at $T > T_c$ (or at $T > T_f$) in several RE ferroelectric materials. Since the CR dispersion is the dominant contribution giving rise to the diffuse $\varepsilon'(T)$ peak, $\chi'_R \approx \varepsilon'$ in the vicinity of T_m, at least for the frequencies that are not very low or very high.

Different possibilities for the temperature evolution of structure and dielectric properties in compositionally disordered perovskites were presented by Bokov and Ye [98]. The temperature dependences of the relative permittivity at different frequencies have showed to exhibit the following types of temperature evolution: canonical relaxor; crystal with a diffuse RE-to-FE phase transition at $T_c < T_m$; crystal with a sharp RE-to-FE phase transition at $T_c < T_m$; and crystal with a sharp RE-to-FE phase transition at $T_c = T_m$*.

As shown recently for many RE ferroelectric materials, several relations have been attempted to described the dielectric permittivity $\varepsilon(T)$ of relaxors at $T > T_m$ [20]. One of these is the Lorentz-type empirical relation, given by

$$\frac{\varepsilon_A}{\varepsilon} = 1 + \frac{(T - T_A)^2}{2\delta_A^2}, \tag{23}$$

where T_A ($T_A \neq T_m$) and ε_A are the parameters defining the temperature of the dielectric peak and the extrapolated value of ε at $T = T_A$, respectively. The parameter δ_A is frequency independent at high enough frequencies and it reflects the diffuseness of the dielectric peak. Eq. (23) has described high temperature ($T > T_m$) dielectric permittivity quite well in a large number of RE ferroelectrics [133]. Also, there is an equation used to describe the dielectric

---

* The temperature intervals in which the regions of CR and UR dispersions, and the types of structure [e.g. PE, NR, ER, and FE phases] are easily identified in Figures 9.(a-d) in ref. [98]. It can be noticed a similar behavior of ε (T, f) at high temperatures in all cases [98].

permittivity, that is fitted by $\varepsilon_m / \varepsilon' - 1 \propto (T - T_m)^{\gamma}$ where $1 < \gamma < 2$, and ε_m is the value of ε' at T_m. The validity of Eq. (23) holds from T_1 (which is typically several degrees higher than T_m) to T_2 temperature (which is a few dozen of degrees lower than Burns temperature, T_B)*.

The CR contribution can consist of several components in itself involving different polarization mechanisms, with each of the mechanisms giving rise to the corresponding dispersion. To describe the CR spectra, the same empirical expressions used for other ferroelectric materials were applied, such as the Kohlrausch-Williams-Watts function (referred as KWW function) [134]. This function have been employed by different authors to fit the experimental data in order to explain the relaxation mechanisms involved in RE materials. The alternative way to analyze the dispersion is to find the appropriate function for the distribution of relaxation times (i.e. the frequency dependence). A remarkable feature observed first in PMN [60] and, therefore, in many other RE ferroelectrics is that the temperature dependence can be related to the frequency dependence of the ε' peak using the Vogel-Fulcher (VF) law, which can be described by

$$f = (2\pi\tau_0)^{-1} \exp[-E_a / k_B (T_m - T_{VF})], \tag{24}$$

where f is the measurement frequency, τ_0, E_a and T_{VF} are the fitting parameters, and k_B is the Boltzmann constant. The VF law was known in structural and spin glass and, when revealed in relaxors, it became one of the main reason to postulate the existence of a dipole glass phase at $T < T_{VF}$. Eq. (24) may signify the similar VF relation for the characteristic relaxation time τ of the corresponding relaxation process, given by

$$\tau = \tau_{\infty} \exp[E_a / k_B (T - T_f)], \tag{25}$$

in which τ_{∞}, E_a are the parameters and T_f is the freezing temperature (i.e. the temperature below which the relaxation becomes infinite).

This divergence of τ indicates that the thermally activated reorientations of dipoles is responsible for polarization slow down with decreasing temperature and become impossible

* T_1 and T_2 are other characteristic temperatures in the phase transition of RE materials.

(i.e. with dipoles does not respond to the electric field) at $T = T_f$, but not at $T = 0$ as Arrhenius law predicts for the dynamics of independent dipoles [135].

In dipole glasses, the interactions among the dipoles are the cause for such freezing. These interactions are frustrated (i.e. can be either FE or AFE, but cannot be satisfied simultaneously) and thus favor the configurations with random directions of dipoles, in contrast to the ferroelectrics and antiferroelectrics in which the dipole directions are parallel and antiparallel, respectively [98].

We have discussed the main relaxation mechanisms to explain the relaxor behavior found in RE ferroelectric materials. Several empirical expression have been proposed in order to describe the temperature and frequency dependence of dielectric permittivity of relaxors, e.g. Völger-Fulcher law, that is commonly used to analyze its dispersion and to find an appropriate function for the distribution of relaxation times.

3. EXPERIMENTAL TECHNIQUES AND MATERIALS PROCESSING

This chapter is dedicated to the details of the experimental procedure including the short description of PLZT and SBN thin films sintering processing as well as techniques and methods employed to characterize the samples. Besides, after describing the experimental setup, the operating principle of Piezoresponse Force Microscopy (PFM) will be explained addressing the experimental procedures used for domain imaging and a quantitative analysis. After, the Switching Spectroscopy Piezoresponse Force Microscopy (SS-PFM) will be described as well as qualitative and quantitative analysis that are possible to extract from this technique.

3.1. SAMPLE PREPARATION

3.1.1. PLZT Thin Films

$Pb_{1-x}La_x(Zr_yTi_{1-y})_{1-x/4}O_3$ (PLZT x / y / 1-y) thin films (x = 9%, y = 65%) were prepared in the Department of Physics and Chemistry of the Engineering Faculty of Ilha Solteira, in Sao Paulo State University, Brazil.

These thin films were sintered using a chemical route based on the Pechini Method (PM) [136]. Briefly, the idea is to prepare a polymeric resin, to deposit it onto a substrate and then crystallize the desired phase structure (perovskite) using a proper thermal treatment. The Pechini Method, also known as Polymeric Precursor Method (PPM), is used for the preparation of titanates and niobates by a polymeric resin are obtained through polycarboxylic acid and polyalcohol. The process is described by forming a chelate[*] between mixed cations (dissolved as salt in a water solution) and citric acid. In this method, various salts can be used, such as chlorides, carbonates, hydroxides and nitrates. Nitrates are preferred for strontium-doped and lanthanum titanates compounds [137].

The modification of Pechini Method used here is based on the fact that not all used precursor oxides (PbO, La_2O_3, ZrO_2 and TiO_2) are soluble in acid media, but only the reacted PLZT oxide is soluble. The PLZT powder with 10 mol% of Pb in excess was prepared by the conventional solid-state reaction using commercial reagents PbO (Synth, 98%), La_2O_3 (Aldrich, 99%), TiO_2 (Aldrich, 99%) and ZrO_2 (Aldrich, 99%). The mixed oxides were calcined in two steps: at 850 ºC for 3.5 hours and then at 1100 ºC for 3.5 hours. High-quality PLZT powder (with no second phase observed) is obtained from this solid-state method at room temperature

[*] A salt or a complex ion in which the binders coordinate themselves with either ion or central atom through two or more covalent bonds.

and was ready to be used as a starting precursor to prepare the polymeric resin by Pechini Method.

To prepare the stoichiometric polymeric resin, 100 mg of PLZT powder was dissolved in 50 ml of nitric acid solution, which comprises 10% of HNO_3 (nitric acid) and 90% of H_2O, at 80 ºC for 1 hour. Distilled water (~30 ml) has been added after the complete dissolution and a clean and transparent stock solution was obtained at room temperature. Then, citric acid (CA) was added to the stock solution (CA/metal molar ratio equal to 15) to form metallic ions citrate, heating and stirring the mixture at 90 ºC for 50 minutes. When the mixture reached about 5 ml in volume, ethylene glycol (EG) was added to the solution, with a CA/EG mass ratio equal to 6/4, keeping such mixture at 90 ºC during 20 minutes in order to complete the polymerization of the stoichiometric resin.

To compensate for the Pb-loss[*] during the thin film processing and to stabilize the growth of the perovskite phase, a second resin was prepared dissolving 0.0126 g of PbO in 10 ml of nitric acid solution at 80 ºC for 10 minutes [138]. The amount of PbO in the second resin represented 20 mol% in excess to the nominal composition of PLZT in the first resin. The second polymeric resin was prepared following the same process used in the first one. Lastly, both resins were mixed at room temperature and stirred for 1 hour for complete homogenization. After the homogenization, the obtained resin with volume about 15 ml was seen clearly transparent and ready to start the film depositions[†].

Thin films were obtained from polymeric resins deposited onto Pt/Ti/SiO_2/Si(100) substrates by spin coating technique. This technique is a procedure used to apply uniform thin films to flat surfaces. A typical process involves depositing a small amount of a fluid resin onto the center of a substrate and then spinning the substrate at high speed [139]. The centrifugal force will induce the resin to spread to the edge of the substrate leaving a thin film of resin on the surface [140]. The final rotational speed used to prepare PLZT thin films was 6000 rpm during 20 seconds. The pyrolysis was performed in air by putting the deposited films directly on a hot plate at approximately 200 ºC during 5 minutes following its placement in the electric furnace at about 300 ºC for 1 hour. The film thickness was increased by depositing new layers on previous pyrolyzed films and repeating all the procedure again to remove the organics. Final

[*] Due to the PbO volatilization, samples of PLZT thin films showed a formation of an undesired non-ferroelectric phase (i.e., the pyrochlore phase) that deteriorate the most important properties of Pb-based ferroelectric thin films. To see more about the formation of the pyrochlore phase in Pb-based film, see the reference [270].

[†] This procedure is necessary, since introducing the PbO excess directly in the PLZT powder leads to unstable polymeric resins that precipitates within some days after the preparation.

thickness and other properties depend on the nature of the resin (such as viscosity, surface tension, etc.) as well as on the parameters chosen for the spin process [140].

After reaching the required film thickness, the crystallization was promoted by means of a final heat treatment in an electric furnace at 700 ºC during 1 hour. The final thickness of the PLZT thin films obtained was uniform and crack-free with the series thicknesses of 240, 350, 430, and 540 nm. These film thicknesses were observed through a Scanning Electron Microscopy (SEM) on transverse sections of the thin films.

3.1.2. SBN Thin Films

In this work, SBN thin film with nominal composition $Sr_xBa_{1-x}Nb_2O_6$ (SBN x) (x = 75%) has been prepared by the same polymeric chemical route based on Pechini method, already described above. Barium carbonate BaCO3 (Aldrich), strontium carbonate SrCO3 (Aldrich), and niobium ammonium oxalate $NH_4H_2NbO(C_2O_4).3H_2O$ (CBMM, Brazil) were used as starting reagents.

Let us now describe the SBN thin films processing. Initially, niobium ammonium oxalate was dissolved in aqueous solution of citric acid at 40 ºC for 10 minutes to form niobium citrate. After homogenization, ethylene glycol (EG) was added to promote polymerization of mixed citrate by polyesterification reaction at 90 ºC for 30 minutes. Cooling down this solution at room temperature, a transparent resin is obtained. Next, dissolving together the strontium and the barium carbonates at the same condition in a separate solution of citric acid, a citrate solution is also formed. Adding ethylene glycol to the citrate mixture solution, the polyesterification reaction occurs at the same temperature to obtain another transparent resin.

In both cases, the CA/metal molar ratio was fixed at 5, while the CA/EG ratio was about 4/6 (in mol%). After that the resins were mixed at room temperature and stirred for 1 hour for homogenization. After adjusting the viscosity with distilled water, a clear polymeric resin was finally obtained.

SBN thin films of polymeric resins were obtained by deposition onto $Pt/Ti/SiO_2/Si(100)$ substrates. The rotation parameters used in the spin coating technique were 6000 rpm and 20 seconds for speed and duration of rotation, respectively. Pyrolysis was carried out in air initially, deposited on a substrate placed on a hot plate at 200 ° C for 10 minutes and then taken to the electric furnace at 400 ° C for 30 minutes in order to remove organic components. Again, the film thickness increases as more layers are added to the previously pyrolyzed film, promoting the removal of organics with the same heat treatment mentioned

above. After reaching the desired thickness, the film was led to the electric furnace to perform the promotion of crystallization at 700 ° C for 1 hour. The final SBN thin film obtained was uniform and free of cracks, having a thickness of about 550 nm.

3.2. CHARACTERIZATIONS

3.2.1. X-ray Diffraction Analysis

X-ray diffraction (XRD) is a quite useful technique for studying of crystalline materials and it is essential for advanced research in materials science. This technique has been used to investigate the structural properties of materials, such as determine and identify the crystalline phases and the unit cell parameters by refinement using the Rietveld method [141]. The refinement evaluates the diffractogram systematically using a pattern of a known structure as a starting point based on the method of least squares. Furthermore, it is possible to obtain structural information about the XRD patterns, like crystallite size, stacking faults, microstrain, and other defects in the crystalline structure by using the Williamson-Hall analysis [142].

In the Rietveld method, the refinement comes to the end when the calculated diffraction pattern is as close as to the observed one. In this condition, as in any process, which uses the method of least squares, the square value of the difference is minimal. In order to calculate the quality of refinement, some statistical parameters are evaluated, such as R_{Bragg} and χ^2. The R_{Bragg} parameter is given by $100\sum|I_{obs}-I_{calc}|/\sum|I_{obs}|$ and measures the quality of a refined structural model, in which $I_{obs,h}$ and $I_{calc,h}$ are the observed and calculated intensities related to the nth point. The good-of-fit (GOF) χ^2 is given by ($R_{wp}/R_{\exp}$) wherein $R_{\exp}$ refers to the statistical analysis of data intended to predict the final value of refinement and R_{wp} is a parameter that indicates how good the refinement was done. The closer the statistic parameter to the unity are the statistical parameters, the higher the quality of the refinement.

In this work, this technique has been used to investigate the structural properties at room temperature of PLZT and SBN thin films using a Rigaku Ultima IV diffractometer with CuK_{α} (1.5406 Å) radiation. For the Rietveld analysis, the software used for the refinement of the crystal structure of samples was the *General Structure Analysis System* (GSAS) using the graph interface EXPUGUI.

Based on the refined data, Williamson-Hall (WH) analysis was applied in order to investigate the structural properties of polycrystalline PLZT and SBN thin films. The crystallite size and lattice strain (microstrain) are two important properties that are obtained by analyzing

the peak width of the diffraction patterns. Due to the formation of polycrystalline clusters, the crystallite size of the particle is not the same as the particle size [142].

The origin of the strain is due to different factors such as grain boundary, partial dislocations, and contact or sintering stress [143]. In many ways, the peaks observed in the diffraction patterns are influenced by the crystallite size and the microstrain, which increase the peak width and intensity shifting the 2θ peak position respectively. WH analysis is a method in which the enlargement induced by the effect of the size and strain are treated by considering the peak width as a function of 2θ.

The diffraction profile can be expressed in the Gaussian form in terms of the lattice *d*-spacing that is detection-mode independent, given by $I(d) \propto \exp\{-[(d-d_{hkl})/s]^2\}$, in which $I(d)$ indicates the diffraction peak intensity as the function of *d* planar spacing and *s* is a statistical scale parameter to define the diffraction peak width. Usually, the diffraction peak width is correlated to the often-used Full Width at Half Maximum (FWHM) defined by $FWHM = 2s(\ln 2)^{1/2}$. For a Gaussian distribution, it is denoted as σ, and the relation becomes $FWHM = 2(\ln 2)^{1/2}\sigma$. Here, we denote the observed FWHM as $\Delta d_{obs} = \left(d^2 - \bar{d}^2\right)^{1/2}$, reflecting the *d*-lattice span around the mean $\bar{d}$ of a particular *hkl* diffraction peak.

The peak profiles observed in the diffraction patterns are results of convoluted functions of multiple effects, such as the instrument response, the grain size and the microstrain (lattice deformation). The microstrain is resulted from the stress heterogeneity and the dislocation density at any condition [144]. We can write down all the contributions to the peak width profile resulted from deconvoluted through Fourier Transform, given by

$$\Delta d_{obs}^2 = \Delta d_{ins}^2 + \Delta d_{size}^2 + \Delta d_{\varepsilon}^2 . \tag{26}$$

Accordingly to Equation (26), Δd_{ε}^2 and Δd_{size}^2 are the microstrain and size contribution to the observed peak width, respectively, and Δd_{ins}^2 is the peak width for the stress-free state, usually referred to the instrumental contribution*. From Bragg's law, we have that $\lambda = 2d\sin\theta$, in which λ is the wavelength of x-ray, *d* is the *d*-spacing of planar and θ is the diffraction angle. Let us consider that θ_B is the angle of maximum intensity of diffraction, and θ_1 and θ_2 are the angles where the intensity is zero. Obviously, for $\theta_1 > \theta > \theta_2$ the intensity is non-zero.

* Non-Gaussian components typically exist due to intricate contributions to a peak profile, which could introduce errors in the peak width determination.

Supposing that the crystallite of thickness *D* has (*m* + 1) planes in the diffraction direction, $2D\sin\theta_1 = (m+1)\lambda$ and $2D\sin\theta_2 = (m-1)\lambda$ are the destructive interferences related to the diffraction pattern in that direction. Subtracting one from the another, we have $D(\sin\theta_1 - \sin\theta_2) = \lambda$ i.e. $2D\{\cos[(\theta_1 + \theta_2)/2]\sin[(\theta_1 - \theta_2)/2]\} = \lambda$. Making θ_1 and θ_2 so close to θ_B, we have that $\theta_1 + \theta_2 \approx 2\theta_B$ and, consequently, $\sin[(\theta_1 - \theta_2)/2] \approx (\theta_1 - \theta_2)/2$, resulting in $2D[\cos\theta_B(\theta_1 - \theta_2)/2] = \lambda$. Defining $\theta_1 - \theta_2 \approx \Delta d_{size}^2$, finally we have crystallite size contribution to the peak profile ,

$$\Delta d_{size}^2 = \frac{k\lambda}{D\cos(\theta_B)} \tag{27}$$ [*]

The second main source of specimen broadening is the strain, or more correctly, the inhomogeneous strain. Let us consider one crystallite undergoing diffraction with the parameter *d*, λ, and θ given by Bragg's law. If the crystallite is strained then the *d* spacings will be changed. A compressive stress would make *d* spacings smaller and a tensile stress would make the *d* spacing larger. In other words, the spacing would be given by $d \pm \delta d$. According to Bragg's law, the position of the peak will increase from 2θ to $2(\theta + \delta\theta)$. It is expected no enlargement effect of the diffraction peak due to homogeneous stress in crystallites. If the crystallite is stressed (compressed) by the same amount (homogeneous stress) would result only in a shift of the peak intensity of diffraction. However, if the strain is inhomogeneous then different crystallites will be strained by different amounts and the shifts in 2θ will be variable. By differentiation of Bragg's diffraction equation with respect to *d* and 2θ, respectively, we have that $4\Delta d\sin\theta_B = d\cos\theta\Delta(2\theta_B)$. Rearranging, we get

$$\Delta d_\varepsilon^2 = 4\left(\frac{\Delta d}{d}\right)\tan\theta_B = 4\varepsilon\tan\theta_B \tag{28}$$

in which we defined $\varepsilon = \Delta d/d$ is the inhomogeneous strain and Δd_ε^2 is the strain contribution to the broadening of peak profile. Taking the Equation (28) and carried out the necessary replacements, we finally

---

[*] Equation (27) is the *Sherrer formula* that describes grain size in diffraction. The constant *k* added to the formula is a correction factor for the actual contribution of crystallite size.

$$\Gamma = 4\varepsilon \tan\theta_B + \frac{k\lambda}{D\cos\theta_B} \qquad (29)^{*}$$

in which $\Gamma = \{\Delta d_{obs}^2 - \Delta d_{ins}^2\}$ is the *FWHM*.

In order to calculate the structural properties using the WH method, we need to plot $\Gamma\cos\theta_B$ as a function of $4\sin\theta_B$ and then to fit it by compare the standard equation for a straight line ($y = mx + c$). The slope will be the microstrain ($\Delta d/d$) and the linear coefficient is inversely proportional to the crystallite size (*D*), where *d* is the lattice spacing, λ is the wavelength, and θ_B is the Bragg angle.

3.2.2. Scanning Electron Microscopy

Scanning Electron Microscopy (SEM) is a type of electron microscope that images the sample surface by scanning it with a high-energy beam of electrons in a raster scan pattern. There are many possible interactions between the high-energy electron beam and the atoms in the specimen. SEM can provide information about topography, crystalline information, chemical composition and electrical behavior of samples [145].

In SEM, a source of electrons is focused into a fine probe that is rastered over the surface of the specimen (Figure 6). A number of interactions can occur as the electrons penetrate the surface sample, resulting in the emission of electrons or photons from the surface. Appropriate detectors can collect a fraction of the electrons emitted, and the output can be used to modulate the brightness of a cathode ray tube (CRT).

The SEM principal images can be produced using three types of contrast: secondary electron images, backscattered electron images, and elemental x-ray maps. The secondary and backscattered electrons are identified according to their respective energies and they are produced by different mechanisms. The secondary electrons result from the inelastic scattering of electrons from the beam of atomic electrons, and when the energy of the emitted electron is less than 50 eV, by convention it is referred as a secondary electron. Higher energy electrons are primary electrons that have been scattered without loss of kinetic energy, i.e. interacted elastically by the nucleus of an atom.

---

[*] This equation is so-often related to Williamson-Hall method. Other methods also are available for separating the effects of size and strain. This is the case of *Warren-Averbach* method, that is quite complex and involves expressing the peak intensity in terms of a Fourier sum.

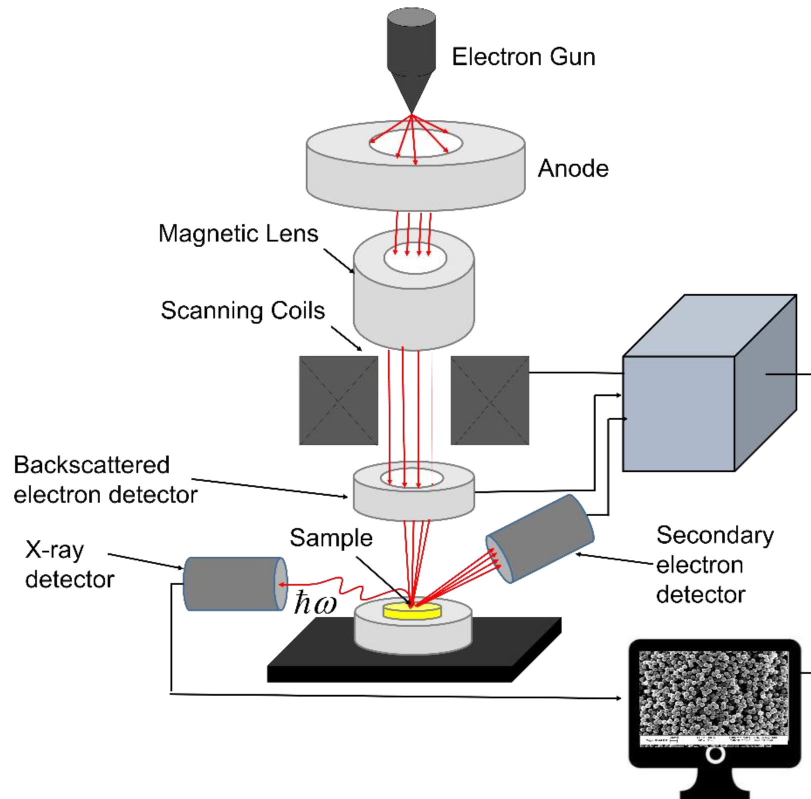

Figure 6: Schematics of the operation principle of SEM

Another interaction in SEM technique occurs when the electrons from the beam collide with the surface and eject an internal electron from an atom. The excited atom will decay to its ground state through emission of a characteristic x-ray photon. This photon signal can be distributed by energy in the energy dispersive x-ray detector. This is the basis of the Energy Dispersive X-ray Spectrometry (EDS). This technique is used for the elemental analysis of chemical characterization of a sample and it will be used to infer about chemical components in the thin films. Both of SEM techniques were used in this work to obtain the morphologic properties and elemental analysis in our films.

3.2.3. Dielectric Characterization

For most applications, dielectric properties are important to provide information about the polarization mechanisms. Dielectric permittivity ε and dielectric loss (tan δ), are the most important parameters used to investigate the dielectric properties of FE materials. To perform the electric characterizations, a set of circular gold electrodes (0.3 mm in diameter) were deposited using a RF-sputtering on the film surface (1×1 cm^2) homogeneously. Generally, the dielectric permittivity is obtained from the measurements of the capacitance under an AC

electric field with frequency dependence, within the interval range of several Hz to hundred MHz. The relative permittivity ε_r can be obtained by the simple relation

$$\varepsilon_r = \varepsilon' = \frac{Ct}{\varepsilon_0 A}, \quad (30)$$

where C is the measured capacitance, ε_0 is the dielectric permittivity of vacuum, A is the area of the electrodes, and t is the sample thickness. Additionally, dielectric losses are obtained from the ratio of the imaginary part ε'' to the real part ε' of the dielectric permittivity, where ε'' is given by $\varepsilon'' = \frac{\sigma}{\omega \varepsilon_0}$, which σ is the conductivity, ε_0 is the static dielectric permittivity, and ω is the external electric field angular frequency.

The electrical measurements comprise the dielectric and ferroelectric properties of thin films. The dielectric characterizations were performed in the setup metal/dielectric/metal using the LCR Agilent 4184A, with measurements for dielectric permittivity $\varepsilon = \varepsilon' + i\varepsilon''$. Investigation of the dielectric permittivity as a function of temperature was done in the thin films studied here, seeking for information about the phase transition. The temperature control used in this work was an ARS cryostat, DE202A1-800K model, with a Lakeshore 340 control adapter, using a precision of 0.1 K in a temperature interval range of 80-450 K. The dielectric permittivity also can be represented in the complex form $\varepsilon = \varepsilon' + i\varepsilon''$ and taking into consideration the RC circuit, we obtain $\varepsilon' = (Bt/A\omega\varepsilon_0)$ and $\varepsilon'' = (Gt/A\omega\varepsilon_0)$, where B and G are the susceptance and the conductance, respectively.

The AC-voltage dependence of the real and the imaginary components of the dielectric permittivity was investigated in a frequency range interval from 100 Hz to 1MHz. In order to verify the influence of the probing electric field (AC probe) on the dielectric properties, the dielectric permittivity was measured with several AC voltages from 0.2 V to 18 V.

3.2.4. Ferroelectric Hysteresis Measurements

For the acquisition of the ferroelectric hysteresis measurements, we used two types of experimental configuration. One for obtaining the polarization-electric field hysteresis (so-called the P-E hysteresis) using the Ferroelectric Module of Aixacct TF 2000 system (aixAcct Systems GmbH, Germany) which utilizes the virtual ground feedback method. Operated in the Dynamic Hysteresis Measurements Mode (DHM), a voltage sweep is applied to the sample in capacitor geometry and the current response is obtained. Voltage pulses consisting of bipolar

triangular forms were applied to our samples and the current was obtained using a virtual ground trans-impedance amplifier [146]. Another configuration used in this work was performed using modified Sawyer-Tower (ST) circuit. The ST circuit is composed by a digital oscilloscope (Agilent 54622A) coupled to the function generator (Agilent 33220A) and to a high-voltage amplifier Trek 610E. These measurements provide information about the polarization of saturation, remnant polarization, and the coercive voltages of the studied samples.

3.2.5. Piezoresponse Force Microscopy (PFM)

Recent advances in synthesis and fabrication of micro and nanoscale ferroelectric brought to life new physical phenomena and devices that need to be better understood at this scale. As structure dimensions are getting smaller, ferroelectrics display a pronounced size effect that manifests itself in a significant deviation of the properties of low-dimension structures from their bulk analogs. Following the miniaturization challenge, novel techniques are required for the evaluation of ferroelectric and piezoelectric properties with the high and ultimately nanoscale resolution. To address the fundamental mechanisms underpinning the functional of FE materials and devices, domain structures and their evolution under bias have to be studied at the micro and nanometer scales. The rapid evolution of scanning probe microscopy (SPM) and PFM has resulted in a significant advancement in this area.

Güthner and Dransfeld [147] were the first who demonstrated the use of the PFM in 1992 investigating a FE polymer film. In such demonstration, they locally poled domains with the help of the tip and subsequently imaged the generated domain pattern. Since then, PFM has become a standard tool for imaging FE domain patterns as can be verified in literature the significant PFM-related publish articles [28, 148, 149, 150, 47]. PFM is a versatile, easy-to-handle, non-invasive method for imaging FE domain patterns or any kind of FE material without the need of an elaborate sample preparation. In addition, it detects the domain-specific piezoelectric deformations of a sample when an electric field is applied to it with help of a conductive tip.

The PFM experimental basis consists in the use of a standard scanning force microscopy (SFM) operated in contact mode with an additional oscillating voltage applied to the conductive tip. The voltage-induced deformations of the sample lead to periodic vibrations of the sample surface, which are transmitted to the tip. The resulting oscillations of the cantilever are sensitively read out with the help of a lock-in amplifier (LIA).

PFM is generally applied to the investigation of FE domain patterns and, since ferroelectricity entails piezoelectricity, the domain pattern can be visualized by its piezo mechanical deformation under the application of an electric field. In the case of PFM, the electric field is applied locally with the help of a tip. The name of the piezo mechanical response of a FE domain obtained by the PFM is called of PFM signal. The difference between PFM signals obtained from different domains on a multi-domain sample is denoted by the PFM contrast.

The PFM approach for probing piezo and ferroelectric properties at the nanoscale is based on the strong coupling between polarization and mechanical displacement. Common atomic force microscopy (AFM) provides an ideal platform for local piezo effect study due to high vertical resolution and high localization of electric field at the junction between the metalized tip and the surface. Then, the PFM is a contact-mode AFM in which an electrically biased conductive AFM tip is used as a probe of local electromechanical coupling via the converse piezoelectric effect.

The experimental setup for PFM technique used in this work can be found with more details elsewhere [28]. The alternative voltage V_{ac} (amplitude V and frequency *f*) is applied to the tip using a function generator and the resulting oscillations of the cantilever are read out with a LIA. This voltage also can be applied to the back electrode (BE) while grounding the tip [28]. In PFM, a voltage is applied to the conductive tip as

$$V_{tip} = V_{dc} + V_{ac}\cos(\omega t). \tag{31}$$

Here, V_{dc} is the DC bias, often called as switching bias, V_{ac} is the AC bias, called probing bias, and ω is the AC bias angular frequency. As the sample contracts or expands due to the converse piezoelectric effect, the tip deflection is monitored using a LIA so that the oscillation is given by

$$A = A_0 + A_{1\omega}\cos(\omega t + \varphi), \tag{32}$$

where A_0 is the static surface displacement and φ is the phase shift between the driving voltage V_{ac} and the voltage induced deformation $A_{1\omega}$. The voltage-induced deformation is composed of the true piezoresponse term due to local piezoelectric deformation described by the effective

piezoelectric coefficient and the local electrostatic deformation. The oscillation due to the voltage induced is given by

$$A_{1\omega} = (d_{33})_{eff} V_{ac} + \frac{\partial C}{\partial z}(V_{dc} - V_S)V_{ac}, \quad (33)$$

which $(d_{33})_{eff}$ is the piezoelectric coefficient resulted from the converse piezoelectric effect, V_S is the surface potential, and C is the capacitance of the cantilever-sample system.

While the PFM amplitude provides information on the magnitude of the local electromechanically coupling, PFM phase images give the local polarization orientation. The resolution of the images obtained by the PFM is less than ~10-30 nm as determined from half of the width of a domain wall in the mixed PFM signal. The most used for characterization is given by $PR = A_{1\omega} \cos(\varphi)$, with φ is either close to 0º or to 180º.

The contrast mechanism and detection of ferroelectric domain patterns with PFM are based on the fact ferroelectric materials are necessarily piezoelectric [81]. Basically, the cantilever performs three kind of displacements: (i) vertical deflection as a result of the out-of-plane force due to $(d_{33})_{eff}$ coefficient, (ii) torsion, that is caused by the shear piezoelectric coefficient $(d_{15})_{eff}$, and (iii) buckling from the interaction with the surface when an in-plane force acts along the cantilever axis. The first type of deformations is described as out-of-plane, or as vertical PFM (VPFM) measurements.

If the polarization and the applied electric field are parallel, the deformation positively results in an expansion and the piezoresponse signal is in phase with the V_{ac}. Otherwise, if the electric field and the polarization are antiparallel, this will cause the piezoelectric to contract with the consequent lowering of the cantilever and the electric field and the piezoresponse signal are out-of-phase by 180º.

A dual frequency technique, coined Dual AC Resonance Tracking (DART), was applied in order to map the mechanical properties of the conservative and dissipative nature of the tip-sample interactions [151]. The topography and the piezoresponse measurements were performed with a scanning probe microscope MFP-3D (Asylum Research, Oxford Instruments, USA). The probes (Nanosensor, USA) with a platinum conductive coating, with a tip radius <20 nm, resonance frequency 50-90 kHz, and spring constant 2-5.5 N/m were used. Piezoresponse measurements also were carried out in a DART-PFM mode with 4 V AC for the SBN thin films.

Additionally to the PFM imaging of FE domain structures and local polarization control, local spectroscopy measurements have been developed in order to investigate the polarization switching phenomena on the nanoscale [152]. The Switching Spectroscopy Piezoresponse Force Microscopy (SS-PFM) has been developed to address quantitatively the local switching characteristics of FE materials. Similarly, SS-PFM also is implemented on a commercial AFM equipped with additional function generators and LIA.

The tip approaches the surface vertically in contact mode until the deflection setpoint is achieved. The hysteresis data are then acquired with the tip fixed in a local using the waveform illustrated in Figure 7a. The data are analyzed in real time to yield parameters describing the local switching process such as the positive and negative coercive biases, imprint voltage, saturation response, and work of switching, as we can observe in Figure 7b.

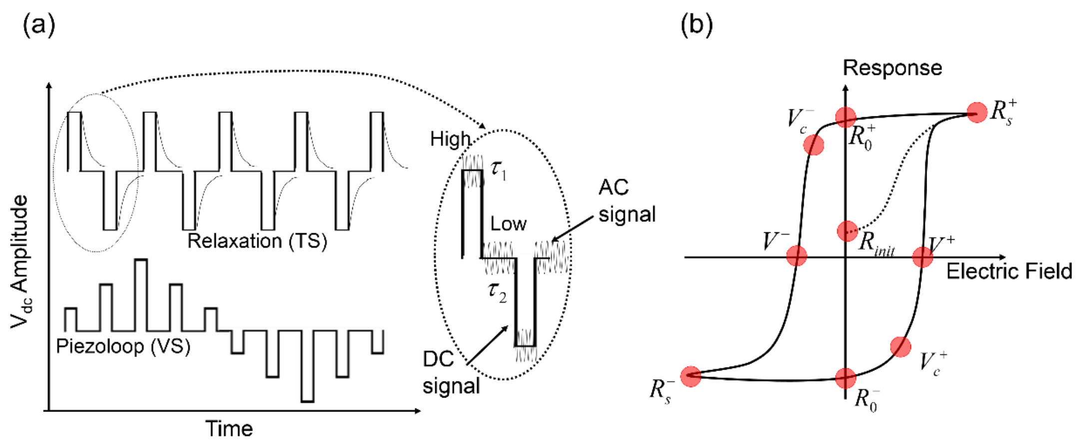

Figure 7: In SS-PFM, local hysteresis loop and piezoresponse relaxation can be locally collected. In (a) we can observe the single-point probing waveform in SS-PFM and the data acquisition sequence for both local piezoloops and piezoresponse relaxation. In (b) is represented a schematic behavior of a PFM hysteresis loop obtained in a FE material.

Hysteresis in PFM is rather different when compared to hysteresis obtained in a macroscopic sample. Macroscopic hysteresis occurs due to the nucleation growth and interaction of multiple separated domains. Otherwise, in PFM hysteresis the nucleation of a single domain occurs under a sharp tip and PFM signals follow the development of domains at a single location [152]. The piezoloops are obtained by an application of variable magnitudes of DC voltages and, at the same time, by applying a small AC voltage to acquire the piezoresponse after the local poling (See Figure 7b). This kind of PFM measurement is called voltage spectroscopy.

Another type of analysis using PFM is denominated as time spectroscopy. The tip is placed in a certain location and the induced piezoresponse is measured as a function of time after applying different DC voltage pulses and different pulse durations. It was found that the

induced piezoresponse of the FE domain was unstable and relaxed with time after switching off the DC bias. The relaxation of induced FE domains is acquired by measurement of the piezoelectric deformation after the removal of the DC bias. The relaxation of the field-induced $(d_{33})_{eff}$ has shown to be dependent on both magnitude and duration of the DC voltage [153].

Time dependences of the PFM signal measured after poling voltage can be described by several fitting curves, such as Curie-von Schweidler (CvS) law, $f(t) = (t/\tau_{CvS})^n$; simple exponential $f(t) = \exp(-t/\tau)$; Kolruausch-William-Watts (KWW) given by $f(t) = -\exp\left[-(t/\tau_{KWW})^\beta\right]$; or logarithmic $f(t) = B_0 + B_1 \ln t$. The KWW dependence is usually used to describe a thermally activated relaxation [154].

In summary, the local piezoelectric response of FE materials can be investigated as a function of applied DC voltage and pulse duration using the PFM. With an application of DC voltage pulses of sufficiently large magnitude can result in the appearance of FE-like order and, consequently, hysteresis. The relaxation of the induced polarization can be studied as well, providing valuable information about domain pinning, fatigue, aging, and imprint effect.

4. RESULTS AND DISCUSSION

This chapter is dedicated to the discussion of the experimental results of SBN and PLZT thin films. Our main goal is to discuss the results at macro and nanoscale and understand the mechanisms involved in the relaxor ferroelectric properties using piezoresponse force microscopic (PFM). Structural and dielectric properties will be relevant for the understanding of the spontaneous polarization phenomena as well the switching properties and relaxation of ferroelectric domains of relaxor thin films.

4.1. NANOPOLAR DOMAIN STRUCTURE OF RELAXOR $Sr_{0.75}Ba_{0.25}Nb_2O_6$ (SBN) THIN FILMS

To understand the properties of the SBN films at the nanoscale, we first studied its major dielectric and ferroelectric properties of the sample. The microstructure of SBN thin film was also investigated by SEM. A local chemical composition (via *energy dispersive scattering* – EDS) was carried out to quantitative and qualitative tests of the thin film using SEM technique. The analysis of SBN at nanoscale was performed through PFM technique to imaging both topography and domain structure as well as measuring the switching and relaxation properties of induced ferroelectric domains in SBN thin films.

4.1.1. Macroscopic and Physical Properties of SBN Thin Films

The observed, calculated, and difference profiles obtained by Rietveld refinements of the x-ray diffraction data for polycrystalline randomly oriented SBN thin film is shown in Figure 8. The indexed (*hkl*) peaks refer to the tetragonal phase of SBN with *P*4*bm* space group. The diffraction peaks referring to the platinum substrate are indicated as Pt (111) and Pt (200) belonging to the cubic phase with $Fm\bar{3}m$ space group and lattice parameter a = 3.892 Å. No peaks typical of other phases are evidenced.

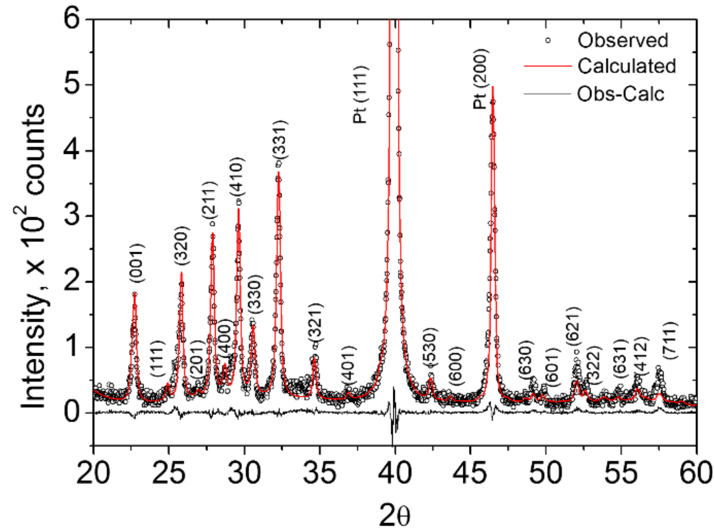

Figure 8: Refined structure with observed (dots), calculated (red lines), and difference (bottom lines) XRD profiles of $Sr_{0.75}Ba_{0.25}Nb_2O_6$ thin film.

Table 1 shows the summary of the atom coordinates and their occupancy of the SBN structure obtained by Rietveld method. The crystallographic R-factors obtained from the refinement, such as R_{wp} and R_p, were 14 and 9.1 respectively, and the goodness-of-fit (χ^2) was 1.7. This indicates a good agreement between the observed and calculated patterns as a good fit was obtained. Thus, it was concluded that the structural parameters and calculated lattice parameters (Table 1) obtained by refinement are representative for the SBN film investigated in this study and indicates that the SBN thin film is polycrystalline on Pt(111)/Si/SiO_2 substrate. The refined lattice parameters (a = 12.4243 Å and c = 3.9082 Å) are very similar to those obtained in SBN single crystal with the same nominal composition (Sr = 75%) [38, 42].

Table 1: Summary of Rietveld refinement for $Sr_{0.75}Ba_{0.25}Nb_2O_6$ film obtained at room temperature*.

Atom	X	Y	Z	Occupancy
Nb1	0.0000	0.5000	0.0236	1.000
Nb2	0.0747	0.2115	0.0089	1.000
Sr1	0.0000	0.0000	0.5000	0.822
Sr2	0.1724	0.6724	0.5069	0.503
Ba1	0.1724	0.6724	0.5069	0.343
O1	0.3450	0.0049	0.0546	1.000
O2	0.1369	0.0679	0.0663	1.000
O3	0.2800	0.7800	0.0356	1.000
O4	-0.0155	0.4845	0.5093	0.500
O5	0.3092	0.4024	0.4795	0.500
O6	0.2792	0.4364	0.5023	0.500

Lattice parameters: a = 12.4243 Å; c = 3.9082 Å
GOF and R-factors: χ^2 = 1.7; R_{wp} = 14; R_p = 9.1

* The SBN crystal structure can be visualized in Fig.3 in Ref [284]

4.1.2. Microstructure Analysis of SBN thin films

The microstructure of the SBN thin films was investigated using a SEM. It was used to carry out qualitative and quantitative analysis of the local chemical composition of SBN thin films via Energy Dispersive Scanning (EDS). Figure 9a and Figure 9b depict top view SEM micrographs of the edge and surface of the thin film. The morphology of SBN thin film showed to be rather spongy, exhibiting a high degree of porosity and homogeneous spatial distribution with pores of different sizes (~20-100 nm).

The porosity is generally formed in thin films regardless the film preparation technique (such as electrodeposition, sol-gel, or sputtering) [155]. In most cases, pores are considered undesirable because they can expose substrates to corrosive agents, reduce mechanical properties, and detrimentally influence density, electrical and optical properties [156, 157], and diffusion characteristics of particles [158]. Index of refraction was shown to depend only on the porosity and on the pore size, shape and spatial distribution for a certain critical film thickness [159]. However, nano and mesoporous morphology have been introduced purposely with different sizes, shapes, and spatial distribution in order to tailor their physical properties [160].

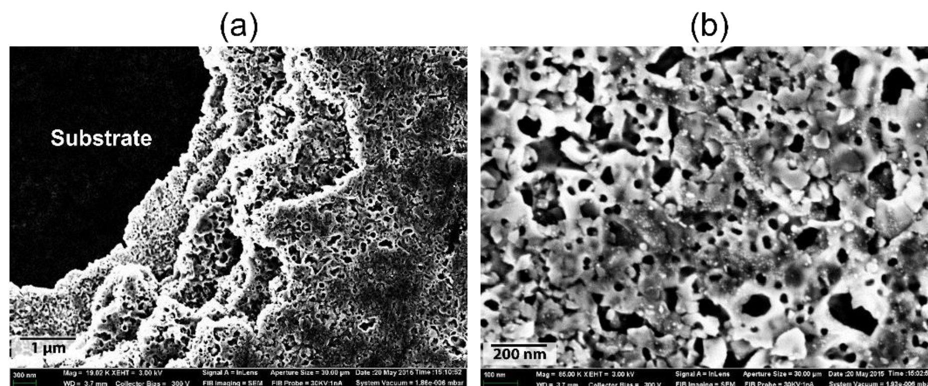

Figure 9: (a) Scanning electron microscopy (SEM) of the SBN thin film obtained at the edge using electron bean of 3 kV with approximately 20,000x of magnification and the top view SEM images obtained with (b) 85,000x magnification.

A specific surface area was chosen to present the morphology of the boundary between the SBN film and the Pt substrate. We can clearly observe that in specific regions, the film was removed layer by layer, presenting a ladder-type profile (Figure 9a). This is an evidence of deterioration of the mechanical properties of the SBN thin film probably due to the presence of pores, causing a decrease in adhesion between the layers. Figure 9b-d present a top view SEM images with different magnifications. Moreover, the weak adhesion may come from the low interdiffusion of the layers at the low temperature (300 ºC) used for the thermal annealing aiming to remove the organic contents. After this first thermal annealing, and before the next

one at high temperature (700 ºC), crystallization of the last-deposited layer probably already started, explaining why the adhesion on the previous deposited layer is not very strong.

In Figure 9b, it is possible to observe some irregularities in the topography due to the deleterious effect of the porosity in SBN thin film. In Figure 9c and Figure 9d porous microstructure with a certain degree of order and periodicity is shown. The pore size distribution is rather inhomogeneous, ranging from 20 to 100 nm. Regarding the morphology, some pores present round shape while are more irregulars, displaying, in general, an interconnected porosity.

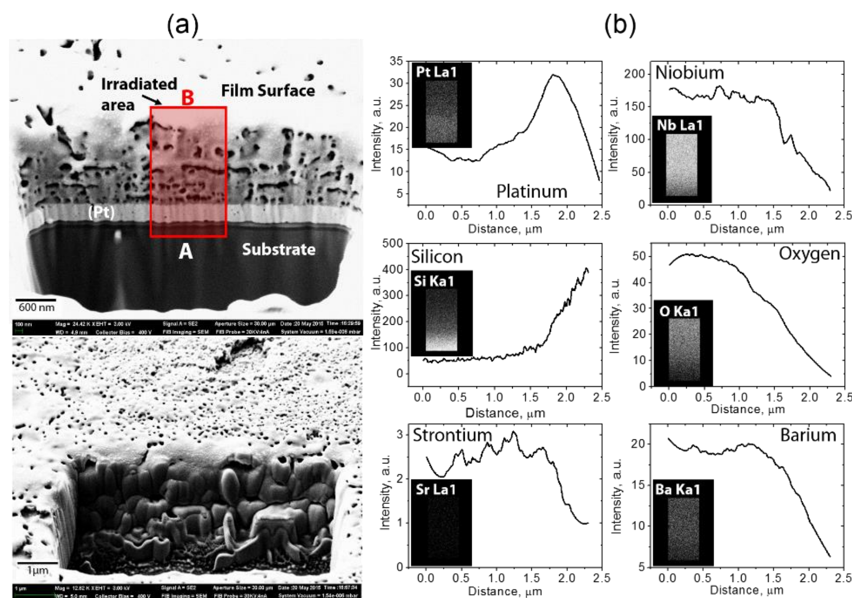

Figure 10: (a) Cross-sectional SEM image of the SBN thin film and (b) the representation of the distribution of the secondary electrons respective to the specific chemical element with the chemical composition in the cross section obtained inside the rectangle drawn in (a).

The cross-sectional SEM image of the SBN thin film and the quantitative analysis of its chemical composition are shown in Figure 10. The images were obtained using a focused ion beam (FIB) of argon atoms to mill the film. The voltage and current of the FIB probe were 30 kV and 4 nA, respectively, with a system vacuum of ~ $1.59 \cdot 10^{-6}$ mbar. Figure 10a shows clearly the morphology details in the cross section, such as the Pt/Ti/SiO_2/Si(100) interfaces, the thickness and surface of the SBN thin film. Moreover, it is also possible to observe a high degree of porosity, the interconnected porosity through the film thickness and the presence of pores in the metallic substrate as well, being considered one of the possible causes of porosity in thin films [161].

Pores can also emerge by misfit of crystal grains due to structural defects in the film-substrate interface [162] that could explain the presence of interconnected porosity on the early stages of the nucleation and growth of the SBN thin films during the coalescence of the

crystallites [163]. It is possible that the pore formation in SBN thin films is mainly due to the burning out of organic in pyrolysis treatment.

The qualitative analysis of chemical components by SEM showed in Figure 10c have presented a significant amount of silicon near Pt/Si substrate and a small quantity of Pt, while elements such as niobium, strontium, barium, and oxygen increase as the cross-section analysis of the SEM approaches film surface.

4.1.3. Electrical Properties of SBN Thin Films

The temperature dependence of the real and imaginary dielectric permittivity, $\varepsilon'(T)$ and $\varepsilon''(T)$ respectively, is shown in Figure 11 in the frequency range of 10-600 kHz. The maximum observed for ε' decreases and the temperature of maximum dielectric permittivity (T_m) are shifted to higher values with increasing frequency. The broad frequency and temperature dispersions of ε' indicate that SBN thin film undergoes a relaxor-type dielectric transition.

The maximum temperature T_m = 221 K at 10 kHz observed in Figure 11 is lower by 100 K as compared to reported SBN single crystals (T_m ~ 320 K, at 10 kHz) with the same nominal composition (Sr = 75%) [45, 164, 37]. Similar results were obtained for SBN thin films prepared by pulsed laser deposition (PLD) which the shift of the phase transition temperature to lower temperatures than in single crystals was attributed to larger defect densities in the film [165]. It is well known in single crystals that the effect of lowering the phase transition temperature is also a consequence of disorder in Sr and Ba sites, long thermal annealing being necessary to rearrange these ions [37]. This effect of lowering the phase transition temperature was observed also in ceramics when compared with the single crystal of SBN with the same nominal composition [166, 167]. The high density of defects, such as oxygen vacancies, a larger concentration of grain boundaries, and in addition the interface to the substrate in our case, may be the reasons for such effect. This behavior was also observed in another relaxor ferroelectric thin films with perovskite structure [168].

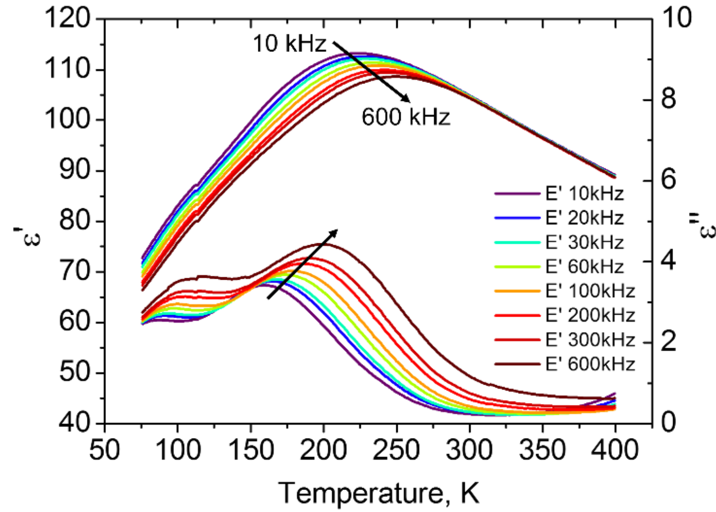

Figure 11: Real and imaginary dielectric permittivity of SBN thin film as a function of temperature at measurement frequencies of 10, 20, 30, 60, 100, 200, 300, and 600 kHz.

The imaginary part of the dielectric permittivity in Figure 11 presents two evidenced peaks as a function of temperature at different ac frequencies. The peak centred around 200 K for 600 kHz is probably related to the relaxor transition from a paraelectric phase to a relaxor phase. The another peak centred near 100 K for 600 kHz maybe is related to the structural change from monoclinic to tetragonal in SBN thin films but it is not clear the mechanisms behind this behavior.

The diffuseness of the phase transition can also be described by an empirical parameter ΔT_{dif}, defined as $\Delta T_{dif} = T_{0.9\varepsilon_m(100Hz)} - T_{\varepsilon_m(100Hz)}$, i.e., the difference between $T_{0.9\varepsilon_m(100Hz)}$ (temperature corresponding to 90% of ε_m at 100 Hz at higher temperature) and $T_{\varepsilon_m(100Hz)}$ that is the temperature of maximum permittivity at 100 Hz. The ΔT_{dif} was found to be 95.5 K in our SBN thin film, relatively higher than in single crystals reported by Li, J. *et al* [169] ($\Delta T_{dif} = 51\,\mathrm{K}$ and $\Delta T_{dif} = 11\,\mathrm{K}$ for SBN single crystals prepared by conventional and microwave techniques, respectively). Moreover, the degree of relaxation behavior, that is described as $\Delta T_{relax} = T_{\varepsilon_m(100\mathrm{KHz})} - T_{\varepsilon_m(100\mathrm{Hz})}$ for the SBN thin film was about 34.8 K, while in the single crystal at same frequency interval it did not exceed 10 K.

The broadened dielectric peaks illustrate a relaxor-like behavior in which the maximum relative permittivity decreases and T_m shifts to higher temperatures with increasing frequency, indicating a diffuse phase transition (DPT) [98]. The DPT can be described by the modified Curie-Weiss law [36]

$$\frac{1}{\varepsilon'} - \frac{1}{\varepsilon'_m} = \frac{(T - T_m)^\gamma}{C} \tag{34}$$

in which ε' is the dielectric permittivity, T is the temperature, ε'_m is the maximum value of ε at $T = T_\mathrm{m}$, C is the modified Curie constant, and γ is a measurement of diffusivity. For $\gamma = 1$, the ferroelectric material behaves as a normal ferroelectric, for $\gamma = 2$ the material shows a complete disordered system, and an intermediate value $(1 < \gamma < 2)$ the material exhibits diffuse ferroelectric characteristics [170]. The γ-factor obtained for the SBN thin film by fitting was approximately 1.62, confirming a typical diffuse ferroelectric behavior [24]. The γ-factor obtained to our film was slightly higher than the values of diffusivity factor for ceramic samples and single crystals compared to the same composition ($\gamma \sim 1.51$ for SBN75 single crystals) [164].

Comparing the results of ΔT_{dif} , ΔT_{relax} and γ, the diffuseness of the phase transition and the frequency dispersion in SBN thin films are higher than in single crystals of the same composition. This effect may be due to a higher structural disorder and compositional fluctuations in thin films [106, 34]. The origin of the relaxor behavior observed in SBN thin films is also believed to be due to random electric fields (RFs), which probably promotes the formation of PNRs. RFs are considered to be related to induced-charge disorder due to vacancy distribution on A-sites of the TTB structure, developing the relaxor state in SBN thin films [171].

It is natural to conclude that the larger diffuseness of the phase transition and the lowering of phase transition temperature when compared to single crystals and ceramics with the same composition are mainly due to higher ionic and nanoscale field disorders in SBN thin films. As structural disorder increases in TTB structure, different repulsive forces of among nearby cations will impose different potential barriers to the hopping process to come about. Under specific thermal conditions, a potential barrier can come or not be overcome by ions in the structure [30].

The frequency dispersion near the dielectric maxima in RE ferroelectric materials can be attributed to the distribution of relaxation times. Among a large number of theoretical models that have been proposed to understand the diffuseness of maximal dielectric permittivity with temperature and frequency, the Vogel-Fulcher model is one of the most important mathematical representation of the discrepant nature of the relaxation times [172] with a temperature interval

[98]. The observed angular frequency dependence of T_m could be described by the Vogel-Fulcher equation [169, 173, 174], given by

$$\omega = \omega_0 \exp[-E_a/k_B(T_m - T_f)] \tag{35}$$

in which ω_0 is the pre-exponential term, E_a is the activation energy from polarization fluctuation of an isolated micropolar region, T_m is the temperature of the maximal relative permittivity, k_B is the Boltzmann constant, and T_f is the Vogel-Fulcher temperature (i.e., the static freezing temperature that is frequency-independent). The fitting parameters (T_f, ω_0, and E_a) in Vogel-Fulcher model are presented as converted parameters in Figure 12.

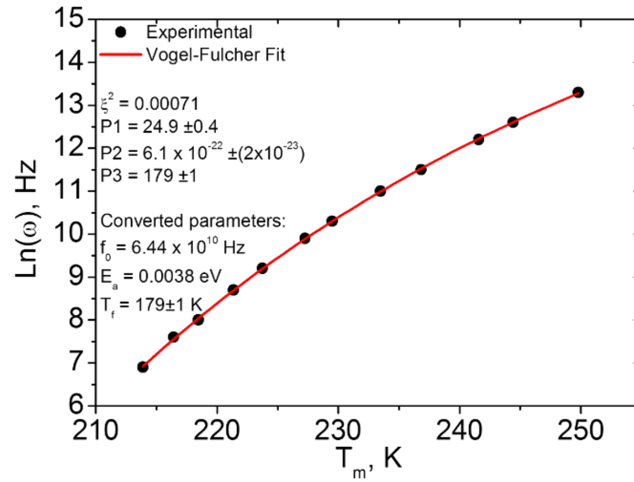

Figure 12: Temperature dependence of the frequency of the maximum permittivity in SBN thin film.

Fitting the experimental data by Equation (35), the SBN thin film showed a typical spin-glass-like dielectric relaxation behavior, which is attributed to the randomly oriented dipolar and electric fields [24]. The fitting parameters obtained were $\omega_0 = 1.0 \times 10^{10}$ Hz, $T_0 = 179$ K, and $E_a = 0.0038$ eV. Independently of the analyzed frequency-dependence, the maxima of the dielectric permittivity and dielectric loss as a function of temperature do not coincide the freezing temperature T_f, which is the temperature where the system experiences a transition from ergodic to non-ergodic phase [175]. These results were compared in literature for SBN single crystals and ceramics. For single crystals with same composition, the results were $\omega_0 = 2.3 \times 10^{11}$ Hz, $T_f = 311$ K, and $E_a = 0.0133$ eV [164]. For SBN ceramics with $x = 70\%$ of strontium, the fitting parameters of Vogel-Fulcher relationship with $\omega_0 = 3.4 \times 10^{11}$ Hz, $T_f = 326$ K, and $E_a = 0.011$ eV have been reported [169]. The apparent change in these parameters is a natural consequence of lowering phase transition temperature in SBN thin films.

As opposed to ordinary FE materials, in which the effect of the electric field felt by an ion in the lattice is treated in terms of average field (mean field theory) [176, 87], in SBN thin film the ions do not experience an average field, but rather local RFs induced by defects. The RFs distribution occurs just because the A-sites are randomly and partially occupied (See Table 1) by strontium and barium ions in the structure as well as the existence of intrinsic disorders, such as valence and size difference in the occupying cations. Therefore, spatial fluctuation of RFs promotes correlations between the fluctuations dipoles, leading to the assemblage of clusters on a mesoscopic scale, oppositely to the conventional FE material that the formation of the macroscopic domain is prevailed [126].

As Vogel-Fulcher temperature T_f of the SBN thin film is much smaller than the SBN single crystals, the transition from ergodic state to the non-ergodic state occurs at much lower temperatures [172]. The barrier potential height for the fluctuation of dipoles, also called activation energy (E_a) of the hopping process, is correlated to anisotropic energy and volume of the cluster, indicating that PNRs are smaller and RFs distribution is more complex in SBN thin films as compared to single crystals and ceramics [98]. Moreover, we can infer that in the SBN thin films the degree of disorder is larger than in single crystal and ceramics of the same composition, resulting in the flattening of the dispersive curve (larger ΔT_{dif} and ΔT_{relax}) and the shifting of the phase transition temperature [37, 38, 164].

In order to investigate the effect of space charge and hopping polarization, we plotted in Figure 13a the frequency dependence of real and imaginary part of dielectric permittivity (*i.e.* ε' and ε'') obtained at $T = 300$ K in the frequency range of 0.1 kHz -1000 kHz. As follows, we observe a smooth decrease of ε' in the frequency range and a sharp in decrease of ε'' in the low-frequency region, showing a frequency independent value of these parameters in the high-frequency interval. This strong decrease of ε'' towards high-frequency range may be due to space charge polarization and interface effect or due to the dc conductivity inversely proportional frequency on SBN thin film.

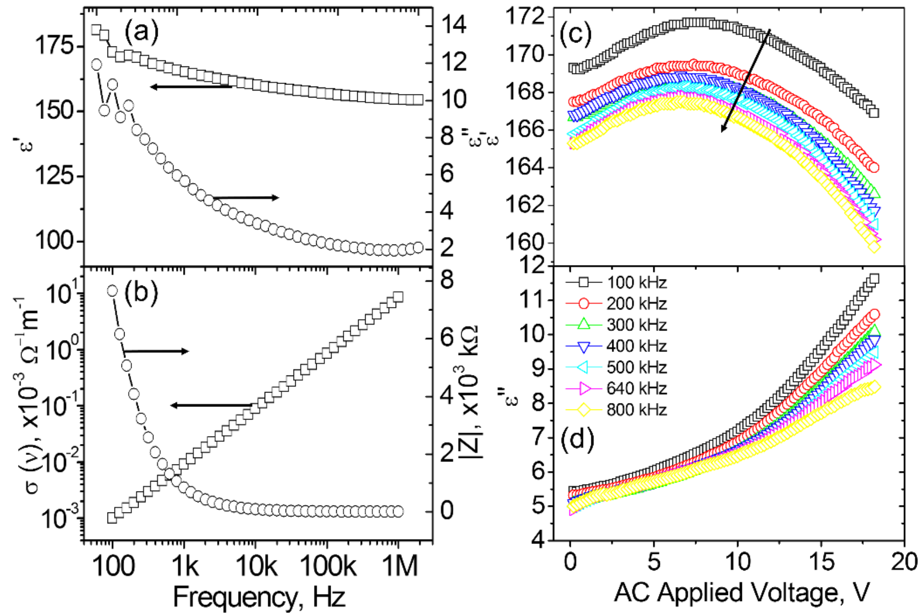

Figure 13: (a) Real and imaginary part of the dielectric permittivity as a function of the frequency in the SBN thin film, and (b) the modulus of the impedance and the conductivity, respectively. The behavior of (c) dielectric permittivity and (c) dielectric loss as a function of AC amplitude for different frequencies.

The frequency dependence of the AC conductivity and impedance are shown in Figure 13b. At room temperature (T ~ 300 K) the conductivity increases with increasing frequency, which is a characteristic of ω^n, and n is a positive exponential. The phenomenon of conductivity in solids is often analyzed by Jonscher's power law and it is described by the function $\sigma(\omega) = \sigma_{dc} + A\omega^n$, which σ_{dc} is the DC contribution, A is a constant and n is an exponent in the range of $0 \le n \le 1$. The n constant represents the degree of interaction between mobile ions with the lattice around them, and A determine the strength of polarizability.

The estimated value of n is very close to unit at 300 K for the SBN thin film. The origin of the frequency dependence of conductivity is due to the movement of charge carriers in the bulk of the sample [177]. As the slope of log[σ(ω)] as a function of log[ω] is constant, the relaxation phenomena observed in Figure 13b indicates that it is only due to space charge polarization. To observe the change of the polarization process in the conductivity curve with the frequency we should notice a change in the slope, indicating a transition to another type of polarization. SBN thin film at lower temperatures, where the frequency effect on hopping process is more relevant, may evidence the existence of the hopping process.

In order to investigate the observed dielectric dispersion of the SBN thin film, we also carried out the complex impedance analysis. The modulus of the impedance is shown in Figure 13b. The both real and imaginary parts of the impedance, described by Z' and Z'' showed to decrease with frequency increasing. However, Z'' is relatively higher than Z' depending on the

frequency interval[*]. The value of Z' and Z'' at 300 K appear to decrease up to 1 kHz, and be frequency independent at higher frequency. Since we have no measurements below 100 Hz, it is not possible to infer about the behavior of the impedance below this region. Ceramics of $BaBi_4Ti_4O_{15}$ have presented a peak of Z'' as a function of frequency around 200 Hz at 660 K, maybe due to the relative high Curie temperature (with T_c ~ 700 K) [178]. The decreasing of Z'' with frequency may be associated to the presence of mobile charges and defects at high temperature. As these observations are made at relative high temperature when compared with temperature of maximum dielectric permittivity, defects may be responsible for electrical conduction in the material via hoping of electrons/oxygen ion vacancies/defects among the available localized sites [178].

The behavior of ε' and ε'' as a function of ac electric field are presented in Figure 13c and Figure 13d, respectively, for different frequencies of the AC applied voltage. As we can observe, the real part of the dielectric permittivity (Figure 13c) experiences an increase in the range of 0.2-7.5 V of amplitude of AC driving field. For higher values of AC amplitude ($V_{ac} \geq$ 7.5 V), we notice a decrease of ε' for all frequencies. In addition, the maximum values of ε' ($\varepsilon'_{\max}$) are centered on 7.5 V at different driven frequencies, indicating the behavior of AC probe amplitude of $\varepsilon'_{\max}$ is frequency independent.

The growth of ε' under different ac amplitude driven fields indicates that this extrinsic contribution has an important role in the ferroelectric domain formation. In the case of FE materials, such behavior is a direct consequence of domain formation and movement of domain walls [179]. There are barrier potentials in such domains that must be overcome in order to take place the movement of the domain walls, promoting a coalescence of domains oriented toward the external field. In other words, the increasing of AC driven field will allow more dipoles to reorient towards the AC electric field direction, so that the dielectric permittivity is consequently increased for all driving frequencies.

However, we can observe a decrease of the intensity of $\varepsilon'_{\max}$ as we increase the AC frequency probe. Such behavior in RE ferroelectrics is due to the presence of nanodomains with a different distribution of relaxation times. Since the distribution of relaxation times in relaxors varies with temperature, different time-dependence of the polarization at various temperature results. At $T \ll T_f$, since there is a large proportion of frozen dipoles in the system, the average polarization remains relatively high with small fluctuations. For rising temperatures, the

[*] An analysis of Z''/Z' as a function of $\log_{10}(\omega)$ has exhibited a linear dependence in the 100-500 kHz of frequency interval.

relaxation time distribution moves to higher frequencies and, as a result, the value of the average polarization decreases with greater fluctuations. In our case, at $T \gg T_f$, the flipping of dipoles is faster compared to the temperature at $T \ll T_f$. However, as the frequency of the measuring electrical field increases, more polar microregions become slow due to not being able to keep up with the switching of the measuring field [172].

As we described above, different polar microregions have distinct characteristic times, depending on the local RFs. External factors, such as temperature, ac amplitude signal, and dc poling field, influence the macroscopic measurement of dielectric properties. The potential barrier that the dipoles need to surpass is decreased with both increasing temperature and ac driving field, promoting more flipping of dipoles towards the external field. However, it is observed that for ac amplitudes greater than 7.5 V, the value of the permittivity decreases for all frequencies measured. This effect may be due to the accretion of space charges, forming a depolarizing field that decreases the values of permittivities or just surpassing coercive voltage of SBN thin film in all driven frequencies.

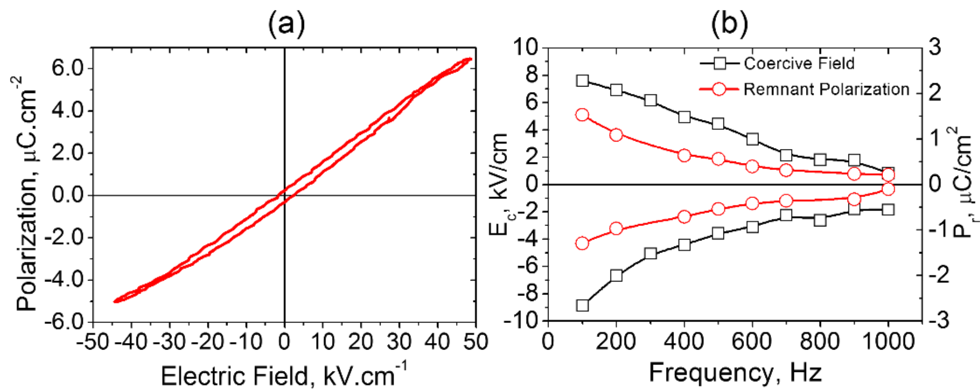

Figure 14: (a) *P-E* hysteresis loops of the SBN thin film measured at room temperature and (b) the behavior of the positive and negative coercive electric field and remnant polarization as a function of frequency.

Observation of hysteresis loop is one of the essential criteria for the existence of FE properties in a material. Macroscopic FE properties of SBN thin films were verified by the FE hysteresis measured with Sawyer-Tower method. Figure 14a shows the hysteresis loops of the SBN thin film at room temperature at 900 Hz using a triangle waveform with an AC driving voltage of 200 mV. It was observed that the hysteresis loop shapes change with the increasing frequency, with the loop slim and characteristic for RE ferroelectrics. For lower frequencies, the shape of the hysteresis loop shows a saturation, indicating a contribution of electric conductivity in the current signal. This conduction may be due to the arisen of charge carriers through the film. The slim hysteresis loop obtained at higher frequencies indicates a minor

contribution of domain switching and having mostly the contribution from the dielectric permittivity [180].

The behavior of coercive electric field (E_c^+ and E_c^-) and the remnant polarization (P_r^+ and P_r^-) as a function of AC driven frequency is shown in Figure 14b. The increasing of the coercitivity for lower frequencies is due to both conduction and dielectric contribution. Since E_c indicates the field necessary to perform the switching of the ferroelectric domains, the electric field where $P = 0$ is not the coercive field because the hysteresis loops is pre-saturated for lower frequencies, and the linear response of the polarization observed for higher frequency does not indicate if the material is even a FE material.

4.1.4. Nanoscale Domain Properties in Polycrystalline Strontium Barium Niobate Thin Films

In order to investigate the static domain structure in relaxor materials, PFM technique has been successfully applied to study the polar structure of single crystals, ceramics, and thin films compounds [149]. The typical topography and out-of-plane piezoresponse images for relaxor SBN thin film are shown in Figure 15a and Figure 15b, respectively.

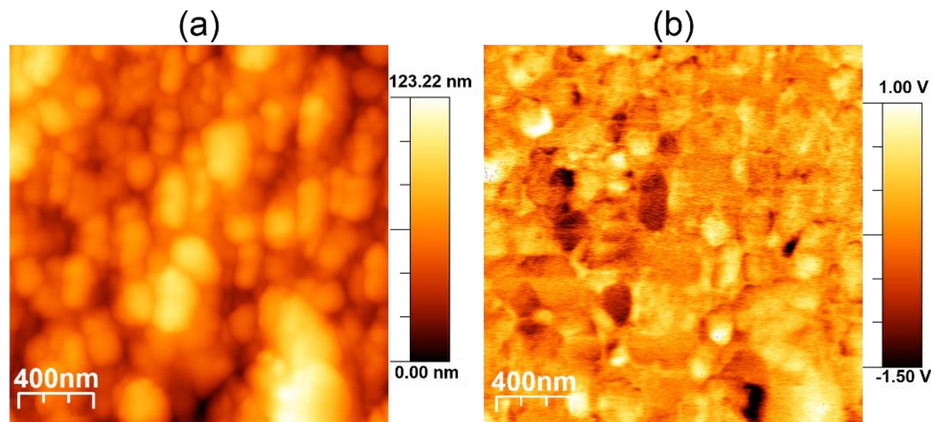

Figure 15: Typical topography (a) and piezoresponse (b) image of the SBN75 thin film obtained in an area of 2×2 µm^2.

The topography shows a distribution of grains with different sizes and shapes. Besides, the image reveals a non-flat surface, with average grain size around 200 nm and root mean square (RMS) roughness of 20 nm. Other SPM images have been taken in different regions of the film surface in order to verify the uniformity of the topography in our film. The existence of three types of contrast (bright, dark and “noisy”) are revealed in the PFM image (Figure 15b). These regions are characteristic of opposite out-of-plane polarization vectors (180º domains). Bright and dark contrast regions are an indication of polarization vectors of the FE domains

pointing towards the film surface (c^+ domain) and the bottom electrode (c^- domain), respectively. The "noisy" contrast observed in the PFM image, being attributed generally to an amorphous phase or/and non-FE phases [5]. In addition, the intermediate contrast could be attributed to very fine polar structures in the SBN film, probably related to PNRs [181]. Nevertheless, it worth to mentioning since the tip dimension is around 10 nm, it is not possible to resolve domains less than this PFM setup condition.

The domain cross-section was analyzed through four grains (from line A to B, as indicated in Figure 16a). Figure 16c shows the profile of the piezoresponse signal and the correspondent topography related to these specific grains. The grain 1, for example, shows a dark contrast, denoting a domain with the polarization vector oriented towards the bottom electrode, while the grain 2 and 3 possess "*noisy*" contrast, exhibiting a low positive and negative piezoresponse signals, respectively, compared with the grain 1. The grain 4 showed a bright contrast indicating a domain with polarization vector opposite to the grain 1. In general, it can be seen that the polarization distribution in the surface varies from grain to grain, giving another possibility of grain visualization.

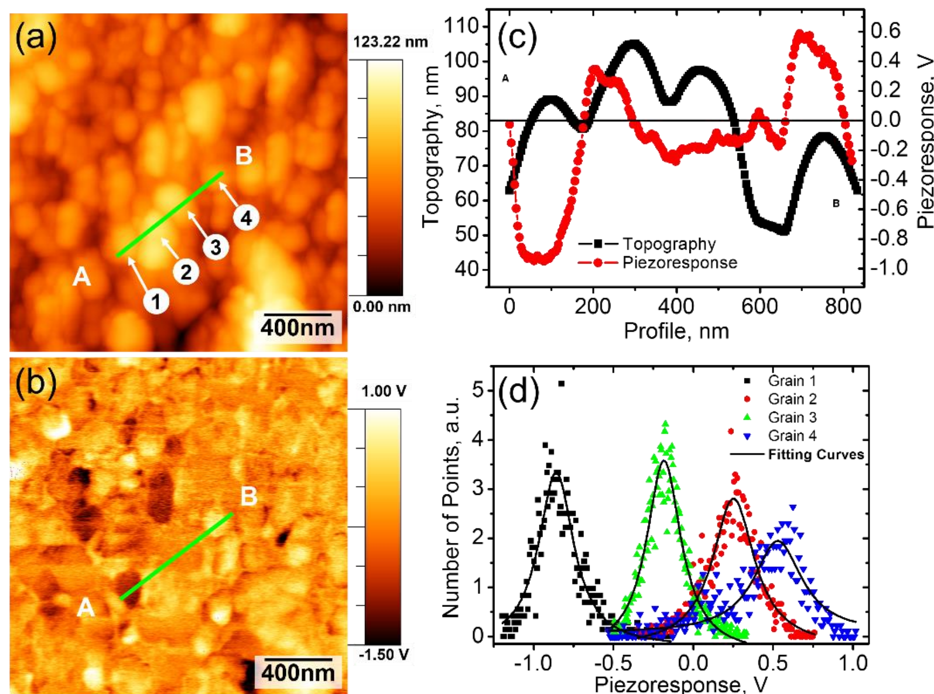

Figure 16: Topography (a) and piezoresponse (b) images and (c) cross-sections across the grains with different domain polarization vectors of SBN thin film and the histograms of the distribution of piezoelectric response inside the grains depicted in Figure 16(a-b).

It was found that the FE domains in SBN thin film are irregulars with random orientation of the polarization within the grains, which either are single domains or represent a distribution

of weak piezoresponse signal. These weak piezoelectric regions are expected for a RE ferroelectric even for temperatures above and below T_m, and can be due to both with locally broken symmetry and the existence of PNRs [171, 182]. The microscopic origins of PNRs in SBN thin film are closely linked to spatial fluctuations of RFs caused by structural disorder and related charge inhomogeneity [126].

Among a number of materials crystallizing in the TTB structure and exhibiting the relaxor behavior, the SBN is a typical representative [177]. For the SBN, the A1 positions are occupied only by Sr^{2+}, the A2-sites are filled with both Sr^{2+} and Ba^{2+} cations, whereas the *C* channels remain unoccupied. However, as there are just five Sr and Ba atoms for the six A1 and A2 positions, one of the A-sites continues empty [183]. It is widely accepted that disordered chemical structure is the main cause for the unique properties of relaxors, but it is still unclear how large the chemical disorder has to be a ferroelectric material to become a relaxor [40]. The SBN undergoes an order-disorder transition from paraelectric to a polar state with spontaneous polarization pointed towards the *c*-axis upon cooling (uniaxial relaxors). This polarization is caused by displacement of the central atom (Nb^{5+}) of the octahedral located at the B-channel in the SBN disordered structure.

Unpredictably, some grains of the SBN has exhibited strong dark and bright contrasts, indicating the existence of a piezoelectric response activity without the applied electric field suggesting an existence of built-in electric fields in this film. The imprint effect, also known as a self-polarization, is an important degradation effect in FE films and it is defined as a preference of one polarization state over the opposite one due to an internal built-in electric field [149, 184]. Since the built-in fields can result in enhanced dielectric properties and directly influence the switching characteristics, comprehending the origin of such phenomena is important for practical applications [185]. The origin of the built-in electrical field is generally associated with different factors, such as strain relaxation (flexoelectricity) [186]; stress induced by film/electrode lattice mismatch or clamping; domain pinning induced by oxygen vacancies, contributing to the non-switchable polarization in domains [187, 188]; degradation of ferroelectric properties in film/electrode surface layer, so-called Schottky effect [189]; structural defects, and others. The evidence of self-polarization is typically found in asymmetries on the hysteresis loops at macro and nanoscale, which will be discussed further in local in investigations at nanoscale of the SBN thin film.

The important information on the distribution of the local polarization can be done through the analysis of the PFM histograms. The histograms are obtained by counting the number of the pixels on the PFM image corresponding to a given piezoresponse signal [149].

The deconvolution of the piezoresponse histograms in several peaks is a way to analyze the valuable information on relative populations of different domain states. The average piezoresponse value is obtained from the peak position while other important information, such as the half-width of the peak, also can be obtained. The broadening of the peak is an indicative of coexistence of several polarization directions in polycrystalline with random orientation in thin films.

The histogram obtained inside the grains (four grains indicated in the profile analysis in Figure 16a) is illustrated in Figure 16d, indicating that the grains do not possess a single value of piezoresponse, but a distribution of the piezoelectric signal. This is an indicative that inside grains there are domains states with several crystallographic orientations reflecting mainly by the random electric field (i.e. by the built-in fields). These fields can cause a preferred reorientation of PNRs forming a smooth piezoresponse distribution inside the grain due to the inhomogeneity of these local fields [171, 190].

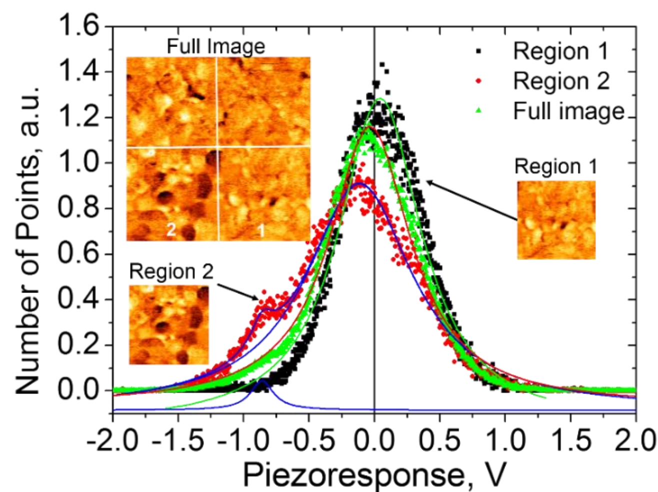

Figure 17: The piezoresponse histograms observed in different regions of a PFM image.

In addition, we have obtained the histograms of three different separated regions inside a unique PFM image (2×2 μm^2) of SBN thin film prepared by the chemical method. These histograms are shown in Figure 17. An analysis of the histograms for different regions of the PFM image is important to verify the effect of grains with self-bias in the piezoresponse distribution of the SBN thin film surface. The PFM image of SBN thin film was split into two regions: one with no presence of a grain possessing dark or bright contrast (i.e. with no strong piezoelectric signal) depicted in Figure 17 as region 1, and other with the presence of grains with probable self-polarization, depicted as region 2. For region 1, the piezoresponse distribution is approximately symmetric. On the other hand, the region 2 is characterized by an asymmetric distribution in the piezo histograms as well as the presence of a “negative” shoulder

around a piezoresponse value of -0.8 V. This is effectively an indicative that regions exhibiting negative piezo signal (in this case, it is rather clear the grains with domains possessing polarization vectors oriented toward the bottom electrode) are essentially larger than areas with positive piezoresponse (domains with polarization vectors oriented toward the free surface). Moreover, full image was analyzed with respect to its piezoresponse distribution. It is clearly observed that the distribution is nearly symmetric, adding a small elevation around the piezoresponse related to the region 2.

Figure 18(a-e) illustrates the domain structure of SBN thin film scanned after applying different DC voltage amplitudes in the area. PFM images observed in Figure 18a were obtained at 0.3 Hz of scan rate, scanned from up to down and from left to right, respectively, with 512 vertical lines. The DC voltage amplitudes applied on PFM acquisition were 0 V (before poling), +5 V, -5 V, and 0 V (after poling), in a row. The images were obtained individually at about the same area (2×2 μm^2), acquired only after a few seconds between the previous poling and the image after poling. The DC voltage amplitude applied were high enough to cause a domain switching, in order to verify the stability of ferroelectric domains in the grains.

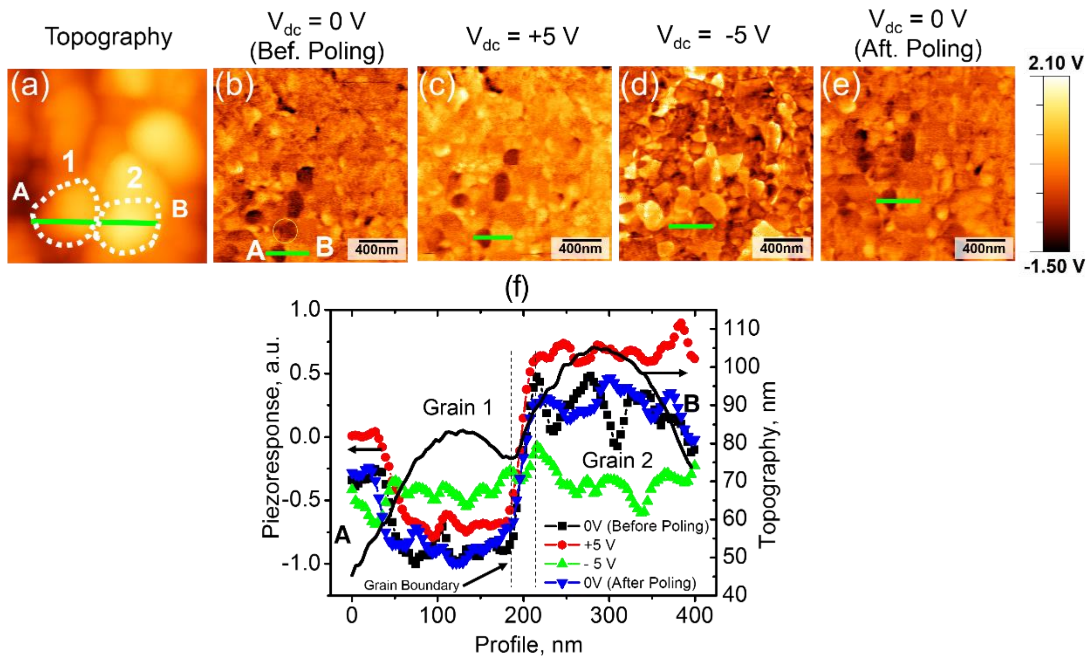

Figure 18: (a) Topography and analysis of the piezoresponse in SBN thin film applying (b) V_{dc} = 0 V (before poling), (c) V_{dc} = +5 V, (d) V_{dc} = -5 V and (e) V_{dc} = 0 V (after poling). (f) Cross-sectional analysis of the grain boundary between two grains indicated in (a).

Figure 18f shows the cross-sectional analysis of two adjacent grains with opposite polarization states over the line AB given in the Figure 18a. It is quite clear from the cross-section analysis that the grains 1 and 2 exhibit different responses to DC poling fields applied on surface. While grain 2 switches the domain orientation with an application of a reverse DC

bias, the grain 1 remains non-switchable for a DC poling field of + 5V. Moreover, with -5 V of DC bias, the piezoresponse of both grains is nearly the same, with a decreasing of the piezoresponse in the grain 1. This effect could be attributed to the local contribution of non-switched FE domains in the neighboring grains. In polycrystalline materials, the grain boundaries can strongly affect the switching kinetics [149], so that causing a decreasing in the local effective electric field and, consequently, decreasing the self-polarization effect in the grain 1.

The piezoresponse distributions related to PFM images of SBN scanned with different DC applied voltages are shown in Figure 19a. For 0 V before poling, the distribution is nearly symmetric and the peak of maximum exhibits a small shift to negative values. After applying +5 V, the peak is shifted proportionally to positive values, indicating that the DC poling was sufficient to cause a switching of some domains in the scan area. Nevertheless, we observed the presence of a shoulder around -0.8 V of piezoresponse, suggesting that DC field was not enough to induce a switching in some ferroelectric domains, as we can observe some grains with dark contrast, possessing a self-polarization with same polarization direction before the poling. Thereafter, a DC poling field with -5 V was applied, being sufficient to shift the peak of the distribution proportionally to negative values. However, the shape of the distribution is rather asymmetric, indicating that some areas have not been switched in this case as well. The piezoresponse distribution with -5 V was fitted with two Gaussians distributions, indicating a distribution of domains around +0.5 V. Finally, we performed a PFM scan with 0 V of DC poling. Practically has been observed the same piezoresponse distribution compared to PFM image with 0 V (before poling), suggesting that all domains that have been switched on the poling process were unstable, reverting back to the initial polarization state after ~30 min the application of A -5 V of a DC bias.

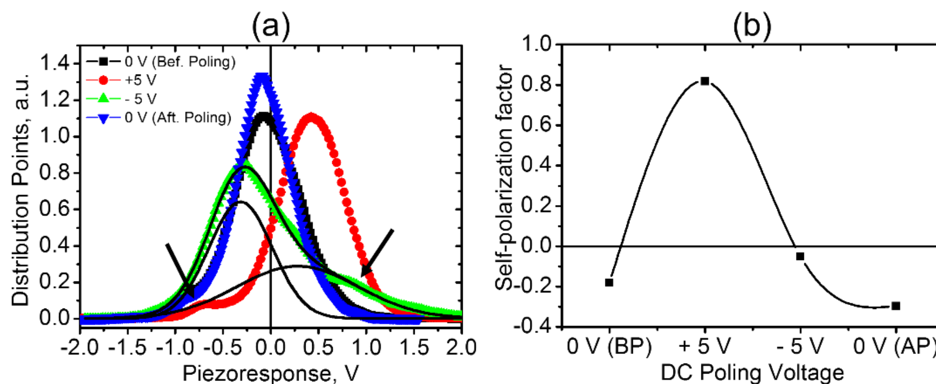

Figure 19: (a) Piezohistogram and (b) the self-polarization factor of the respective PFM images of SBN thin films referred to Figure 18.

Considering the piezoresponse histograms, the distribution of oppositely oriented domains in the SBN thin film with different DC poling fields (0 V BP, +5 V, -5 V, and 0V AP) was further analyzed by the integral characteristics of domain distribution. The difference between all positive domains $\int_0^{+\infty} N(\nu)d\nu$ and all negative ones $\int_{-\infty}^{0} N(\nu)d\nu$, divided by the number of all domains is defined here as a self-polarization factor β, in which $N(\nu)$ is the population obtained from piezohistogram [191]. Here, it is noteworthy that the self-polarization factor was used mainly to analyze the domain population distribution after applying different DC poling field.

$$\beta = \frac{\int_0^{+\infty} N(\nu)d\nu - \int_{-\infty}^{0} N(\nu)d\nu}{\int_{-\infty}^{+\infty} N(\nu)d\nu}. \tag{36}$$

Figure 19b illustrates the domain population as a function of the DC poling field related to the PFM images represented in Figure 18a. Slightly self-polarized state was observed before poling, indicating that the average piezoresponse of negatively polarized domains is larger than positive ones. Applying a DC voltage of +5V, the β factor increases to 0.8, suggesting a switching to positive domains. However, after reversing the voltage (-5V), the domain population (positive and negative) was found to be equally distributed. After poling, the domain distribution returns to its initial inhomogeneous domain pattern. This spontaneous back switching can be attributed to the presence of a local built-in electric field [192], probably originated from the distribution of quenched RFs due to structural and related charge disorder of SBN thin film [193]. And the formation of non-switchable domains shown in this work can be an origin for the imprint and retention loss in ferroelectric SBN thin films [187].

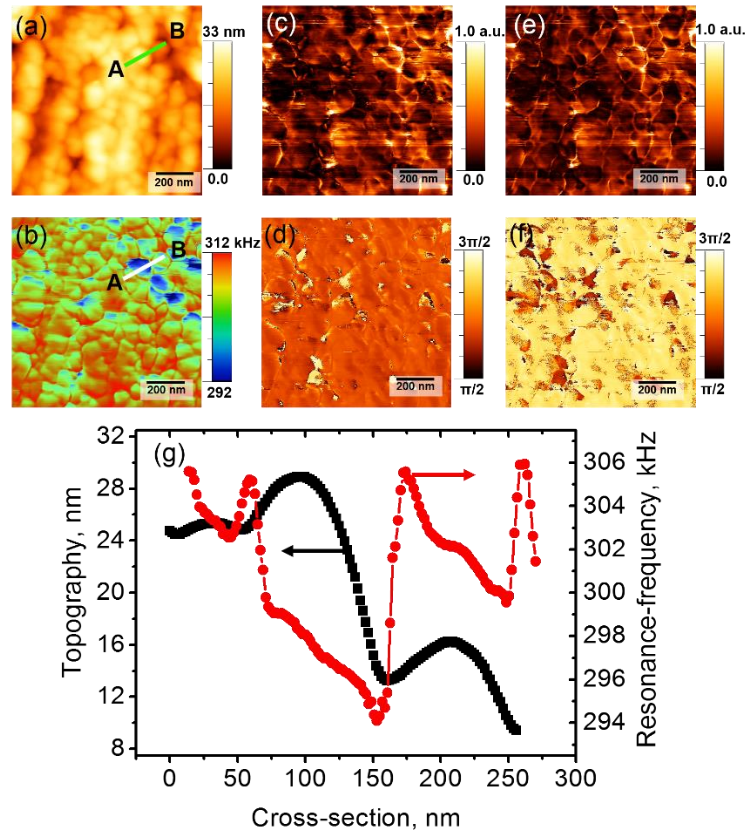

Figure 20: A 1 μm ×1 μm scan of SBN75 thin film obtained at room temperature in DART-PFM mode (a) the sample topography, (b) the resonance contact frequency (f_0), and (c), (d), (e) and (f) the experimentally measured R_1, φ_1, R_2 and φ_2, where R and φ are amplitude and phase of the DART-PFM image. $\Delta f = (f_2 - f_1) =$ 20 kHz was used for these measurements. A cross-section analysis of topography and mapping resonance contact frequency [indicated along the line *ab* in Figure 20a-b] is illustrated in (g).

PFM images obtained so far were obtained using the single frequency contact resonance (CR), in which the excitation frequency (AC driven frequency ~50 kHz) was applied far below the resonance contact in order to avoid an ambiguity in the measurements. Since relaxor SBN studied in this work was far above the T_c temperature, it is expected the presence of low piezoresponse regions in PFM images. Approaching the excitation frequency to the tip-sample CR, resonance amplification improves the signal-to-noise ratio (SNR) considerably, and the contrast observed in PFM amplitude images caused by shift in the tip-sample resonance contact frequency can be used to qualitatively infer the mechanical properties of the sample [194] (e.g. local elasticity measurements in FE material surfaces [195]). Therefore, the PFM contrast is strongly affected when the excitation frequency is very close to the contact resonance, undergoing a phase inversion whenever the driven frequency cross the resonance contact [196]. Therefore, care must be taken to avoid crosstalk between topography and the piezoresponse signal.

Figure 20a shows the sample topography while the DART measurements are shown in five images, from Figure 20(b-f) the respective values of f_0, R_1, φ_1, R_2, and φ_2. As characteristic for PFM images, the contrast in the phase images (d) and (f) show both polarized domains and a large area with the phase in 0 or 2π, indicating the absence of a ferroelectric domain. The low amplitudes (c) R_1 and (e) R_2 suggest a quite weak response typical for the SBN75 thin film which is far above the phase transition temperature. A large variation in resonance frequency f_0 in Figure 20b (~20 kHz) demonstrates the advantages of DART over single frequency PFM for higher sensitivity investigations [194]. Also, the variation of the resonance frequency on film surface indicates that the stiffness of the mechanical contact between the tip and sample changes accordingly to the roughness of grains and topography, as we can observe in Figure 20g [197].

4.1.5. Domain Switching and Local Piezoresponse Relaxation Dynamics of SBN Thin Films via SS-PFM

A Switching Spectroscopy Piezoresponse Force Microscopy (SS-PFM) was applied in the SBN thin films to understand the local switching properties. The SS-PFM mode was implemented on a commercial AFM (Ntegra Aura, NTMDT, Russia) in order to investigate the local piezoelectric response, using both conventional polarization imaging and a step voltage sweep spectroscopy methods to study the piezoelectric origin of the sample. During the PFM measurements, the AC probing (amplitude 1 V, frequency 50 kHz) was applied between a conduction tip (Budget sensor Multi75E-G: Si cantilever covered by Pt, spring constant 3N/m, resonance frequency 75 kHz) and the bottom electrode. The PFM response was detected via external lock-in amplifier (LIA) system (SR830, Stanford Research, USA).

To induce a local polarization state, the SS-PFM was carried out to verify the reverse domain characteristic behavior. The tip was fixed at a predefined position on the sample surface and voltage bias pulses of variable magnitudes V_{dc} and durations t_p were then applied [149]. During the application of the DC pulse, a probe with an alternating voltage V_{ac} was applied and each pulse was followed by measurements of the effective piezoelectric response $(d_{33})_{eff}$ as the value of the signal measured by the lock-in system. The dependence of $(d_{33})_{eff}$ on V_{dc} is referred to as piezoelectric hysteresis loops [46, 152]. The relaxation of induced polarization states was measured as a function of time between DC voltage pulses of variable magnitudes V_{dc} and voltage duration t_p in different grains in order to investigate the domain nucleation and growth mechanism of the FE domains in SBN thin films [198].

To understand the origin of different polarization states in some grains, the piezoelectric hysteresis loops were obtained locally in the interior of three different grains, as indicated by grain #1, #2 and #3 in Figure 21a and Figure 21b. The hysteresis loops for these grains are shown in Figure c. The slim hysteresis loops were clearly observed in areas with dark and bright contrasts, possessing small remnant d_{eff} and coercitivity. Normal ferroelectric-like hysteresis loops are observed in "noisy" contrast grains (grain #2 and #3) indicating the existence of a ferroelectric state in these grains. The shape of local hysteresis loops depends not only on the induced polarization but also on the depolarization rate after removal the DC external field, which is confirmed by the tilt of the loop on the delay time between the bias removal and the d_{eff} acquisition.

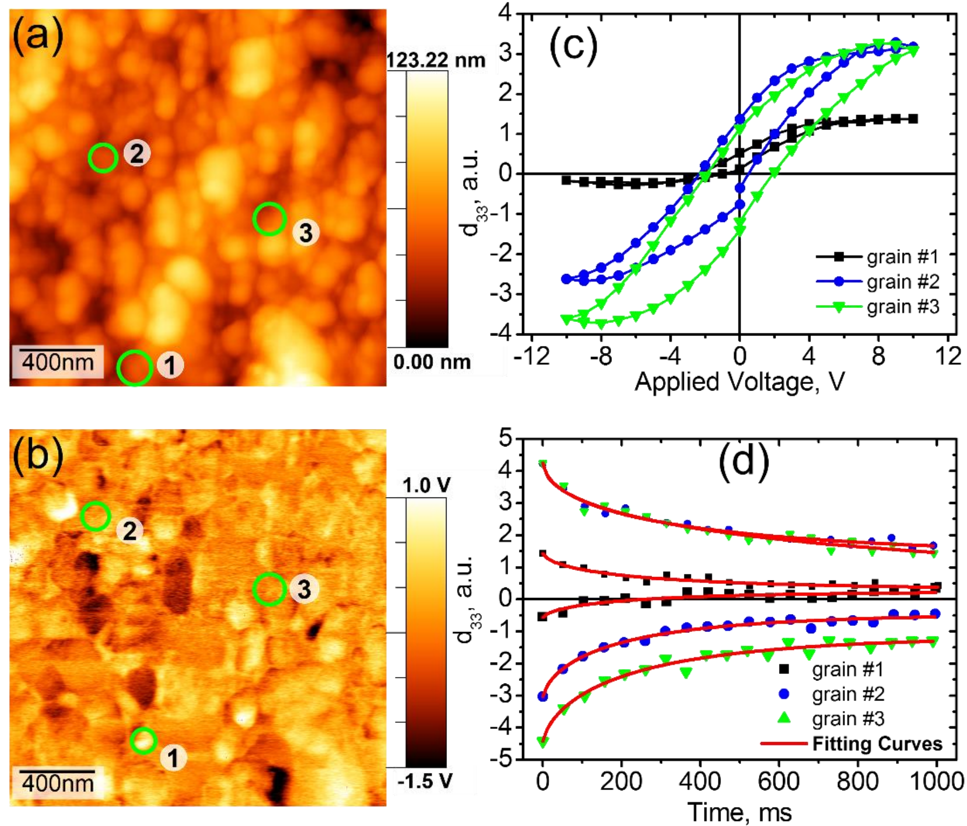

Figure 21: (a) Topography and (b) piezoresponse images of the SBN thin film. (c) Local hysteresis loops recorded at three different grains is indicated in (a) and (d) Polarization relaxation of piezoresponse as a function of time at different grains for the magnitude of ±10 V and duration of DC voltage of 100 ms.

The local hysteresis loops measured in grains with a bright area (e.g. grain #1) has exhibited a significant upward shift along the d_{eff} axis (as we can see in Figure 21c). The positive offset indicates the existence of a non-switchable polarization that is probably related to high internal bias field near the bottom electrode, pointing out that the grain #1 is self-polarized by a built-in field upon cooling through the phase transition temperature [199]. The external DC bias can not reorient the polarization or stabilize the ferroelectric domain after the reorientation near the electrode region, resulting in a shift of the piezoelectric hysteresis loops, and the hysteresis is due to orientable polarization of the area close to the tip [46]. Moreover, must be taken to account that the phenomenon of asymmetric switching is attributed not only to the presence of a built-in electric field at the bottom interface (as already described) but also to the mechanical stress contribution exerted by the SPM tip (related to the 90º domain rotation of the polarization vector) [200].

It is still not resolved why only some grains or clusters are self-polarized and the problem is still under debate in the scientific community. One possible explanation for the self-polarization effect appearance in grains can be related to their specific grain crystallographic

orientations. Despite the SBN75 thin film structure is in PE at room temperature (T_m = 221 K at 10 kHz frequency) [201] on the macroscale, the local symmetry of PNRs is tetragonal, and each grain may possess local properties, depending on their specific crystallographic orientations. *A priori*, in the case of grains with parallel and antiparallel orientation related to the built-in electric field, a large piezoelectric response could be induced. Other explanations for the presence of self-polarization include stoichiometric fluctuations in some grains, oxygen vacancies, and other defects, typically of RE ferroelectrics [182, 188].

The relaxation of piezoelectric response d_{33} for the grains #1, #2 and #3 is shown in Figure 21d. The induced piezoresponse was observed to be unstable and relax rather fast within 1 second after shutting off the DC external bias. The relaxation of induced domains showed to be influenced by the polarization state of grains, the amplitude (V_{dc}), and the pulse duration (t_p) of the DC voltage bias. The magnitude V_{dc} was chosen to be larger than the estimated coercitivity obtained from the local hysteresis loops (see Figure 21c).

The induced piezoresponse decay was described by the Kohlrausch-Williams-Watts (KWW) function. The KWW function or the stretched exponential relaxation function is observed in complex systems from intricate behavior of liquids and glasses to structures and dynamics of atomic and molecular clusters, describing properly the phenomena of the time-dependent dynamic process [134]. The function is described by

$$d_{33} = P_0 + P_1 \exp\left(-\frac{t}{\tau}\right)^{\beta} \tag{37}$$

where t is the time, P_0, P_1, τ , and β are the fitting parameters [198, 153]. For the stretching exponential β between 0 and 1 (β = 1 is the normal exponential function and is referred as a Debye simple relaxation) and the time t from 0 to $+\infty$ (τ is the characteristic relaxation time) [202]. Lines in Figure 21d refers to the theoretical fitting using the KWW equation. For the grain #1 the obtained relaxation time τ were 202 and 240 ms while β values were 0.66 and 0.64 for pulses of +10 and -10 V, respectively with $t_p \cong 100$ ms of pulse duration. For the grain #2, we observed, for the same condition, relaxation time τ were 187 and 342 ms while β values were 0.69 and 0.60. Finally, for grain #3, the values of τ were 219 and 880 ms and β values were 0.69 and 0.52, respectively for +10 and -10 V of DC bias.

The polarization direction of the grain #1 (Figure 21b) is reversed when a V_{dc} = -10 V is applied. However, the domain state rapidly decays to its original polarization, indicating a stable and a non-switchable polar state. Referring to the grains #2 and #3 ("*noisy*" contrast) the

ferroelectric domain was switched with an application of a reverse DC bias and maintaining after the DC removal, indicating switchable polar states. Comparing the grain #2 with the grain #3, the effective d_{33} induced piezoresponse was relatively lower when applied reverse negative pulses, probably due to the contribution of nearest-neighbour interactions between polar microregions [172] and the polarization state of adjacent grains [200]. Moreover, grains presenting a self-polarization effect due to the high internal electric field may prevent the dipole alignments along the applied DC bias direction when compared to the grains in the ferroelectric state ("*noisy*" contrast). Other effects have also to be considered in the case of asymmetry of induced-state grains by DC bias, such as domain pinning due to the oxygen vacancies, mechanical stress induced exerted by the tip [203], and grain size effects that can influence significantly the properties of polar nanoclusters [46].

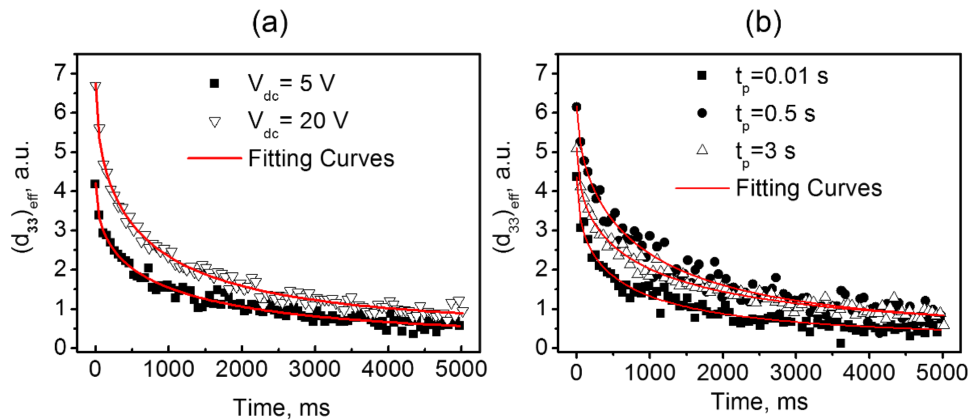

Figure 22: Piezoresponse relaxation curves of SBN thin film for (a) 5 and 20 V at 100 ms of pulse duration and (b) for 0.01 s, 0.5 s, and 3 s of pulse duration at 15 V of DC voltage amplitude.

Pulses with different voltages and durations were applied in grains with "*noisy*" contrast to investigate both time and voltage dependences of the piezoelectric response. Figure 22a describes the voltage dependence of effective d_{33} for 5 and 20 V of amplitude at 100 ms of duration, while in Figure 22b shows the pulse duration dependence for pulses with 0.01, 0.5, and 3 seconds at 15 V.

For magnitudes higher than 5 V, we expected the existence of induced single domains in our films. These induced-domains were found to be completely relaxed and reversible within less than a second, indicating that the kinetic of domains have a quite short relaxation and a high response to an external bias [153]. The relaxation mechanisms of induced-domains are governed by the same depolarizing process described in normal FE materials. The bound charges at the electrode-ferroelectric interfaces set up a depolarization field (E_d) that tends to oppose the polarization in domains [204]. The polarization bound charges will be induced at the surfaces, but compensated by free charge carriers in a limited extent, resulting in an

incomplete compensation of the polarization charges [205]. Such an incomplete charge compensation should induce a depolarization field E_d inside the ferroelectric layer, with opposite to that of the induced ferroelectric polarization [206].

With the increasing of external static voltage from 5 V to 20 V and the DC bias duration fixed at 10 ms, the characteristic time (called also relaxation time) τ increases. In this case, the parameters of KWW function obtained in the fitting of the experimental results showed an almost linear increasing in the relaxation time τ from 404 to 784 ms in this applied voltage interval. The β-factor has remained broadly unchanged ($\beta \approx 0.51$) for all values of amplitude voltages. Besides, for a pulse duration of 3 seconds and amplitudes in the interval range between 5-20 V, both τ and β were found practically constant ($\tau \approx 883$ ms and $\beta \approx 0.51$). The coefficient of determination R^2 obtained in the KWW fitting curves did not exceed the value of 0.95.

We expected an increase of the polarization in the induced polar states with the increasing of the external DC electric field. This effect is due to the increase the number of dipoles oriented along the field direction. In order to explain the increasing of relaxation time τ as a function of the DC electric field, a dipole glass model was proposed by Gui *et al.* [172] performing many simulations in perovskite structures. It was predicted a peak shift to lower flipping frequency distribution of dipoles, i.e., moving the spectra to longer relaxation times as the DC external voltage increases.

The values of the local induced piezoresponse have shown an increasing for lower pulse durations of the DC bias (from 10 to 500 ms), as we can observe in Figure 22b. This is an indicative that a saturation of flipping dipoles has not been achieved yet, promoting gradually the reorientation of dipoles overt the DC external field direction. Nonetheless, for longer pulse duration (i.e., for pulse durations longer than the characteristic times, $t_p > \tau$), it was observed a saturation and a decreasing of the effective piezoresponse $(d_{33})_{eff}$ in our film. This may be related to the formation of a depolarizing field (E_d) on the FE layer localized under the tip during the SS-PFM measurement. Probably, the E_d is mainly due to space charge contribution on film surface that is compensated by free charges [206].

We have measured local hysteresis loops from a specific grain possessing "*noisy*" contrast in the investigated SBN thin film. Through application of different magnitudes and pulse durations of DC bias, it is possible to study the time and voltage dependences of switching and electromechanical properties at nanoscale of FE materials. The piezoelectric hysteresis loops were obtained at DC voltage $V_{dc} = 10$ V with $t_p = 10$, 500, and 3000 ms and it is possible to verify the correlation between time and hysteresis shapes in Figure 23a.

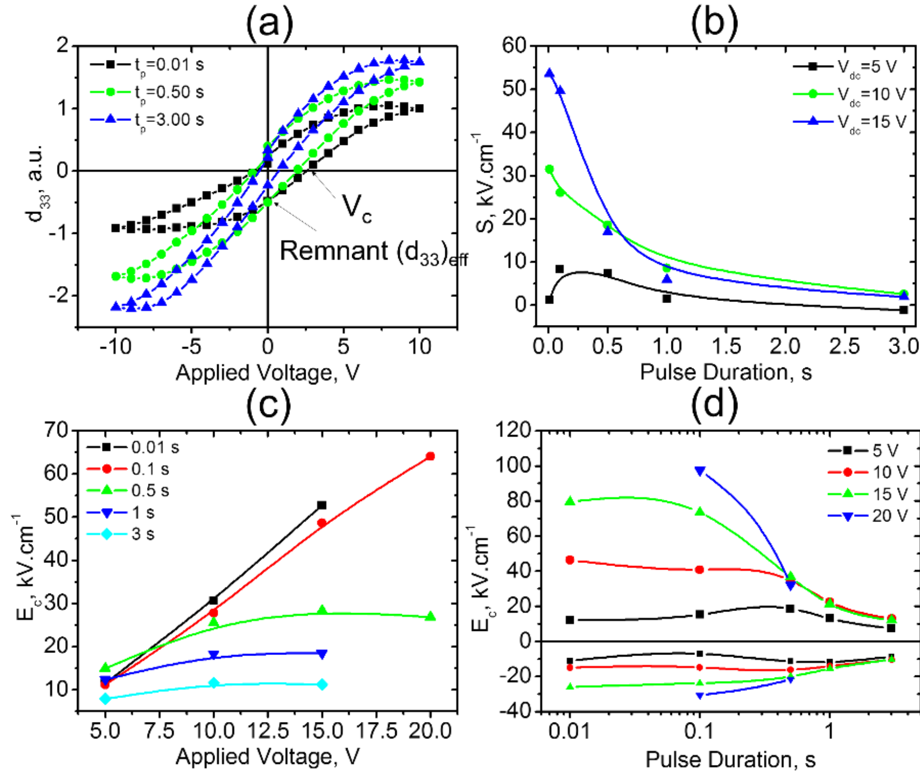

Figure 23: (a) Local hysteresis loops of SBN thin film at DC pulses voltages of 10 V with pulse duration t_p = 10 ms, 500 ms, and 3000 ms. (b) Pulse duration dependence of local imprint effect $S = (E_c^+ + E_c^-)$ at different voltages. (c) Effective coercive field $E_c = (E_c^+ - E_c^-)/2$ as a function of DC amplitude voltages, and (d) coercive electric field as a function of pulse duration for positive and negative DC pulses. (Here the lines are guides for the eyes)

For pulse durations longer than relaxation times, the piezoelectric response as a function of DC bias has presented a slim shape (see the blue line in the color version in Figure 23a). Moreover, it was observed a shift towards the positive voltage, characterizing a local imprint effect similar to that reported earlier [201], and a decreasing of the saturated piezoresponse in the hysteresis loops for lower pulse durations of DC applied voltage. The persistence of local ferroelectric features, such as in piezoelectric hysteresis, well beyond the Curie temperature, indicates the existence of nanopolar clusters that can be oriented by the external field. Asymmetries observed in PFM hysteresis emerges beyond T_c, suggesting the existence of random fields that becomes conspicuous in the absence of long-range ferroelectric order [207].

The pulse duration dependence of the local asymmetry (described as $S = E_c^+ + E_c^-$, in which E_c^+ and E_c^- are the positive and coercive electric fields) is illustrated in Figure 23b. The DC applied voltages used were 5 V, 10 V, and 15 V respectively. Increasing the pulse duration from 1000 ms to 3000 ms, the asymmetry in the hysteresis loops decreases and there are practically no change in asymmetry at 3000 ms of pulse duration. However, for very short pulses of DC external bias, the asymmetry observed in coercitivity increases as the applied

voltage increases. As it was already discussed, for pulses longer than the characteristic times, the influence of space charges localized at the film/electrode and film/tip interface may be one possible reason to explain the observed saturation of effective d_{33} and the relaxation of induced FE domains [5].

The voltage dependence of average coercive electric field, given by $E_c = (E_c^+ - E_c^-)/2$, is shown in Figure 23c. The observed coercive electric field increases as the voltage amplitude increase for lower values of t_p, indicating that more polar domains were switched along DC external bias direction and, consequently, a higher external electric field is needed to bring the local net polarization to zero in this condition. For higher values of t_p in which the DC bias is switched on, the values of E_c decreases significantly. The decreasing of E_c is probably related to depolarizing process due to space charges at the interface, being necessary to bring to zero the local net polarization.

Figure 23d shows the behavior of E_c^+ and E_c^- at different applied voltages as a function of $\log_{10} t_p$. Clearly, the asymmetry of positive and negative coercive voltages is evident for lower t_p and higher V_{dc}. A quantitative analysis was performed from the pulse and voltage dependence of E_c^+ and we fitted using a simple exponential function of the pulse duration t_p,

$$E_c = E_1 + E_{0c} \exp(-t_p / \tau_c), \qquad (38)$$

where E_{0c} is the time independent factor and τ_c is a fitting parameter related to the local polarization switching. Figure 24a and Figure 24b show the fitting curves and the fitting parameter related to the pulse duration dependence of E_c^+ and E_c^-, respectively, in our of SBN thin film.

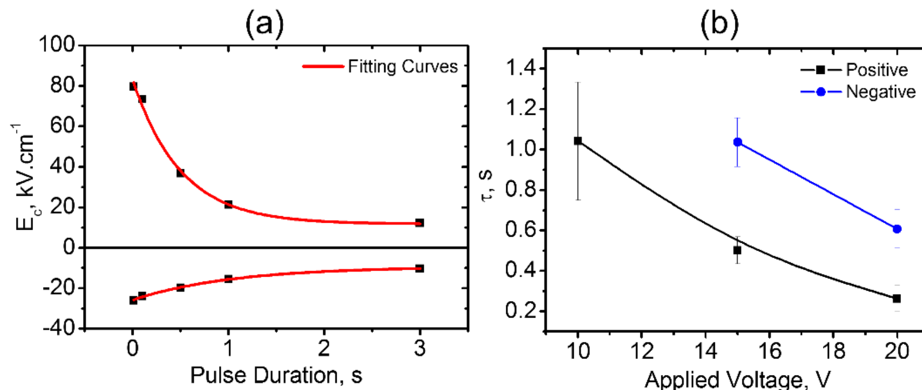

Figure 24: (a) Positive and negative coercive electric field E_c^+ as a function of t_p for 15 V of a DC applied voltage, fitted with simple exponential form, given by $E_c \cong E_{0c} \exp(-t_p/\tau_c)$. (b) Fitting parameter τ_c as a function of applied voltage. (Lines are just guides to the eyes).

We can clearly observe from Figure 24b that the values of characteristic times related to positive and negative pulses are almost linear within the interval from 10 V to 20 V. The mathematical meaning of τ_c given here is just the value of the time required for the coercive field decreases the factor of e^{-1} from its initial value. Physically speaking, we could attribute such parameter to the relaxation phenomena in SBN thin film. For higher applied voltages we observe a decrease of both positive and negative τ_c, suggesting again the existence of a depolarizing process that contributes to the decrease of the coercive electric field. The relaxation of induced domains becomes linearly faster depending on the applied voltage due to the contribution of space charges in the interfaces.

4.1.6. Summary

$Sr_{0.75}Ba_{0.25}Nb_2O_6$ thin films (SBN) have been prepared by the polymeric method in order to investigate their physical properties. Microstructure analysis has revealed a spongy character in the SBN thin film morphology. SEM images exhibited a high degree of porosity and homogeneous spatial distribution with pores of different sizes (~20-100 nm) and shapes. The SEM cross-sectional analysis has also allowed both quantitative and qualitative information about the relaxor material. The SEM qualitative analysis showed that the spongy features is found along the film thickness and are more concentrated between the film layers deposited using a polymeric resin by spin-coating. The quantitative analysis has enabled the investigation of chemical distribution in the cross-section of the SBN thin film. The Rietveld refinements have corroborated the tetragonal structure and the stoichiometry of the studied film. The relaxor behavior of the material has been confirmed using the Vögel-Fulcher (VF) analysis. The transition temperature found was T_m = 221 K at 10 kHz in driven frequency, and an apparent lowering of 100 K was observed in comparison to single crystals of the same composition. PFM studies have shown a grain size distribution with grain size ~200 nm and roughness of ~20 nm. Piezoresponse images have revealed grains possessing self-polarization and regions with negligible piezoelectric responses, which are typical of relaxor materials and probably related to PNRs. Piezoresponse histograms have indicated the existence of FE domains with various polarization directions (even inside of the grains) and the self-polarization effect. The imprint effect is probably due to the inhomogeneity distribution of random electric fields originated from structural and its related charge disorder in the SBN thin film structure. Most polar domains were stable and switchable when applied a DC voltage before PFM measurements, while for some domains showed to be unstable and non-switchable. Random

fields and neighboring polar microregions contribution were considered to be responsible for the appearance of this effect. DART-PFM studies have revealed that the variation of the resonance frequency observed on film surface indicates that the stiffness of the mechanical contact between the tip and sample changes accordingly to topography. Local polarization relaxation was investigated using a piezoresponse force microscopy. Local ferroelectric features remain well beyond Curie temperature, indicating the existence of PNRs that can be reoriented accordingly the application of an external bias field. Asymmetry in the hysteresis loops has been observed in SBN thin film for higher voltages and lower pulse times of DC bias. The studies of relaxation have revealed a voltage and time dependence of the relaxation time τ for pulses of 10 ms, but for higher pulse durations (t_p ~ 3000 ms) the relaxation time is practically constant and voltage independent. The mechanism suggested here for the relaxation phenomena in relaxor SBN thin film is the same in normal ferroelectric. However, we found clues of linear dependence of depolarizing fields with the amplitude of DC external bias which could be a result of the formation of space charges near the tip.

4.2. INVESTIGATION OF POLAR STRUCTURE IN RELAXOR THIN FILM OF $Pb_{0.91}La_{0.09}Zr_{0.65}Ti_{0.35}O_3$ (PLZT)

This section is devoted to the investigations of the nano e microscale properties of the PLZT thin films prepared by the polymeric method. Effects of the thickness of switching and relaxation properties of ferroelectric polar domains will be presented here as well as the effects of thickness on structural, grain size and local piezoelectric properties. Furthermore, a cross-sectional PFM investigation will be presented in polycrystalline random oriented PLZT thin film.

4.2.1. Structural Properties of PLZT thin films

XRD measurements were carried out at room temperature in order to investigate phase purity and other structural properties of polycrystalline randomly oriented PLZT thin films using a Rigaku Ultima IV diffractometer with CuK_α (1.5406 Å) radiation[*]. The structural parameters were obtained using the Rietveld refinement method [141]. To refine the structure, we used as initial parameters an orthorhombic phase with $Pmmm$ space group, where the Pb^{2+} and La^{2+}cations occupy sites at (0, 0, 0), Ti^{4+}/Zr^{4+} and O_I^{2-} occupy sites at (1/2, 1/2, z), and O_{II}^{2-} occupy sites at (1/2, 0, z). The refined parameters obtained include background, scale factor, zero correction, peak width, cell parameters, positional coordinates, and isotropic atomic displacements. Anisotropic atomic displacements for Ti^{4+}/Zr^{4+}, O_I^{2-} and O_{II}^{2-} have been used but with no improvement in the *R*-factors. Through the refined parameters, it is rather convenient to evaluate the microstrain, $\Delta d / d$, and the crystallite size, *D,* of the PLZT thin films according to the modified Williamson-Hall analysis[†] [138].

Figure 25a shows the XRD patterns of PLZT thin films prepared by the modified Pechini technique[‡] pyrolyzed at 300 ºC for 30 min and a final crystallization from 400 ºC to 700 ºC for 1 hour. The reflections Pt(111) and Pt(200) shown in Figure 25 are attributed to cubic phases of the Pt substrate with the space group $Fm\bar{3}m$ and lattice parameter a = 3.892 Å. The indexed peaks (*hkl*) are related to the orthorhombic phase of the PLZT with space group *Pmmm*. The Figure 25a illustrates the XRD pattern of the film crystallized at 400 ºC, illustrating a typical feature of an amorphous material while it has been observed a tendency to crystallize into the

---

[*] Additional information about the x-ray diffraction technique used in this work, check the section: "3.Experimental techniques and materials processing, 3.2.1. X-ray diffraction analysis."
[†] These parameters have already been published and they can be seen along with discussion in detail elsewhere [138, 270].
[‡] The details of the material synthesis go to section "3.*Experimental techniques and materials processing*".

perovskite structure for crystallization temperatures ranging from 500 ºC to 700 ºC, respectively. Better thermal condition for the thin film crystallization was obtained at 700 ºC for 1 h, since the peaks related to the perovskite phase become stronger and better defined at higher crystallization temperatures. Figure 25b shows XRD pattern of these PLZT thin films with thickness ranging from 240 nm to 540 nm. No additional phase was found in PLZT thin films. An agreement between the observed and calculated pattern in this figure is an indicative of a good fit.

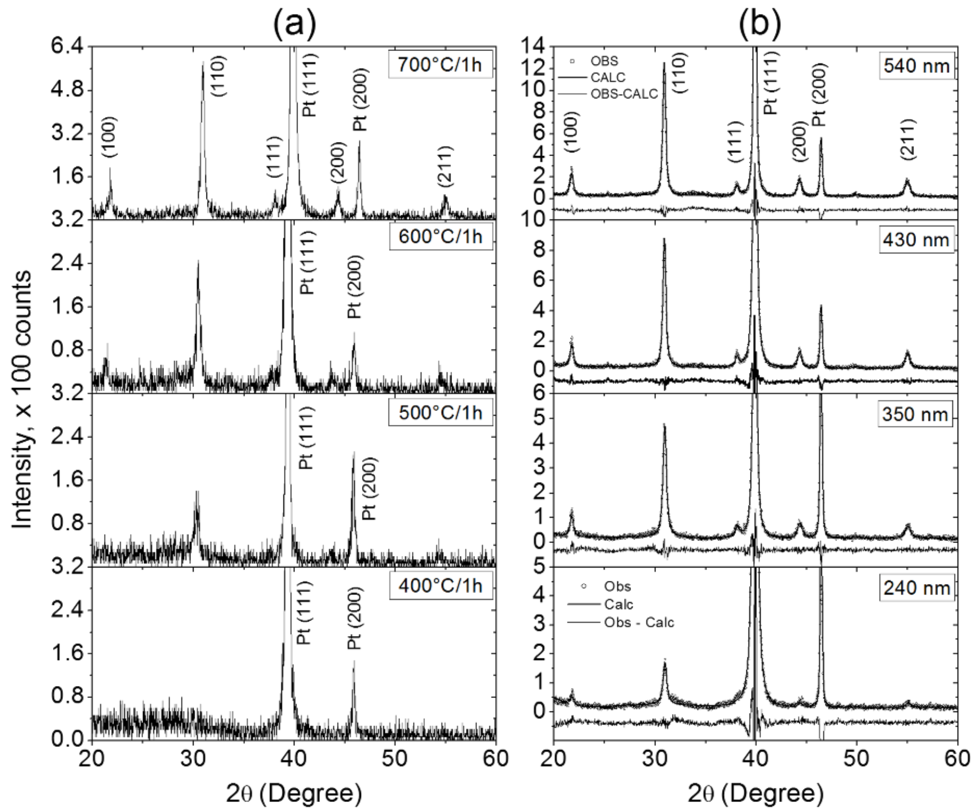

Figure 25: XRD pattern diffractions of PLZT film deposited on Pt (100)/SiO_2/Si substrates prepared for (a) different film thickness (ranging from 240 nm to 540 nm) crystallized at 700 ºC for 1h and (b) different annealing temperature for the film with 550 nm in thickness. All films were pyrolyzed at 300 ºC for 30 min [138].

The positional coordinates for atoms (*x, y, z*) as well as the isotropic atomic displacement parameters (U_{iso}) obtained from Rietveld refinement for the PLZT thin films with different thicknesses are summarized in Table 2, while the lattice parameters, volume cell, the crystallographic R-factors, and GOF indices are given in Table 3. The lattice parameters are in good agreement with the PLZT ceramics of same nominal composition [208]. The small χ^2 values obtained for all data indicate good refinements. Accordingly to statistics, the χ^2 term is defined as the average of $\chi^2 = (1/N)\sum_i (y_{c,i} - y_{o,i})/\sigma^2[y_{o,i}]$, where N is the number of data

points*, $y_{c,i}$ is the calculated intensity, $y_{o,i}$ is the observed intensity, and $\sigma^2[y_{o,i}]$ is estimative of the standard deviation of the observed intensity in the ith peak. It can also be determined from the expected and weighted profile R-factors $\chi^2 = (R_{wp} / R_{\exp})^2$. Even for obtained small χ^2 values, it is necessary to verify the values of R_{wp} and R_p indices to conclude about the quality of fitness. R_{wp} weight the residual, given by $R_{wp}^2 = \sum_i w_i (y_{c,i} - y_{O,i})^2 / \sum_i w_i (y_{O,i})^2$, where w_i is defined as $1/\sigma^2[y_{o,i}]$, having a meaning of smallest statistical uncertainty. $R_{\exp}$ denotes the expected R-factor, a quantitative that is a rather useful concept that represents the "best possible R_{wp}", given by $R_{\exp}^2 = N / \sum_i w_i (y_{O,i})^2$, where the quantity $\sum_i w_i (y_{c,i} - y_{O,i})^2 = N$ [209]. Due to the lower number of data points in thin films when compared with single crystals or ceramics, it is expected the R-factors of the data refinements of thin films result in higher values. Though the R-factors are larger, the values of χ^2 are small and a slight difference between observed and the calculated intensities can be seen in Figure 25, indicating good refinements. In conclusion, the structural parameters obtained from the refinements can be considered significant and representatives in this work.

Table 2: Refined Structural parameters for the PLZT thin films at 240, 350, 430 and 540 nm in thickness.

Thickness	***240 nm***				***350 nm***			
Atom	***X***	***Y***	***Z***	***U_{iso}***	***X***	***Y***	***Z***	***U_{iso}***
Pb^{2+}	0.000000	0.000000	0.000000	14.59	0.000000	0.000000	0.000000	12.98
La^{2+}	0.000000	0.000000	0.000000	23.2	0.000000	0.000000	0.000000	3.91
Zr^{4+}	0.522830	0.522830	0.522830	4.74	0.505150	0.505150	0.505150	5.02
Ti^{4+}	0.522830	0.522830	0.522830	3.69	0.505150	0.505150	0.505150	30.51
O_I^{2-}	0.519989	0.524989	0.034989	80	0.519989	0.524989	0.034989	4.75
O_{II}^{2-}	0.533355	0.040355	0.534355	76.06	0.533355	0.040355	0.534355	7.54
O_{III}^{2-}	0.039355	0.536333	0.537355	77.41	0.039355	0.536333	0.537355	28.95

Thickness	***430 nm***				***540 nm***			
Atom	***X***	***Y***	***Z***	***U_{iso}***	***X***	***Y***	***Z***	***U_{iso}***
Pb^{2+}	0.000000	0.000000	0.000000	11.1	0.000000	0.000000	0.000000	10.61
La^{2+}	0.000000	0.000000	0.000000	15.45	0.000000	0.000000	0.000000	80
Zr^{4+}	0.467133	0.467133	0.467133	0.53	0.464678	0.464678	0.464678	0.04
Ti^{4+}	0.467133	0.467133	0.467133	35.47	0.467023	0.467023	0.467023	63.43
O_I^{2-}	0.507633	0.503365	0.030765	23.86	0.519989	0.519989	0.519989	55.4
O_{II}^{2-}	0.452806	0.037802	0.510870	0.77	0.533355	0.040355	0.534355	0.39
O_{III}^{2-}	0.131777	0.448613	0.546557	52.33	0.105121	0.541335	0.522663	21.87

*The atomic displacement parameters U_{iso} showed here are given in unit of 100 Å.

*Actually, N is considered as a quantity called of "degrees of freedom", denoted as the difference between the number of data points and the number of varied parameters. However, the latter can be ignored by considering that the number of data points is much greater than the number of variables.

Based on the peak intensities of the XRD patterns it was possible to evaluate the degree of *a*-axis orientation, given by the formula $\alpha = \sum I(h00) / \sum I(hkl)$, for films with different thicknesses. From the refined parameters, the microstrain ($\Delta d/d$) and the crystallite size (D) were also evaluated from the XRD data using the modified WH analysis [138].

Table 3: Calculated cell parameters, R-factors from Rietveld refinement, and crystallite size and microstrain obtained from WH analysis of the PLZT thin films as a function of thickness.

Thickness	*Lattice parameters and volume cell*					*R-factors and GOF*			*D (nm)*	*Δd/d (10^{-3})*
	a (Å)	*b (Å)*	*c (Å)*	*a / c*	*V_c (Å^3)*	*R_{exp}*	*R_{wp}*	*χ^2*		
540 nm	4.090(4)	4.096(9)	4.086(3)	1.001(6)	68.48(5)	21.81	26.20	1.44	81±6	3.9±0.3
430 nm	4.085(4)	4.098(0)	4.088(3)	1.003(1)	68.44(6)	19.17	23.35	1.48	67±7	3.3±0.4
350 nm	4.097(2)	4.094(5)	4.089(3)	0.999(3)	68.60(4)	10.75	12.15	1.29	36±7	3.1±0.4
240 nm	4.095(6)	4.095(6)	4.090(6)	1.000(0)	68.59(2)	8.44	13.24	2.46	28±9	1.7±0.5

We observed a small (100)-orientation tendency with decreasing the film thickness, while thicker films show a random orientation behavior [138]. As discussed in literature the mechanisms responsible for the preferred orientation in PLZT films prepared by different methods can be related to the bottom electrode. The (111)-orientation PLZT films was found to be controlled by an ultra-thin TiO_2 layer prior the film deposition. The presence of the titanium oxide seeding layer clearly promoted the crystallization of the (111)-oriented PLZT perovskite [210]. Other seeding layers like $(Ti_2)_x(PbO)_x$ were also used to promote a preferred orientation in thin films due to its lower surface energies [211, 212]. Another explanation for the preferred orientation phenomena is probably due to the lattice matching between the film and the substrate or to the effect of a metastable Pt_3Pb phase in the early stage of the film crystallization [213]. There was no clear indication of the lattice match between film and substrate in our PLZT thin films. However, the small increasing of tetragonality of the perovskite phase for the thinner film could be an indicative of a PbO layer that leads to an enhanced (100)-orientation for thinner films and tends to decrease for thicker films.

The microstrain and the crystallite showed to increase almost linearly with film thickness. The thickness dependence of the non-uniform strain observed in our films may be due to the decrease in lattice defects for thinner films [214, 215, 142]. The measured strain in X-ray diffraction experiments is an elastic strain and, as the presence of structural defects produces a plastic strain, a relaxation of the accumulated elastic strain is observed in thinner films. The increasing in lattice deformation with thickness is probably caused by the gradual incorporation of La^{2+} in the structure during the growing process [210]. Also is worthy to notice that this thickness dependence of microstrain can be a direct consequence of the polymeric chemical method used in this investigation to prepare the films. The reduction of a lattice

deformation as we decrease the thickness results in a reduced interplanar spacing, minimizing the stacking faults as a consequence of the minimum surface energy.

The crystallite size was also observed to increase with film thickness. The values obtained for our PLZT films are in close agreement with the reported values to films of PZT [216]. The observed thickness dependence of the crystallite size is probably caused by different degrees of heat-treatment of the films. Thicker films were obtained by more repetitions of resin depositions and heat process (pyrolysis) at 300 ºC, which means that thicker films were subject to heat-treatment for a long period, although the temperature was below that of the considerable crystallization process of the PLZT thin films [217].

4.2.1. Microstructure and Morphologic Analysis of PLZT thin film

Figure 26 below depict top view SEM micrographs of PLZT thin films thermally treated at 400, 500, 600, and 700 ºC for 1 h. The SEM images show the surface and illustrate the differing microstructure evolution of the films. A porous microstructure with a certain degree of order and periodicity was observed to depend on the thermal treatment used in these films.

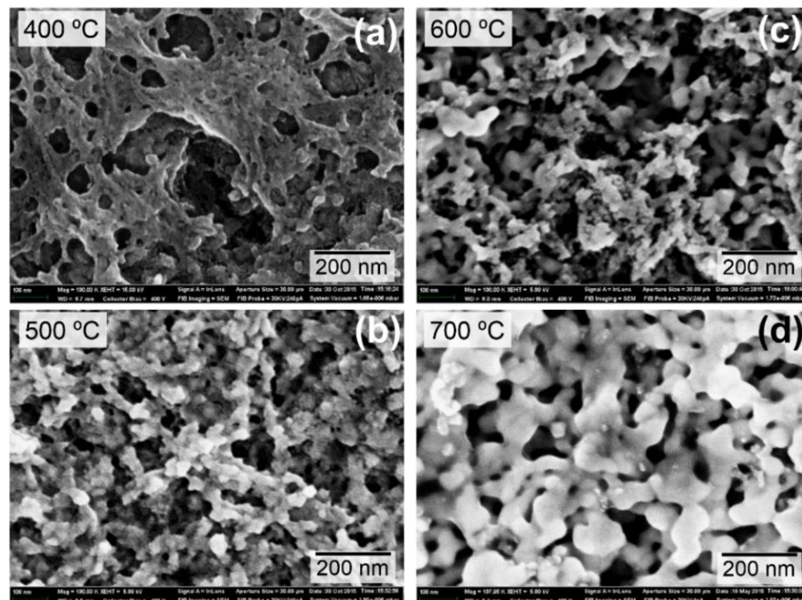

Figure 26: SEM micrographs exhibiting the typical morphology of mesoporous PLZT thin films after thermal treatment at 400, 500, 600 and 700 ºC, respectively. As the temperature of the thermal treatment increases, the porosity order is increased, pores become interconnected and dense areas increase as well. A well-defined grain pattern with annealing temperature characterizes the crystallized PLZT thin film.

Figure 26b presents a SEM micrograph of the film treated at 400 ºC and we observe no crystallized grain with the formation of pores at nanometre size. As we increase the crystallization temperature, there is a formation of grains that are interconnected and, consequently, the degree of order is increased. At 700 ºC, the morphology of the film surface

illustrates a full crystallization of the grains and a higher degree of order of the porosity was verified, when compared to the films thermally treated with lower temperatures.

Cage-like uniform mesopores were observed in the entire area of the film and connected each other. The SEM micrograph at 700 ºC of PLZT film exhibited the presence of uniformly sized mesopores (average ~150 nm). The mesopores features observed in our film were rather similar to mesoporous gold (Au) films reported by Li *et al* (2015) prepared by electrochemical synthesis [218]. The pore ordering results from the self-assembly of micelles of the amphiphilic block copolymer, followed by condensation of the inorganics around an ordered arrangement of micelles. During the thermal decomposition of the block-copolymer, voids are created and this takes place at 300 ºC (pyrolysis temperature) [219, 220].

As the temperature of the heat treatment increases, the microstructure of the mesoporous films varies, from a disorganized pore arrangement to an interconnected porosity. The films heat-treated at temperatures lower than 700 ºC were partially or entirely amorphous. Only at 700 ºC, dense films crystallize and a well-defined grain pattern can be observed. The growth of the grains is evident in films annealed at 700 ºC. XRD patterns of PLZT thin films as we presented in the previous chapter an analyse of the crystallization process at various temperatures.

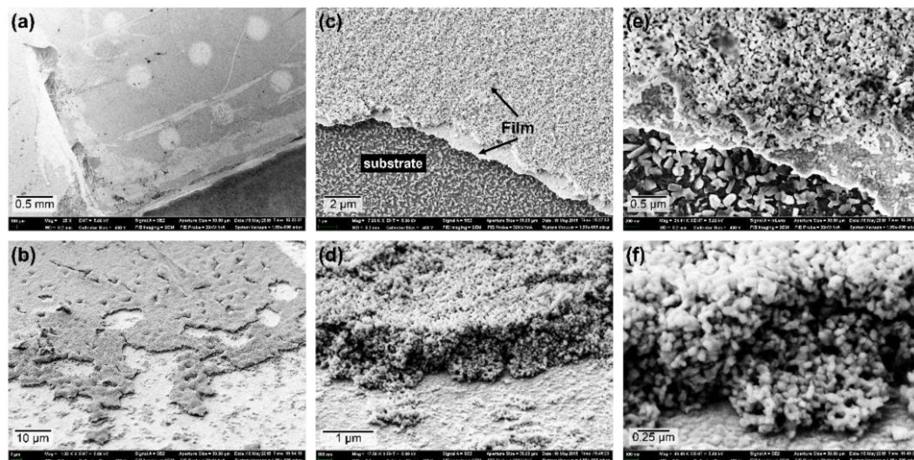

Figure 27: SEM images of the PLZT thin film in (a) a wide surface and (b) an area displaying the material and the bottom electrode (Pt) in which we can see several cracks over the film surface. In (c) is possible to observe another area illustrating the boundary between the bottom electrode and two different morphology layers of the film. In (d) an approached image of the thin film shows the remaining grains that are stuck on the substrate. SEM top view of PLZT revealing the interfaces between some individual crystallization steps is shown in (e) and a SEM side view of the crystallized grains through the film can be seen in (f).

Figure 27 shows SEM micrographs of particular areas in order to verify some characteristics of the interfaces between the PLZT thin film and substrate. Figure 27a presents a wide area of the film surface. Clearly, we can see a contrast between the film and the circular gold top electrodes (Au). Several attempts to perform dielectric measurements on these top

electrodes have led to many scratches on the surface, suggesting that the material possesses soft-like features. Before the application of any mechanical polishing on surface film to obtain cross-sectional investigations, SEM image of an area displaying the microstructures of the interfaces between film and bottom electrodes were performed and it can be seen in Figure 27b. An inhomogeneous pattern of cracks is observed over the film surface, indicating the possible existence of a strain resulted from thermal treatment. Another important point to notice is the difference observed in porosity between one layer and another in our PLZT thin film.

The very first layer deposited during the thin film process seems to be rather denser that the last layers, as we can see in Figure 27c. Probably, this effect can be due to the additional thermal treatment during the pyrolysis process, resulting in the increasing of the pore connectivity and simultaneously the relative area of dense zones. These dense zones correspond to film densification promoted by the heat treatment [219]. The film thicknesses used in this work are 240, 350, 430, and 540 nm. As we have already described, the thin film thicknesses was achieved by incremental depositions of the polymeric resin. To obtain the desired thickness, we have deposited 2, 4, 6, and 8 layers, respectively. Therefore, it is important to notice that the film thickness does not increase in proportion to the number of deposited layers. It is possible that during the first stages of thermal treatment, the pores of the first deposited layers can be partly filled with a subsequently deposited layer, resulting in a more densification of layers that are near the substrate. Figure 27e also shows some crystallization layers of the thin film with a slightly different degree of order of the porosity as well as the degree of densification. The porosity is increased as the layers experience less heat treatment during the process. Figure 27d and Figure 27f illustrate SEM side views of a non-flat cross-section of the thin film in different places. Despite the morphology of grains appear quite similar, the pore connectivity seems to be slightly different through the film.

SEM observation of a specimen cross section can provide important information about the samples. In many cases, surface observation alone can not compare to the cross-sectional image of granular materials, layered materials, fibrous materials, and metallic coatings, etc. In order to obtain a cross-sectional analysis we made an attempt to perform a cross-section using mechanical means, like conventional mechanical polishing methods. The sample was embedded in a holder and polished to achieve a flat cross section. Regardless the mechanical techniques, our PLZT film has presented as a soft-like material and it was not possible to achieve a flat cross section by mechanical polishing [221].

Instead of using mechanical techniques, it was possible to perform a flat cross section in our film using a Focused Ion Beam (FIB) System with high precision. However, the size of

the resulting cross section is rather limited and possibly be damaged by heavy atoms [221]. A precision argon (Ar) ion beam cross section polisher was used to prepare truly representative cross sections of our samples free of artifacts and distortions.

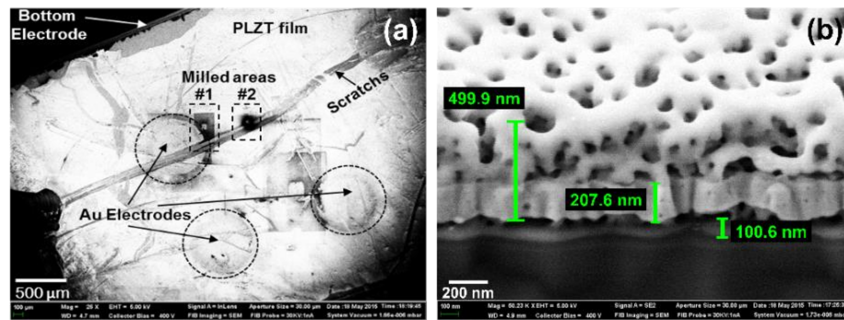

Figure 28: (a) SEM image of the PLZT thin film surface pointing the top electrodes and the (inset) irradiated area used to mill the sample by FIB method. SEM micrograph revealing the morphology of the cross-section of the film is shown in (b).

Figure 28a presents a region in which has been irradiated with a broad argon ion beam with an accelerating voltage of 5 kV. During milling, the specimen stage was automatically rotated ± 52º related to the Ar beam in order to prevent beam striations and ensure uniform etching. Figure 28b present different magnifications of the flat cross section in our film. In these images is possible to observe the morphology on the surface and on the cross section, especially at the interface between the film and the substrate. According to the SEM images, the denser part of the film has about 200 nm in thickness while the film has shown in the cross section a thickness of 500 nm approximately.

4.2.2. Ferroelectric Properties of PLZT thin films

The macroscopic ferroelectric properties of PLZT thin films were investigated as a function of frequency and temperature, as can be seen in Figure 29a and Figure 29b, respectively. Figure 29a shows the P-E hysteresis loops at 183 K in the frequency range from 50 Hz to 5 kHz, while the hysteresis loops at 1 kHz at temperatures in the range 183-293 K are shown in Figure 29b. Clearly, we can observe a small change in the saturation polarization of both temperature and frequency dependence. Small changes in remnant polarization and coercivity were also observed.

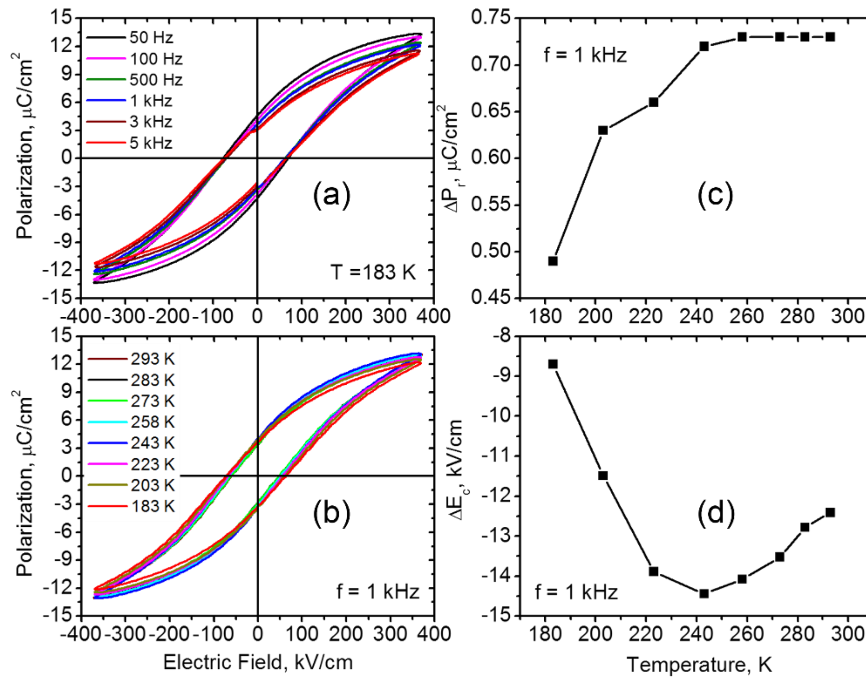

Figure 29: P-E hysteresis loops in PLZT thin film: (a) at 183 K at a frequency range from 50 Hz to 5 kHz and (b) at 1 kHz frequency at temperatures in the range 183-293 K. Temperature dependence of the differences (c) $\Delta P_r = P_r^+ - P_r^-$ and (d) $\Delta E_c = E_r^+ - E_r^-$ at 1 kHz frequency. Lines in (c) and (d) are drawn as a guide to the eye.

To investigate the temperature dependence of the P-E hysteresis loops, the differences in the remnant polarization $\Delta P_r = P_r^+ - P_r^-$ and coercive field $\Delta E_c = E_c^+ - E_c^-$ were plotted in Figure 29c and Figure 29d as a function of temperature, respectively. We observe that both ΔP_r and ΔE_c decrease with temperature decreasing indicating a more symmetrical hysteresis loops at lower temperatures. This effect can be due to the coexistence of both relaxor glass-like and FE dominated regions at low temperatures. At low temperatures slow conversion from the glassy RE state to the microdomain FE state takes place under cooling [54], decreasing the asymmetries observed in the P-E hysteresis loops. Therefore, the decrease in both ΔP_r and ΔE_c

tends to vanish at low temperatures, suggesting an increasing in the long-range FE order and minimizing the effect of built-in electric fields on the dynamic of PNRs in the RE phase.

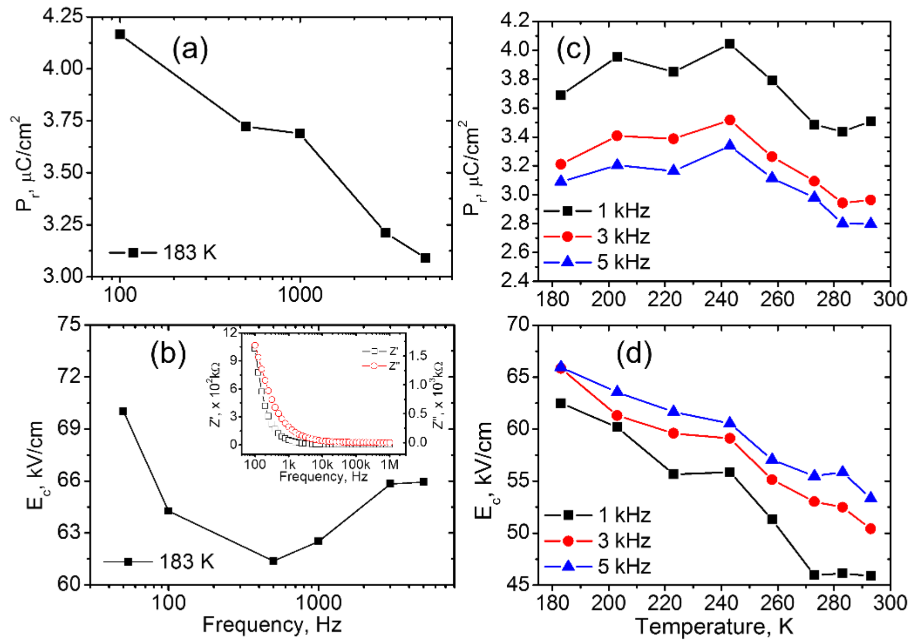

Figure 30: Frequency dependence of the (a) remnant polarization at 273, 223, and 183 K and (b) coercive field at 273, 223 and 183 K of temperature. Temperature dependence of the (c) remnant polarization and (d) coercive field at 1, 3 and 5 kHz frequencies. The real and imaginary impedances as a function of the frequency is shown as inset in (b). (Lines are drawn as a guide to the eye).

Figure 30 shows the frequency and temperature dependence of the remnant polarization and coercive field. The remnant polarization decreases with frequency within the frequency range while the coercive field decreases at first, and then increase after reaching the minimum value at 500 Hz. The coercive field, spontaneous and remnant polarization, and shape of the loops may be affected by many factors including the thickness of the sample, the presence of charged defects, mechanical stresses, preparation conditions, and thermal treatment [222]. The shape of the hysteresis loops can also experience changes depending on the conditions the system is undergoing. The most relevant shape modifications of hysteresis loops are represented by pinched loops (constricted P-E loops in the region $E \approx 0$, remnant polarization approaching to zero), asymmetric loops (imprint effect) and polarization gaps (relaxation of the remnant polarization at $E = 0$), which have been found in different ferroelectric systems (polycrystalline or single crystal) [223]. As we discussed above, it is generally accepted that these characteristics can be caused by the development of an internal bias field whose magnitude and the distribution depend on both composition/microstructure and on the thermal /electrical history of the system [223].

The increase of the frequency of external field entails a decrease of the remnant polarization, as we can observe in Figure 30a. This effect can be explained in terms of domain motion. Most of the domain directions are reversible by the external electric field but some domains cannot follow it during the switching process. We have noticed experimentally that the coercitivity also increases for frequencies higher than 500 Hz, being necessary an application of higher voltages in order to cause a polarization switching in such domains. The pinning of domain walls is one of the possible mechanisms responsible for the remnant polarization reduction since pinned domains cannot be switched. This pinning effect is due to the entrapment of space charges at the electrode or domain interfaces, typically causing ferroelectric fatigue. Moreover, oxygen defects can contribute to the ferroelectric fatigue and cause an increasing in the domain pinning, acting as real trapping sites for electrons injected into the ferroelectric film [224].

Since it was reported by Genenko *et al.* [225] that PLZT ceramics seem to be fatigue-free for frequencies in the kHz regime, it is not clear if the fatigue effect is the main reason for both the decrease of the remnant polarization and its concurrent increase in coercivity. Other possible reason consists in assuming a difference in domain wall switching dynamics arising from a difference in domain structure. It is possible that the nucleation and growth process in two film orientations is different [224]. If the degree of 180 º and non-180º switching is different in the two cases, or if the polarization vector in (001)-oriented film rotates somehow first to switching, then the conditions required to develop non-switching "blocked" regions may differ for the two orientations [226].

For the reversal of the polarization, the coercive electric field necessary to provoke a switching follows a power law to explain its dependence on frequency, given by

$$E_c(f) \propto Bf^{d/\alpha} \tag{39}$$

where d is the dimensionality of domains and α is a frequency coefficient that is temperature dependent [30, 227, 228]. Then, the frequency behavior of the coercive field can be interpreted in terms of the increase of resistance of the domain wall motion during switching [62]. The behavior of the coercive field with frequency has been experimentally observed in PZT systems in 90º domain wall relaxation studies [229]. Though the domain wall motion can be used to explain the increasing of the coercive field with increasing frequency, the observed increasing for lower frequencies (below 500 Hz) is not fully understood. For thin films, Dawber *et al.* [230] have shown the importance of incomplete charge compensation at the ferroelectric electrode interface and the resulting depolarization fields, leading to the distinction between the measured and the true coercive fields. It was observed that rapid increase of the impedance

takes place at 500 Hz (inset Figure 30b), suggesting a relationship with the increasing resistance of the electrical current with coercivity at lower frequencies. Further investigations are needed to better understand the frequency dependence of the coercive field in our films, despite the results indicate an influence of defects and motion of domain walls [231].

Figure 30c and Figure 30d show the remnant polarization and coercive field as a function of temperature at three different frequencies. As the PLZT thin film is under cooling, the remnant polarization initially increases and then decreases after reaching a maximum at 243 K regardless the frequency. The coercive field, on the other hand, decreases almost linearly with temperature for all frequencies. These behaviors suggest the occurrence of a re-entrant dipole glass or an activated electric field effect in the studied PLZT thin film, which is characterized by the loss of ability to field induce polar ordering to large random dipolar interaction at a low enough temperatures [232].

The existence of an equilibrium phase transition into a low-temperature glassy phase is one of the most interesting characteristics in relaxors [98]. The nonergodic relaxor (NR) state existing below freezing temperature can be irreversibly transformed into a ferroelectric (FE) state if a sufficient external field is applied in canonical relaxors. The similarity between relaxors and dipolar glass materials can be considered only for the nonergodicity feature, but not for a transition into FE state. Nevertheless, using an analogy with spin-glass theory, the basic features of relaxors could be explained [20] if considered that the transition from weak-FE state to NE dipole-glass state is a possible explanation for the re-entrant dipole-glass behavior observed in the $_{0.95}BaTiO_3–_{0.05}BiScO_3$ [233], $Ba_{0.9}Bi_{0.067}(Ti_{1-x}Zr_x)O_3$ solid solution [21], and $_{0.99}BaTiO_3–_{0.01}AgNbO_3$ [234] systems. The re-entrant relaxor behavior observed in these ferroelectric systems is called analogously to re-entrant magnetic spin glass systems [235].

The re-entrant phenomena are featured by a transition from a more ordered state first developed at higher temperatures before going back to a more disordered state at low temperatures [171]. The remnant polarization first increases as the temperature is lowered, but drops down on further cooling essentially vanishing at low temperature [235]. In Figure 30c, the PLZT film presents firstly an increasing of the remnant polarization and then decreases after the temperature drop more than 240 K and the maximum observed suggests a re-entrant phenomenon in our films. The re-entrant behavior found in $(1-x)BaTiO_3–xBiScO_3$ ($0.10 < x < 0.45$) system is assumed to be due to a competitive dipole interaction between local ferroelectric and antiferroelectric (AFE) order and/or local stress [235]. Local PFM investigations have shown that disordered states with the presence of PNRs grow within normally ordered

ferroelectric phase, suggesting that polar conglomerates develop from a ferroelectric state and re-enter the frozen disordered phase, instead of emerging directly from a paraelectric state as in most other RE ferroelectrics [233].

Re-entrant-like behaviour has also been reported by Huang *et al.* [236] in $(Sr_xBa_{1-x})Nb_2O_6$ (x = 0.25, 0.5, 0.75) unfilled tungsten bronze ceramics. They suggested that the decline of switchable polarization at low temperature in the SBN system is mainly due to the increase of the coercive electric field rather than the decrease of the long-range-order interaction of structural dipoles on cooling [236]. In terms of kinetics, one knows that the switching of domains in ferroelectric materials by an applied field is believed to occur by the formation of new domain nuclei with the favored orientation of polarization, which subsequently expand and grow at the expense of the existing domains [237, 238, 239, 240, 241]. At low temperature, the ferroelectric domains are hindered to be switched because of the low nucleation rate, given by the Arrhenius type expression $\Gamma = \upsilon \exp\left(-\Delta G / kT\right)$, where ΔG is the Gibbs free energy, T is the temperature, υ is the frequency related to the correlated fluctuations of the group of atoms involved in the formation of nucleus. In this way, a higher electric field is necessary to switch the ferroelectric domains, i.e., increasing the coercivity [240]. Therefore, the low-temperature linear response detected in our PLZT thin film may be essentially different from the re-entrant relaxor behavior.

Despite the PLZT system has been intensively investigated in the past due scientific and technology reasons, some interesting questions still open to debate. Among a few reports on the field dependence of switchable polarization on cooling, the effect of temperature on remnant polarization for PLZT compositions exhibits a gradual increase as the temperature decreases and no abrupt change of the dielectric permittivity. The effect of temperature on induced phase transition in PLZT ceramics with 9/65/35 composition has been studied by Bobnar *et al.* [242]. They concluded that cooling the system with a bias field above E_c an ER to a FE phase transition was induced while by cooling below E_c the system undergoes the transition from the ER to NR state at a freezing temperature T_f (at which the divergence of the longest relaxation time effectively breaks ergodicity). The ER-NR and ER-FE transition lines can be well described by a spherical random bond-random field model of RE ferroelectrics [98]. In spite of the temperature dependence of the remnant polarization observed in the present work and the above considerations, it is not possible to affirm that it is certainly a re-entrant phenomenon. Actually, all films and bulk materials can become normal ferroelectric with a high coercive field at low temperatures [236].

We should be careful when we identify the re-entrant relaxor behavior only by the character of a decrease of polarization at low temperature. Further investigations are needed to clarify the temperature dependence of remnant polarization under different electric fields. Accordingly, only after that is possible to infer about the mechanisms and unravel the true origin of this phenomenon observed in this work.

4.2.3. Effects of thickness on structural, grain size and local piezoelectric properties of self-polarized PLZT thin films

In this chapter, we are going to discuss the effects of thickness and grain size on structural properties, local piezoelectric properties, and correlation length of polycrystalline PLZT thin films prepared by chemical route. The structural properties have already presented previously as a function of thickness as well as temperature used in thermal annealing. The PFM technique has been used to investigate the piezoelectric properties at the nanoscale. This section aims to provide a qualitative relationship between grain size and size of ferroelectric nanodomains in our PLZT thin films.

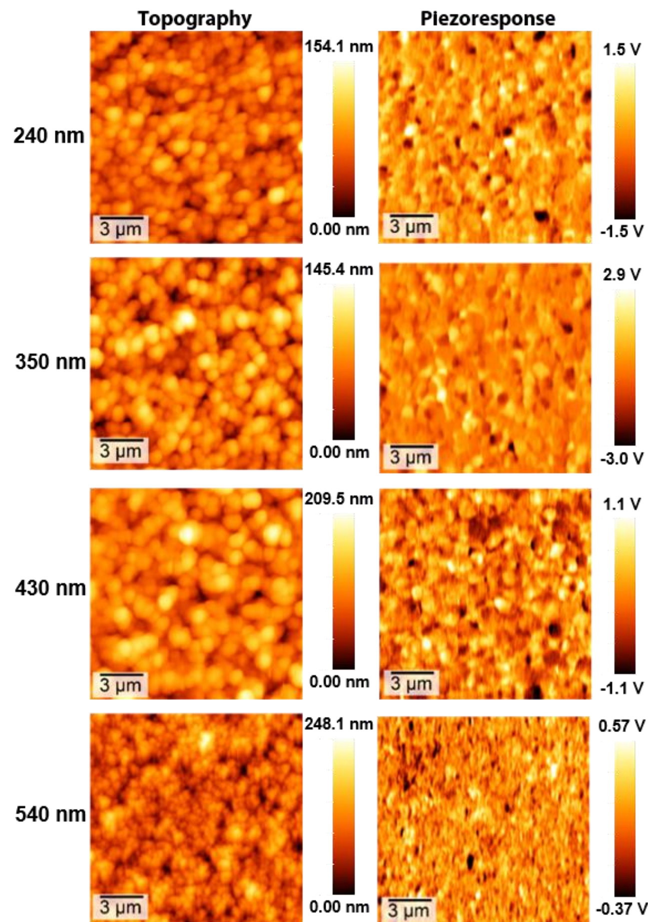

Figure 31: Topography and VPFM piezoresponse images of PLZT thin films for the thicknesses 240, 350, 430 and 540 nm, respectively. The scan size of the images is 15×15 μm^2.

The topography and vertical piezoresponse images of PLZT thin films at different thickness are shown in Figure 31. As we can see, the topography is very similar to the studied films, except for the thicker one. The thicker film (540 nm) exhibited smaller grains as observed in Figure 31. Again, here the bright and dark areas in out-of-plain images are related to upward and downward polarization vectors, respectively, while intermediate contrasts refer to the weak piezoresponse signal. Figure 31 shows that the piezoresponse in these films is quite homogeneous.

The grain size was obtained from topography images, showed in Figure 31. The average grain sizes were plotted as a function of film thickness in Figure 32a. We can observe visually from topography images a clear difference in grain sizes between films with different thicknesses. The film with 350 nm in thickness has exhibited larger grain size (about 738 nm) while the thicker one (540 nm in thickness) has shown smaller grain sizes (about 438 nm). To obtain the grain size information as a function of thickness, it has been considered that the grains were all rounded and spherical, even though some elongated grains has been observed. Triangular-shaped grains were also reported in PLZT thin films with 10%-La^{3+} content grown on platinized silicon substrates by RF magnetron sputtering technique and this effect was associated with the preferential (111)-orientation in these films [5, 210].

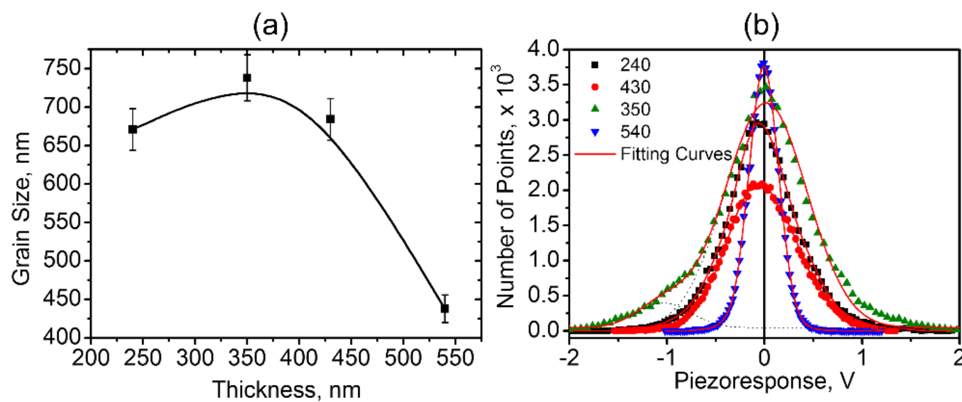

Figure 32: (a) Thickness dependence of average grain size of studied PLZT thin films. (b) Piezoelectric histogram distribution of PLZT thin films at different thicknesses. The line in (a) is drawn as a guide to the eye while lines in (b) refer to fit curves.

The grain shape is closely related to growth process of the thin films. During the process, two growing islands may eventually meet and when they are close enough to interact each other, they will begin restructuring to minimize the energy in the system. The atoms diffuse mainly along the grain surface forming a grain boundary, thereby trading surface energy in order to minimize their chemical potentials. The surface diffusion proceeds to change the grain shape

until new grain reaches its equilibrium shape [243]. Excluding the texture effects on the morphology of our films, (these should be minimal for the top layer), a large amount per deposition of material to be crystallized may lead to spherical grains observed in the present work.

The piezoresponse histograms, or we can also call piezohistograms, were acquired from piezoelectric vertical images of PLZT thin films and these are shown in Figure 32b for different thicknesses. The importance of the statistical analysis of piezoresponse was already described when discussed the piezoelectric properties at nanoscale of SBN thin films. The piezohistograms are statistical distributions of the piezoelectric signal related to the domain setup in a ferroelectric material [191]. In our case, the piezoelectric properties were obtained in out-of-plane polarization direction, resulted from the vertical displacement of the tip due to the effective piezoelectric coefficient [244, 28]. The observed peaks in these distributions curves are associated with the most probable domain formation while the peak half-width is a measure of a number of domain states.

These piezohistograms distributions in Figure 32b suggest single peaks for films with 240, 350, 430, and 540 nm. However, the distribution of the piezoresponse for the film with 350 nm in thickness clearly presents a peak close to 0 V and a "shoulder" around -1 V (Figure 32b the dot lines are associated with the peak deconvolution in two Gaussian distributions). Only one peak for films with 240, 430 and 540 nm in thickness indicates the predominance of unimodal domains, and, for this reason, one Gaussian function has been used to fit the respective piezohistograms. However, the bimodal distribution of the film with 350 nm thick suggests a predominance of domains centered around 0 V with another active piezoregion, or "dynamic" polar nanoregions [245, 246], shifted to negative voltages (~1.0 V). Then, two Gaussian functions were used to fit this piezohistogram. Despite two Gaussians used in our analysis, we considered the width of the main curve around 0 V for the film with 350 nm in thickness, since the secondary peak around – 1 V is too small, though the presence of a secondary peak affects the linewidth of the main peak.

Important information can be obtained from curves fitting in Figure 32b. The peak half-width of piezohistograms is an important parameter to be considered to infer about the polarization directions evolution. In polycrystalline thin films randomly oriented, the half-width broadening suggests the coexistence of various polarization directions [149]. The thickness dependence of the peak half-widths in piezohistograms from Figure 32b is shown in Figure 33. Looking more closely at the curve shapes in Figure 32a and Figure 33 we observe that both curves show essentially the same behavior with film thickness. A maximum value of the peak

half-width is observed at the film with 350 nm in thickness as well as a minimum at the thicker film (540 nm thick). These results suggest an intrinsic relationship between the coexisting polarization directions and the grain size. In order words, the coexisting polarization directions increase with increasing grain size in the studied films.

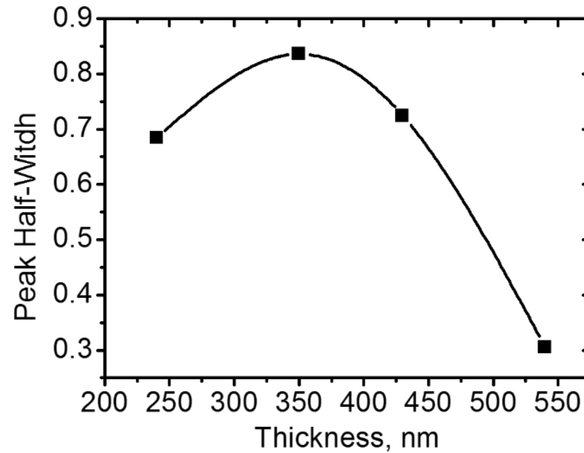

Figure 33: Thickness dependence of peak half-width of the piezohistograms. Lines in both curves are drawn as a guide to the eye.

Other important information that it is worth mentioning is the thickness dependence of crystallite size in our PLZT thin films (Table 3). As the domain orientation can be observed in different directions inside the grains, evidently the domain orientation of grains depends on the internal crystalline structure. Doubtless, larger grain sizes may host a larger number of smaller crystallites, resulting in a more complex internal crystalline structure for these films.

The asymmetries observed in the piezohistograms of Figure 32b are other points that have to be considered. The d_{33} peaks shift slightly towards negative voltages for films with 240, 350, and 430 nm in thickness, but the piezohistogram of the thicker film (540 nm thick) is almost symmetrical around 0 V (d_{33} peak ~ 5.7×10^{-3}). About these observed asymmetries, we need to punctuate some possible reasons. Firstly, we have to consider the instrumental effects associated with tip geometry, to electrostatic effects or to piezoelectric interactions due to tip-sample interactions on the PFM signal. Even though we have used a metallic spherical tip in our measurements, it was reported that the magnitude of the piezoelectric coefficient is independent of the tip radius, and the PFM profile width is linearly proportional to the tip radius [247]. Another effect that has to be considered is the contribution associated with the capacitive force or Maxwell force. The system comprising the conducting tip in a contact with the dielectric surface represents a capacitor. Therefore, an external voltage applied between the tip and the bottom electrode results in an additional force, given by

$$F_{cap} = \frac{dW_{cap}}{dz} = \frac{1}{2}V^2 \frac{dC}{dz} \tag{40}$$

where $W_{cap} = V^2C/2$ is the energy stored in the capacitor C and z are the vertical distance [47]. Thereby, the capacitive contribution of the cantilever to vertical displacement measured by the PFM has been demonstrated to be $\propto V_{ac}/k$ and a piezoelectric contribution $\propto d_{33} V_{ac}$, where k is the spring constant of the cantilever [150]. As we have used stiff cantilevers in our studies, the capacitive contribution is expected to me minimal, prevailing the piezoelectric part in the PFM signal without injection effect due to the potential barrier between the tip and surface of the film. Thus, we expect no direct influence of bottom electrode on the electrostatic effects, as well no charge injection effect due to the potential barrier between the tip and film surface. Based on these assumptions, we excluded tip geometry or electrostatic effects as mechanisms responsible for the asymmetries in the piezohistograms.

A possible cause for the small asymmetries observed on the distribution of the piezosignal, excluding instrumental effects, is the imprint effect [203]. The imprint phenomenon, referred sometimes as a self-polarization effect, is often observed in ferroelectric thin films. Asymmetries of piezoelectric coefficient versus DC electric field loops are related to the self-polarization [248]. These asymmetries on the hysteresis loops are due to the existence of a built-in electric field. Considering the distribution of the piezoelectric response signal, self-polarization can be evaluated by the β factor according to the equation (36). This factor reflects the difference between all positive and all negative domain states divided by all domains states in the studied range. The behavior of the self-polarization β factor as a function of thickness to infer the origin of asymmetries in the histograms is illustrated in Figure 34.

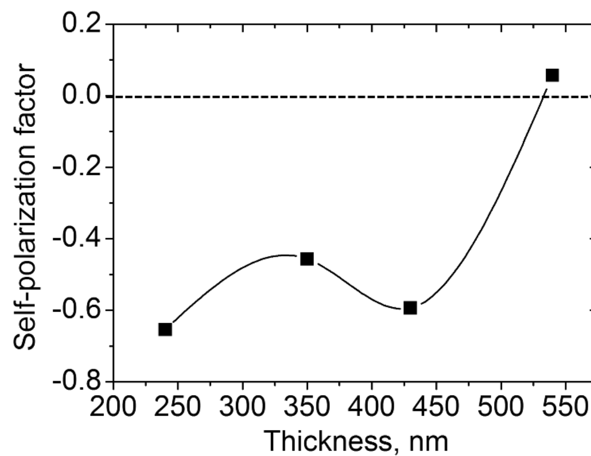

Figure 34: Thickness dependence of self-polarization factor (see text) of PLZT thin films. Lines in both curves are drawn as a guide to the eye.

The self-polarization factors in Figure 34 slightly shifting to the negative values for thinner films suggest a predominance of "negative" domains over the oppositely oriented "positive" domains, indicating a polarization directed towards the bulk of the film. For the thicker film, the self-polarization factor is almost zero. The weak self-polarization observed for the film with 540 nm in thickness suggests a predominance of "positive" domains, i.e., polarization directed towards the free film surface. Asymmetries observed in slim macroscopic hysteresis loops of the PLZT film with 540 nm in thickness (shown in Figure 29) reveal that the difference between positive and negative remnant polarization is $\Delta P_r = P_r^+ - P_r^- \approx 0.7\ \mu\mathrm{C/cm^2}$. These results, both for local and macroscopic scale, indicate that the net remnant polarization (ΔP_r) is positive. Despite the different magnitudes, the positive net remnant polarization at macroscale agrees with the positive local self-polarization observed in Figure 34 for the thicker film. Although macroscale P-E hysteresis loops were not acquired for thinner films, the self-polarization factor shifting to negative values in Figure 32b for thinner films (larger grain sizes) indicates the existence of a built-in electric field towards the bottom film-substrate interface. However, for thicker film (smaller grain sizes) a small built-in electric field towards free surface of the film is also possible.

The origin of the self-polarization in FE thin films has been discussed in terms of different mechanisms. Among the mechanisms, we can mention the Schottky barrier, acting as a built-in field poling the interfacial region of a FE film [189]. When the top and bottom electrodes of a metal/ferroelectric/metal configuration are made of different materials, trapped charges appear near the bottom ferroelectric-electrode interface leading to a built-in electric field responsible for self-polarization. In addition, the *n*- or *p*-type conduction by oxygen and lead vacancies (or other impurities) are complex defects in Pb-based thin films that may be also responsible for the localized built-in electric field in the FE film giving rising to the imprint effect [249]. Such defect appears in these materials due to several factors such as PbO loss and oxygen pressure during the synthesis or donor/acceptor impurities introduced in the perovskite ABO_3 structure [9]. The stress induced by film/electrode lattice mismatch or clamping [203] is another mechanism responsible for the self-polarization. During the formation temperature of the FE phase, due to different thermal expansion coefficients between film and substrate, may originate a compressive or tensile stress on cooling after the film crystallization, producing a self-polarization state [249].

Space-charge field is another point to consider as a possible origin of the built-in electric field in our films. It was observed in experiments with PLZT ceramics that the space-charge

field increases with decreasing grain size and increasing porosity [102]. Here, the self-polarization factor shifting to negative values for thinner films suggest the built-in electric field increases with increasing grain size. Besides, even though porosity is relatively higher in thin films prepared by the polymeric chemical method used in the present work (compared to thin films prepared by physical methods such as RF-sputtering or laser ablation) it is practically improbable that space charges is the dominant mechanism responsible for the built-in electric field in our studied PLZT thin films. Despite different models are used to explain the mechanisms of the built-in electric field in FE films [69], the nature of this effect and naturally, depends on each particular system studied.

The randomly oriented PLZT thin film investigated here and the expected low thermal expansion coefficient between the film and the substrate, we may exclude strain gradients along the film depth and compressive/tensile stress as mechanisms of self-polarization, though mechanical stress can result from various phenomena, such as porosity can this effect in the films. Therefore, further investigations about the influence of porosity on physical properties are extremely important to corroborate this explanation.

Although recent studies on the thickness dependence of self-polarization in PZT thin films [250] prepared by the same chemical method used in this work have excluded Schottky barriers and mechanical coupling near the film-substrate interface and assumed that complex defects are probable mechanisms responsible by self-polarization [251], the case observed here for the PLZT thin films is different. In other words, while the self-polarization occurs in the bulk, our results suggest the Schottky barriers closed to the bottom film-substrate interface seems to be the dominant mechanism for the self-polarization in our films of PLZT. The increase in self-polarization with decreasing film thickness first suggests that the alignment of ferroelectric domains may occur near the film-electrode interface. In this case, Schottky barriers near the film-substrate are likely responsible for the built-in electric field in the studied PLZT films. However, other experiments are needed to clarify the mechanisms of self-polarization in PLZT films.

A quantitative analysis of the nanodomain structure of the PLZT films was investigated. The existence of a correlated polarization could be easily verified by an autocorrelation analysis [252]. Autocorrelation images were obtained by applying the transformation

$$C(r_1, r_2) = \sum_{x,y} D(x, y) D(x + r_1, y + r_2), \quad (41)$$

on the piezoresponse images. $D(x, y)$ is the value of the piezoresponse signal at a point in the image and $D(x + r_1, y + r_2)$ is the PFM phase signal at a point translated by (r_1, r_2) from the original reference point. The shape of the autocorrelation function provides information about the symmetry and regularity of the polarization distribution. The correlation function technique has been used firstly for topographic analysis [253]. The value of $D(x, y)$ taken from the piezoresponse image is proportional to the local polarization value. So, its autocorrelation function $C(r_1, r_2)$ is equivalent to a “polarization-polarization” correlation function [56].

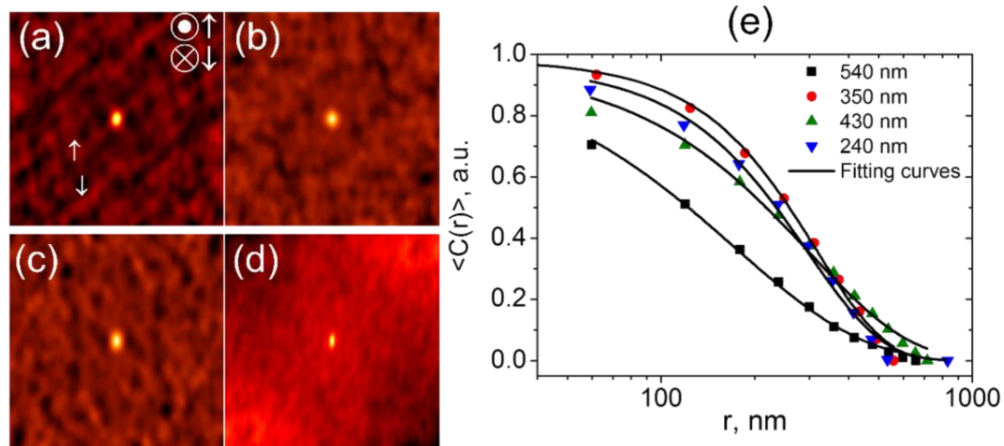

Figure 35: Autocorrelation images (scan area 15×15 μm^2) of PLZT 9/65/35 thin films for film (*a*) with 240 nm, (b) 350 nm, (c) 430 nm, and (d) 540 nm in thickness. (e) The autocorrelation function $<C(r)>$ average overall in-plane directions for PLZT thin films with 240, 350, 430, and 540 nm in thickness, respectively.

The 2D images of $C(r)$ for different film thickness are shown in Figure 35(a-d). The bright contrast represents areas with correlated polarization, and dark contrasts correspond to negative values of the correlation. In the sense of polarization-polarization correlation analysis, this means that bright contrast implies a probability to find a parallel polarization direction, while dark contrasts indicate the probability to find an antiparallel polarization of the FE domain over all out-of-plane directions.

Clear anisotropy could be related to the existence of the preferable directions of alternating regions with opposite contrast. These directions are thought to be closely associated with specific crystallographic axes of the perovskite structure in PLZT films. However, since the investigated PLZT thin films in the present work were prepared randomly oriented (i.e. with no preferential orientation) it is difficult to identify the crystallographic axes in the autocorrelation function analysis.

As we can observe in Figure 35a and Figure 35b, the autocorrelation images referred to thinner (240 nm) and thicker (540 nm) PLZT film show a strong difference. In the thinner film, there is clearly a probability of finding an antiparallel domain configuration periodically in a

short-range, while in the thicker film (Figure 35b) overall in-plane directions the probability to find a negative correlation is very small in the studied range. In particular, the width of the central peak in the two-dimensional $C(r_1, r_2)$ map is a measure of the polarization correlation radius and its width can be used as a measure of the mean size of piezoactive regions [202]. In other words, autocorrelation analysis of the PFM data provided quantitative insight into the polarization distribution and nanodomain structure. This type of analysis was used to estimate the size of the PNRs [182]. The autocorrelation function can be represented as a sum of two contributions, as follows

$$\langle C(r)\rangle = \sigma^2 \exp\left[-\left(\frac{r}{\langle\xi\rangle}\right)^{2h}\right] + (1-\sigma^2)\exp\left[-\frac{r}{r_c}\right]\cos\left(\frac{\pi r}{a}\right). \tag{42}$$

The first and second terms correspond, respectively, to short- and long-range correlation. Only a short-range correlation length term was taken into account for our thin films with uniform morphology, which was useful for the estimation of the characteristic parameters of the nanodomains. In this case, to obtain a measure of the short-range polar order, autocorrelation function was average overall in-plane directions and then approached by the first term of the Equation (42), that is the function represented by

$$\langle C(r)\rangle = \sigma^2 \exp\left[-\left(\frac{r}{\langle\xi\rangle}\right)^{2h}\right]. \tag{43}$$

Here, the variable r is the distance from the central peak, $<\xi>$ is the average correlation radius, σ is a pre-exponential factor, and the h ($0 \leq h \leq 1$) is a measure of the “roughness” of the polarization interface [182]. Based on the autocorrelation images, the autocorrelation $C(r)$ at small r were recorded for PLZT thin films with different thickness and plotted in Figure 35e with its best fits.

The thickness dependence of the average correlation length $<\xi>$ obtained from fits is shown in Figure 36. The larger $<\xi>$ in the present work and its maximum value observed for the film with 350 nm in thickness are two aspects to punctuate. The correlation lengths obtained are about 2-3 times larger than those reported in literature for PLZT ceramics at the same composition [56, 254] and comparable to larger values observed for $Ba(Zr,Ti)O_3$-$(Ba,Ca)TiO_3$ (BZT-BCT) thin films [255]. Typical correlation lengths observed for relaxor thin films are ~80 nm [252]. Although it remains unclear the relation between the correlation length and its real

value at the macro scale, we assume that < ξ > is directly related to the average size of PNRs in relaxors [252, 256] and thus can be used to measure the polarization disorder on the surface of the relaxor films. The great similarity between results shown in Figure 32 and Figure 33 suggest a correspondence between grain size and correlation length. Based on these results, there was smaller correlation length in small grains and higher correlation length for large grains. These results agree with the previous report on the grain size effect in PLZT ceramics, which demonstrated larger correlation length for larger grain size [255].

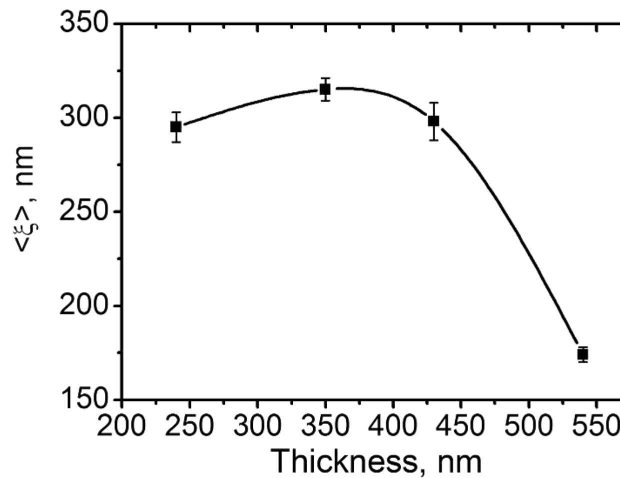

Figure 36: Thickness dependence of correlation length of PLZT films. Lines in (a) are best fits of <C(r)> while in (b) lines are drawn as a guide to the eye

Large correlation lengths obtained here suggest larger PNRs in the investigated PLZT thin films. The large size of PNRs (ξ~151 nm) reported in BZT-0.5BCT/LNO thin films is due to stronger polar correlation in thin films with a LNO seed layer grown on the film-substrate interface such that the interface induced by the LNO seed layer is more conducive to nucleation and coalescence for larger nanodomains [255]. In our films of PLZT, the large values of the PNRs sizes are certainly due to other mechanisms. Chemical substitution, as introduction of La^{3+} ions, and lattice defects introduce extra charges or dipolar entities in mixed ABO_3 perovskites. At very high temperatures, the dipole moment present in the relaxor state is not so well-defined due to large thermal fluctuation. However, on cooling, the dipolar moments manifests itself as small PNRs below the so-called Burns Temperature [26].

The feature of the nanodomains at room temperature depends on the thermal history. On cooling in the absence of biasing field, the domains can either become largely enough to produce macrodomains that permeate the whole sample or leading to a freezing in nanodomains with random orientation. The first assumption leads to a cooperative FE state while the second

one leads to a RE state with randomly oriented nanodomains. In a presence of a biasing electric field during the cooling process, it is expected an alignment of domains followed by an increase in their correlation length, leading to a nano-to-macrodomain transition in PLZT [26]. The increase observed in the correlation length with increasing the self-polarization factor for thinner films (correspondent to larger grains) is a strong evidence of the built-in electric field effects on the alignment of macrodomains in the grains.

4.2.4. Piezoelectric Hysteresis Loops and Local Polarization Relaxation in PLZT thin films by Switching Spectroscopy PFM

The application of FE materials for electronic devices necessarily needs a deep quantitative analysis of the local switching behavior, including imprint effect, coercitivity, remnant and saturation responses, and work of switching [152]. The SS-PFM technique (already described in this work) was used as a tool for investigation of the switching properties at nanoscale of PLZT thin films. The study includes the analysis of switching domains as a function of thickness film, pulse duration, and magnitude of the DC external applied field.

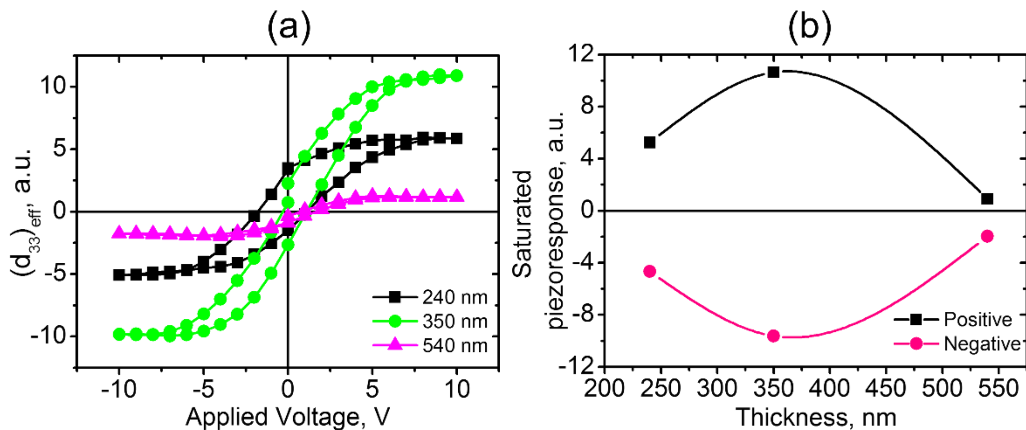

Figure 37: Hysteresis loops measured for PLZT thin films at a different thickness as a function of applied voltage using 1 s of the pulse duration of the DC external bias (b) and the saturated piezoresponse as a function of thin film thickness.

The SS-PFM mode was implemented on a commercial AFM (Ntegra Aura, NTMDT, Russia) using both conventional polarization imaging, time and voltage spectroscopy methods to study the local switching properties of the films. During the PFM measurements, the probing AC (amplitude 1 V, frequency 50 kHz) was applied between a conduction tip (Budget sensor Multi75E-G: Si cantilever covered by Pt, spring constant 3N/m, resonance frequency 75 kHz) and the bottom electrode. The PFM response was detected via external lock-in amplifier system (SR830, Stanford Research, USA).

Measurements of local hysteresis loops are of great importance in polycrystalline ferroelectrics because they can quantify polarization switching on a very small scale [257]. Thus, in order to determine the thickness effect of the switching and electromechanical properties on the nanoscale, measurements were carried out by positioning the conductive tip at the center of grains possessing intermediate contrast in the PFM images. Ten local piezoresponse hysteresis loops were acquired for each sample. Figure 37a and Figure 37b show representative local hysteresis loops PLZT film for 240 nm, 350 nm, and 540 nm in thickness and the saturated piezoresponse as a function of thin film thickness, respectively.

The hysteresis loops are clearly different in shape depending on the film thickness. As a first observation, the loops become slimmer as the thickness is increased. The average coercive electric fields obtained from the experiments resulted in $E_c = 60$ kV/cm, 20 kV/cm and 6 kV/cm for the films with the thickness of 240 nm, 350 nm, and 540 nm, respectively. Here, E_c is defined as $(E_c^+ - E_c^-)/2$. The evolution of E_c in our films is quite different from one reported in (111)-oriented PLZT thin films with 10%-La content [5], in which the results showed an increasing of E_c with film thickness. In the latter case, Ferri *et al.* [5] have suggested the influence of space charges localized at the film/electrode or film/tip interfaces. In the case of trapped charges localized in the interfaces, it may depend on thickness film, increasing the coercitivity as it decreases the film thickness. Also, thin films of $0.7Pb(Mg_{1/3}Nb_{2/3})O_3$–$0.3PbTiO_3$ (PMN–PT70/30) have exhibited no significantly effect on the average coercive field for films thicker than 200 nm [258].

Size effects of $0.8SrBi_2Ta_2O_9$–$0.2Bi_3TiNbO_9$ thin films were investigated by Zhu *et al* [259] and they reported a specific thickness dependence of the coercitivity with the existence of a critical thickness. In these results, for films thinner than a critical value, the coercitivity increased with thickness increasing, while for thicker ones the coercitivity decreases with film thickness increasing. The thickness dependence of the coercive electric field in FE thin films was numerically simulated based on the Potts model with nearest-neighbor interactions between dipole moments by Hu *et al.* [260]. They reported that for large thickness, experimental results where E_c decreases with thickness increasing could be reproduced from Monte-Carlo simulation*. Otherwise, for thinner films, simulations have obtained an increasing of E_c with thickness by polarization switching mechanisms.

* This simulation uses random sampling and statistical modelling to estimate mathematical functions and mimic the operations of complex systems [273].

The thickness dependence of the coercitivity in our PLZT thin films seems to agree with the simulations reported by Hu *et al* [260] for film thickness larger than the critical value, in which the E_c decreases with thickness increasing. When the thickness of the film is considerably small, the film is basically single-domain [261] and as the thickness increases, there will be more dipole moments inside the same domain structure, being necessary more energy to flip all dipoles simultaneously. However, for films larger than the critical value the sample becomes multi-domains and the switching is essentially through the domain wall motion, decreasing consequently the coercitivity with the film thickness of our PLZT thin films.

The piezoresponse hysteresis loops presented in Figure 37a are systematically shifted to positive voltage values, stressing the imprint behavior of the local switching, generally defined as a tendency of one polarization state to become more stable than the opposite one [262]. The shift S (defined as $E_c^+ + E_c^-$) clearly becomes more positive as long we increase the thickness. This shift may arise from the experimental setup through the asymmetry of the tip/film/bottom electrode configuration [5]. Gruverman *et al.* [263] reported that compressive stress also resulted in complete switching into the positive polarization state. As we already have described previously, the refinement of the XRD of our PLZT thin films has shown that the microstrain increases with the thickness linearly. This microstrain effect could be contributing to the imprint phenomena observed in our films, mainly because the shift of the piezoresponse loops becomes more positive as the thickness increases. Also, we should consider that the imprint effect may originate from space charges at film/electrode or at film/tip interfaces. Some band gap states can exist near the surface or near the bottom electrode, and these bands can be filled by charges. In this way, electrons could be trapped in these band gap states, leading to the building of a negative space charge near the film surface and screening the positive applied voltage, causing the deviation of the piezoloops. In the presence of a local electric field generated by space charges or by the Schottky barrier heights, the double-well thermodynamic potential of each FE domain is modified in an asymmetric manner, favoring in one specific direction and then presenting a shifting in the piezoloops [7].

Macroscopically, the switching of FE domains occurs via the nucleation and growth of a large number of reverse domains in the situation in which the applied electric field is uniform, reflecting the switching average over the entire sample under the electrode. However, in the piezoresponse hysteresis loops, the electric field applied is strongly localized and inhomogeneous. Therefore, the switching onset starts with the nucleation of a single domain under the conductive tip [264]. In all hysteresis loops observed in Figure 37a, the piezoresponse

achieves a maximum value before the voltage achieve its maximum, and this maximum is called as a saturation of the piezoresponse.

The behavior of the piezoresponse saturated as a function of the film thickness is shown in Figure 37b. This indicates that the nucleation and the growth of reversed domains have reached the maximum and it is thickness dependent. The saturated piezoresponse increases with film thickness reaching a piezoresponse of maximum near thickness around 350 nm and then decreases. Worthy to notice that the behavior of the grain size of PLZT thin films with film thickness has shown similar behavior when compared with the remnant piezoresponse. This result also suggests an intrinsic relationship between grain size and saturated piezoelectric response in our films. The explanation for this behavior may be the same of that to explain the behavior of the FWHM as a function of the thickness. In the film with 350 nm in thickness, we obtained the larger grain size and, consequently, a more complex structure of the crystallite orientation is possible, resulting in an increasing of polar state reorientation along the external field and, consequently, increasing the saturated piezoresponse.

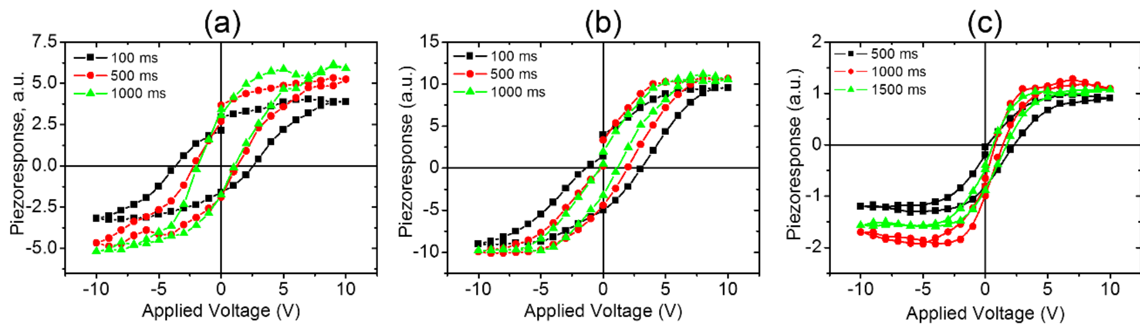

Figure 38: Hysteresis loops measured at different pulse durations for PLZT thin films with a) 240 nm, b) 350 nm and c) 540 nm of thickness.

In order to determine the pulse duration dependence at different PLZT thin film thicknesses of the switching and electromechanical properties at nanoscale, measurements have been performed by placing the probing tip at the centre of the grains in these film thicknesses. Figure 38 shows representative piezoelectric response hysteretic loops of the 240 nm, 350 nm, and 540 nm thick films for different DC pulse durations, t_p. In a first moment, the loops are methodically shifted towards both positive and negative voltage values depending on the thickness of the PLZT sample is observed as the DC pulse duration increases from 500 ms to 1000-1500 ms. The coercive electric field shows different behavior with DC pulse durations in all PLZT thickness.

From piezoresponse hysteresis loops, we obtained valuable information about the switching and electromechanical properties. The remnant polarization (positive and negative)

and the average remnant polarization, given by $d_{33,r} = (P_r^+ - P_r^-)/2$, the imprint effect $(E_c^+ + E_c^-)$ and the coercive electric field $(E_c^+ - E_c^-)/2$ were obtained both as a function of the film thickness as a function of the pulse duration and are shown in Figure 39.

Figure 39a presents the d_{33} remnant piezoresponse ($d_{33,r}$) as a function of the film thickness. We clearly observe a thickness dependence of $d_{33,r}$ for pulse durations with 500 ms and 100 ms, respectively. All the values of $d_{33,r}$ in the thicker film are considerably small and positives. The asymmetry observed in 240 nm and 350 nm thin films between the positive and negative values of $d_{33,r}$ is an indicative of an imprint effect and it is probably due to the presence of an internal (built-in) electric field [149].

Figure 39b shows that $d_{33,r}$ of the thinner (240 nm) and the thicker (540 nm) films remains approximately constant as the pulse duration changes from 100 ms to 1000 ms and from 500 ms to 1500 ms, respectively. A significant variation of $d_{33,r}$ is observed in 350 nm in thickness as we can see in Figure 39c as a function of film thickness for different pulse duration. Its value decreases from ~4.0 to ~2.5 in the pulse duration from 500 to 1000 ms.

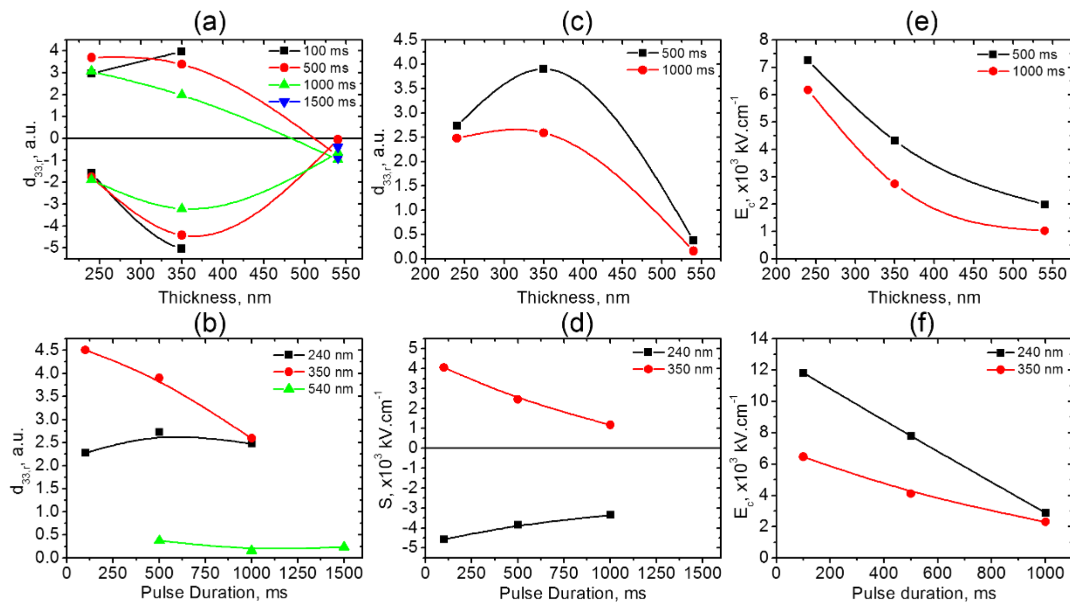

Figure 39: (a) Positive and negative $d_{33,r}$ remnant piezoresponse signal as a function of thin film thickness for different DC pulse durations. Average remnant piezoresponse $d_{33,r} = (P_r^+ - P_r^-)/2$ as (b) a function of the DC pulse duration for different thin film thicknesses and (c) as a function of the film thickness for different DC pulse durations. The DC pulse duration dependence on imprint effect $(E_c^+ + E_c^-)$ is shown in (d) and the coercive electric field (E_c) dependence with thickness and pulse duration are illustrated in (e) and (f), respectively. The lines are just guides to the eyes.

Worthy to notice the similarity between the thickness dependence of the $d_{33,r}$ (Figure 39c) and the thickness dependence of the grain size in our PLZT thin films (Figure 32). Kim *et al.* [265] have observed the same behavior and have attributed this effect to the coupling

between local strain and polarization. The $d_{33,r}$ of small grains is significant reduced, because the mechanical strain from interaction between the surrounding grains is relatively large on small grains. As we have observed, the increasing of the DC pulse duration in films with small grains does not change significantly as in larger grains. We suggest that the considerable decrease of $d_{33,r}$ in our film with 350 nm in thickness with increment of the DC pulse duration could be mostly attributed to the reduction of non-180º FE domains. This reduction may originate from trapped charges released from surrounding grains due to a longer time of the DC pulse applied into the grain. These spaces charges can significantly influence the non-180º domain wall motion, decreasing consequently the contribution of 180º domains in the local $d_{33,r}$ due to the increasing of the mechanical clamping.

The imprint effect is illustrated in Figure 39d as a function of the pulse duration. We can observe a decreasing as the pulse duration is increased. In the 350 nm in thickness, we observe a faster asymmetry decreasing than the thinner film. The coercive field has also shown a decreasing with the film thickness and with the pulse duration as we can observe in Figure 39(e-f). This effect could be attributed to the increment of the mechanical clamping in the grain due to surrounding grains in higher DC pulse durations hindering the self-polarization effect in the films. Therefore, this can explain as well the decreasing of the coercive field with pulse duration, once the local strain originated by the mechanical clamping could hinder non-180º FE domain wall motion and decrease consequently the electric field needed to cause a switching in the local polarization.

While the initial piezoresponse was rather weak for the PLZT thin films a strong piezoelectric signal can be induced by application of a DC external voltage. Moreover, the polarization direction of the FE domains can be switched to an antiparallel one, as we can observe in Figure 37a. At the same time, the induced piezoresponse state of relaxor PLZT thin films was studied using SS-PFM in order to investigate the relaxation of these domains as a function of time. With a purpose of an investigation, the relaxation was performed at various local of the film. The conductive tip was positioned in one specific location and the positive and negative induced piezoresponse was measured as a function of time after applying DC pulses of different magnitudes V_{dc} and pulse durations t_p. The magnitude of V_{dc} was chosen to be larger than the coercive voltage estimated from the piezoresponse loops presented in Figure 37.

The time dependences of the PFM signal measured after the DC poling voltage that had been switched off are shown in Figure 40 for DC pulses of +10 V and -10V with 1 second of

duration. One can see that the positive and negative induced piezoresponse decay relatively fast within seconds for all thicknesses of the PLZT samples. The relaxation of the induced piezoresponse was better described by the Kolrausch-William-Watts (KWW) type dependence: $(d_{33})_{eff} \sim \exp\left[-(t/\tau)^{\beta}\right]$ where t is the time, and τ and β are the fitting parameters.

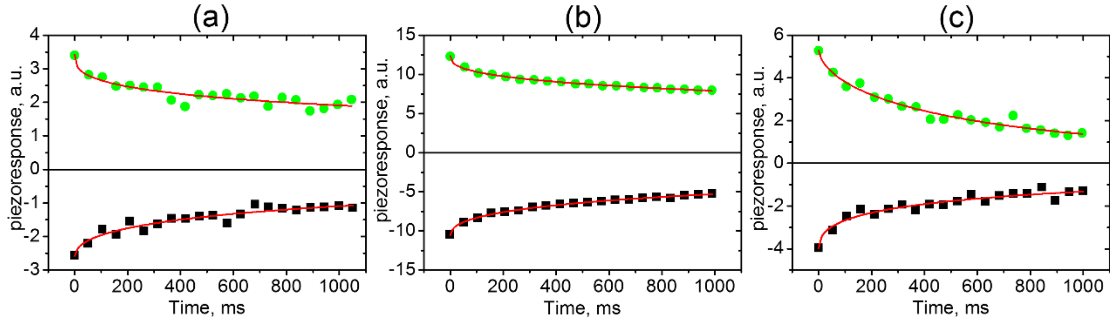

Figure 40: Time dependences of the positive and negative induced piezoresponse measured after applying a voltage pulse of V_{dc} = 10 V and pulse duration t_p = 1s for PLZT thin films with (a) 240 nm, (b) 350 nm, and (c) 540 nm of thickness.

All the fitting curves have shown that β is almost constant (~0.5-0.6) in the electric field range of 100-600 kV/cm. The KWW dependence is generally applied to describe a thermally activated relaxation in systems with a distribution of relaxation times [153]. The dc pulses applied locally were 5 V, 10 V, and 15 V, respectively. Nevertheless, in spite of the external voltage were exactly the same in all film thickness, the local electric field felt under the tip and through the film is different depending on the thickness. Thus, the behavior of the relaxation times as a function of the external electric field felt by the film thickness, using $E = V/L$ where E is the electric field, V is the DC applied voltage, and L is the film thickness, is shown in Figure 41a.

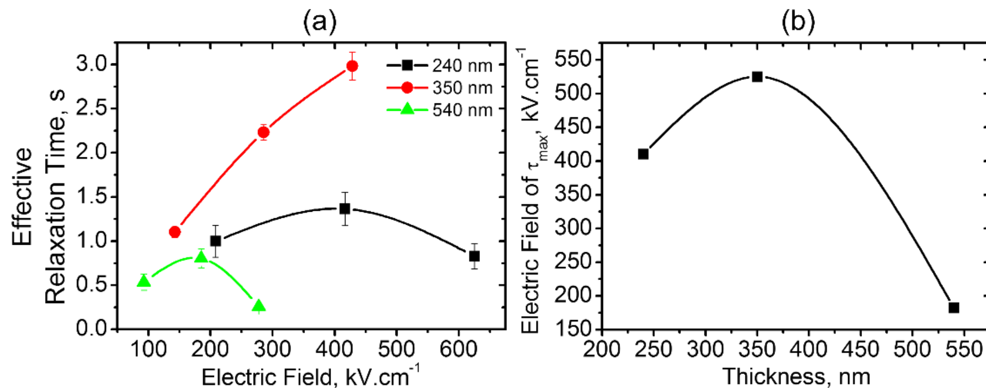

Figure 41: (a) Effective relaxation times (s) as a function of the magnitude of the applied electric field for the PLZT thin films in different thickness and (b) electric field of maximum characteristic time as a function of the PLZT thin film thickness.

Different film thicknesses exhibit a distinct distribution of relaxation times as a function of the electric field. Our results are in agreement with other reports where the onset of the polar state has been completely reversible less than some seconds [266]. Except for the film with 350 nm of thickness, the relaxation of the induced piezoresponse exhibits a wide peak in the electric field dependence of the relaxation time τ observed in the PLZT with 240 nm and 540 nm of thickness. If in our measurements we had applied an external electric field higher than 600 kV/cm in the film with 350 nm in thickness, we would also expect a maximum of relaxation time. Therefore, fitting the data points using a Gaussian function, given by $\tau \propto \tau_0 \exp\left[-(E-E_m)^2/2\sigma^2\right]$ where τ_0 is a fitting parameter, E is the electric field, E_m is the electric field of maximum relaxation time, and σ^2 is the statistical parameter (variance), we have obtained by extrapolation the peak of the possible maximum relaxation time for the film with 350 nm of thickness.

In order to understand the thickness effect of the peak shift of the maximum of the relaxation time, we have plotted in Figure 41b the electric field of maximum relaxation time as a function of the film thickness. The electric field of τ_{max} increases with thickness until reaches 350 nm in thickness, and then, decreasing considerably the relaxation time with thickness. In other words, the induced piezoelectric domains in which its decay is as long as possible with electric field dependence achieves a maximum in the film with 350 nm in thickness.

Worth stressing here the behavior of the electric field of maximum relaxation time as a function of film thickness (Figure 41b) is quite similar to the behavior of the grain size (Figure 32a). The FE domain relaxation seems to follow the grain size, i.e., for larger grains, the relaxation is much slower than smaller grains. The results that we have shown here in this work are in agreement with reports of relaxor $0.9Pb(Mg_{1/3}Nb_{2/3})O_3$-$0.1PbTiO_3$ (PMN-PT) films investigated by Kholkin *et al*. [267].

Our experimental results just revealed a distinct grain size effect in relaxor PLZT thin film in the FE properties, i.e., the strength of the local remnant electromechanical coupling (Figure 37) and domain relaxation (Figure 41b) are closely related to the grain size in our PLZT thin films. It is obvious that the grain boundaries may affect significantly the properties of the polar clusters and perturbs the periodicity of domain structure [261]. The reasons for such strong relationship between grain size and physical properties at the nanoscale may be explained as follows. The influence of surrounding grains that can cause a mechanical clamping in a specific grain underneath the tip seems to be dependent on its size. The residual strain after strain relaxation due to thermal mismatch have been reported by Choi & Suresh [268] and they

suggested to be inversely proportional to the grain size. This way, it is probable that the mechanical interaction between the grains leads to a high level of the compressive pressure inside small grains [267]. Consequently, the growth and nucleation of polar domains under an external electric field may be notably restricted in smaller grains via the strong coupling between local strain and polarization. Thus, the piezoresponse is highly reduced in smaller grains [46]. In small grains, polar clusters may be completely frozen-in due to high mechanical clamping and the signal measured is essentially due to the paraelectric matrix.

It is believed that grain size effects are equivalent to the local variations of the phase transition temperatures that causes additional diffuseness of the dielectric permittivity versus temperature dependence. We should also consider that the size effect observed in this work can be related to the possible grain size dependence of the mean size of polar clusters inside the grains, possibly due to mechanical clamping effect again. Studies on PMN ceramics have exhibited a grain size dependence of nanoscale ordered regions using Transmission Electron Microscopy (TEM) [269], where the polar nanoscale regions have shown to be smaller in fine-grained than those of coarse-grained PMN ceramics.

In summary, we have observed a clear correlation between the values of the piezoelectric coefficients, the switching and the relaxation of polar domains with the size of the respective grains in relaxor ferroelectric PLZT thin films. Thus, the influence of the grain size on the dynamics of polar clusters was confirmed, suggesting that the relaxation of induced domains is much slower in large grains, indicating the existence of different relaxation times of different grains, probably due to the mean size of polar cluster inside the grains [267].

4.2.5. Summary

Thin films of polycrystalline random oriented PLZT with 9%-La content and 65/35 molar ratio of Ti/Zr were prepared by the polymeric method, using the modified Pechini technique. In summary, our films of PLZT have shown a thickness dependence on structural properties, as lattice parameters, crystallite size, and microstrain. The macroscopic ferroelectric properties have exhibited a frequency and temperature dependences for the PLZT thin film with 540 nm in thickness. The decreasing of $\Delta P_r = P_r^+ - P_r^-$ and $\Delta E_c = E_c^+ - E_c^-$ at lower temperatures have indicated the coexistence of both relaxor glass-like and ferroelectric state, with a slow conversion from relaxor to ferroelectric order with lowering temperature. The frequency dependence of the remnant polarization and the coercive field at different temperatures has shown many details about domain switching properties, as well the possibility

of the observation of either a re-entrant dipole glass behavior or an activated electric field effect in our PLZT thin films.

The microstructure analysis has revealed the spongy features of the samples at different thermal treatment and different film thickness. In addition, SEM micrographs have exhibited distinct characteristics concerning the degree of porosity of the film thickness, suggesting a temperature dependence of the porous development and a more densification of deposited layers near the substrate.

The thickness effect on grain size and local piezoelectric properties were investigated and correlated with structural properties. PFM has been used to study the piezoelectric properties at nanoscale of the PLZT thin films. Grain size distributions obtained from topography images showed to present a maximum around 350 nm in thickness. The results of the piezoelectric histograms obtained from PFM images for the PLZT thin films has revealed an intrinsic relationship between the coexisting polarization directions and the grain size. The complexity of the internal crystalline structure in larger grains seems to influence significantly in the piezoresponse distribution in our films. The quantitative analysis of the symmetry and periodicity of nanodomains structure were studied using the autocorrelation function. The average correlated radius has shown a similar behavior with the grain size, i.e., smaller correlation lengths in smaller grains, suggesting a grain size dependence of the size of the polar nanoregions.

The switching properties of the relaxor ferroelectric material PLZT thin film also has revealed a strong thickness dependence. The coercitivity in our films has shown to increase with decreasing film thickness, being associated with the presence of a multi-domain structure. The piezoresponse hysteresis loops presented a shift to positive voltage values stressing the imprint behavior of the local switching and they become more accentuated as the film thickness increases. The saturated piezoresponse showed a large peak with its maximum around 350 nm in thickness and presented similar grain size dependence. The imprint effect and the coercive electric field showed a grain size and pulse duration dependences, in which it was attributed the mechanical clamping effect inside grains as mainly contribution factor. Also, the relaxation times of the induced piezoresponse of the PLZT thin films follows the grain size, i.e., for larger grains, the relaxation is much slower than smaller grains, corroborating these results with other reports in PMN-Pt films. This can be attributed to the mean size of the polar clusters inside the grains, which is also grain size dependent due to mechanical clamping.

5. FINAL CONSIDERATIONS

Ferroelectric relaxor thin films of strontium barium niobate with 75% of Sr/Ba molar ratio (SBN) and lead lanthanum zirconate titanate with 9%-La content and 65/35 of Zr/Ti composition (PLZT) were prepared by the polymeric method. Physical properties at macro and microscale were investigated in these films. In SBN thin film we have confirmed its relaxor characteristics through the temperature and frequency dependence of the dielectric coefficient dispersion. However, such measurements were not possible in PLZT thin films because in all electrodes were in short-circuit. One believes that the high degree of porosity may have influenced the gold electrode deposition by RF-sputtering. For future works, thin films of PLZT and SBN can be prepared in order to reduce the porosity and possibly obtain the necessary dielectric measurements.

The lowering of temperature of maximum dielectric permittivity at 10 kHz comparing with SBN single crystal with same nominal composition needs more detailed investigations to better understand the effect. Even though local shifts on stoichiometry have been proposed to explain the lowering of temperature, we must obtain more data about the influence of defect densities on the structure, in order to really comprehend the shift observed in the dielectric measurements.

Both relaxor systems have shown an intrinsic dependence of the piezoelectric response with grain size and the domain states. In PLZT thin films it was possible to observe the effect of the grain size on the switching and relaxation properties using SSPFM. Application of several voltage magnitudes and pulse duration have indicated the appearance of depolarizing electric fields possibly due to charge movements in both SBN and PLZT thin films.

The possible re-entrant behavior discussed in our PLZT thin film has to be carefully investigated. The indication of an increasing of the coercive electric field for lower temperature can be explained by the low nucleation rate of new ferroelectric domains as temperature decreases, decreasing consequently the remnant polarization for low temperatures. Therefore, further experiments have to be performed to clarify this phenomena.

REFERENCES

[1] F. Jona and G. Shirane, Ferroelectric Crystals, New York: Dover Publications, 1993.

[2] H. T. Martirena and J. C. Burfoot, "Grain-size effects on properties of some ferroelectric ceramics," *J. Phys. C: Solid State Phys.,* vol. 7, pp. 3182-3192, 1974.

[3] Y. Yano, K. Lijima, Y. Daitoh, T. Terashima, Y. Bando, Y. Watanabe, H. Kasatani and H. Terauchi, "Epitaxial growth and dielectric properties of BaTiO3 films on Pt electrodes by reactive evaporation," *Journal of Applied Physics,* vol. 76, no. 12, 1994.

[4] K. R. Udayakumar, P. J. Shuele, J. Chen, S. B. Krupanighi and L. E. Cross, "Thickness-dependent electrical characteristics of lead zirconate titanate thin films," *Journal of Applied Physics,* vol. 77, no. 8, 1994.

[5] A. Ferri, S. Saitzek, A. Da Costa, R. Desfeux, G. Leclerc, R. Bouregba and G. Poullain, "Thickness dependence of the nanoscale piezoelectric properties measured by piezoresponse force microscopy on (111)-oriented PLZT 10/40/60 thin films," *Surface Science,* vol. 602, p. 1987–1992, 2008.

[6] D. Damjanovic, "Ferroelectric, dielectric and piezoelectric properties of ferroelectric thin films and ceramics," *Reports on Progress in Physics,* vol. 61, p. 1267–1324, 1998.

[7] V. C. Lo and Z. J. Chen, "Simulation of the Effects of Space Charge and Schottky Barriers on Ferroelectric Thin Film," *IEEE Transactions on Ultrasonics, Ferroelectrics, and Frequency Control,* vol. 49, no. 7, pp. 980-986, 2002.

[8] R. Ahluwalia, A. K. Tagantsev, P. Yudin, N. SEtter, N. Ng and D. J. Srolovitz, "Influence of flexoelectric coupling on domain patterns in ferroelectrics," *Physical Review B,* vol. 89, pp. 174105(1-4), 2014.

[9] A. Gruverman, B. J. Rodriguez, A. I. Kingon, R. J. Nemanich, A. K. Tagantsev, J. S. Cross and M. Tsukada, "Mechanical stress effect on imprint behavior of integrated ferroelectric capacitors," *Applied Physics Letters,* vol. 83, no. 4, pp. 728-730.

[10] D. Damjanovic, P. Muralt and N. Setter, "Ferroelectric Sensors," *IEEE Sensors Journal,* vol. 1, no. 3, pp. 191-206, 2001.

[11] M. Yoichi, "Applications of Piezoelectric Actuator," *NEC Technical Journal,* vol. 1, no. 5, pp. 82-86, 2006.

[12] J. E. Huber, "Micromechanical Modelling of Ferroelectric Films," *MRS Proceedings,* vol. 881, 2005.

[13] R. Guo, , L. You, Y. Zhou, Z. S. Lim, L. Chen, R. RAmesh and J. Wang, "Non-volatile memory based on the ferroelectric photovoltaic effect," *Nature Communications,* vol. 4, no. 1990, pp. 1-5, 2013.

[14] J. F. Scott, “Applications of Modern Ferroelectrics,” *Science,* vol. 315, no. 5814, pp. 954-959, 2007.

[15] R. Mankowsky, A. v. Hoegen, M. Först and A. Cavalleri, “Ultrafast reversal of the ferroelectric polarization,” *Phys.Rev. Lett.,* vol. 118, no. 197601, 2017.

[16] M. Scigaj, N. Dix, J. Gázquez, M. Varela, I. Fina, N. Domingo, G. Herranz, V. Skumryev, J. Fontcuberta and F. Sanchez, “Monolithic integration of room-temperature multifunctional $BaTiO_3$-$CoFe_2O_4$ epitaxial heterostructuress on Si(001),” *Scientific Reports,* vol. 6, no. 31870, pp. 1-10, 2016.

[17] M. A. Hintermüller, B. Jakoby and E. K. Reichel, “Numerical and experimental analysis of an acoustic micropump utilizing a flexible printed circuit board as an actuator,” *Sensors and Actuators A: Physical,* pp. 1-24, 2017.

[18] J. Cronin, S. Sun and T. Davenport, “Method for fabricating a damascene self-aligned ferroelectric random access memory (F-RAM) having a ferroelectric capacitor aligned with a three dimensional transistor structure”. USA Patent US9318693 B2, 19 abr. 2016.

[19] A. A. Bokov and Z. -G. Ye, “Universal relaxor polarization in $Pb(Mg_{1/3}Nb_{2/3})O_3$ and related materials,” *Physical Review B,* vol. 66, no. 6, p. 064103, 2002.

[20] A. Bokov and Z. Ye, “Dielectric relaxation in relaxor ferroelectrics,” *Journal of Advanced Dielectrics,* vol. 2, no. 2, pp. 1-24, 2012.

[21] A. Simon, J. Ravez and M. Maglione, “Relaxor properties of $Ba_{0.9}Bi_{0.067}(Ti_{1-x}Zr_x)O_3$ ceramics,” *Solid State Sciences,* vol. 7, pp. 925-930, 2005.

[22] G. A. Smolenskii and A. I. Agranovskaya, “Dielectric polarization and losses of some complex compounds,” *Sov. Phys. - Tech. Phys.,* vol. 3, pp. 1380-1382, 1958.

[23] V. Fridkin and S. Ducharme, Ferroelectricity and Ferroelectric Phase Transition, Springer, 2013.

[24] G. Samara, “The relaxational properties of compositionally disordered ABO3 perovskites,” *J. Phys.: Condens. Matter,* vol. 15, pp. R367-R411, 2003.

[25] Z. Kutnjak, J. Petzelt and R. Blinc, “The giant electromechanical response in ferroelectric relaxors as a critical phenomenon,” *Nature,* vol. 441, pp. 956-959, 2006.

[26] W. Kleemann, “The relaxor enigma - charge disorder and random fields in ferroelectrics,” *Journal of Materials Science: Frontiers of Ferroelectricity,* vol. 41, pp. 129-136, 2006.

[27] M. Dawber, K. M. Rabe and J. F. Scott, “Physics of Thin-Film Ferroelectric Oxides,” *Reviews of Modern Physics,* vol. 77, pp. 1083-1130, October 2005.

[28] E. Soergel, “Piezoresponse force microscopy (PFM),” *J. Phys. D: Appl. Phys.,* vol. 44, p. 464003, 2011.

[29] N. Setter, D. Damjanovic, L. Eng, G. Fox, S. Gevorgian, S. Hong, A. Kingon , H. Kohlstedt, N. Y. Park, G. B. Stephenson, I. Stolitchnov, A. K. Taganstev, D. V. Taylor, T. Yamada and S. Streiffer, “Ferroelectric thin films: Review of materials, properties, and applications,” *Journal of Applied Physics,* vol. 5, no. 100, pp. 051606(1-47), 2006.

[30] K. -C. Kao, Dielectric Phenomena in Solids: with emphasis on physical concepts of electronic processes, Elsevier, 2004.

[31] R. W. Whatmore and A. J. Bell, “Pyroelectric ceramics in the lead zirconate-lead titanate-lead iron niobate system,” *Ferroelectrics,* vol. 35, no. 1-4, pp. 155-160, 07 Fev 1981.

[32] J. Lian and T. Shiosaki, “Pyroelectric properties of $Pb[Zr, Ti, (Zn, Nb)]O_3$ solid solution ceramics,” *Ferroelectrics,* vol. 118, no. 1, pp. 135-141, 1990.

[33] P. Kumar, S. Sharma, O. P. Thakur, C. Prakash and T. C. Goel, “Dielectric, piezoelectric and pyroelectric properties of,” *Ceramics International,* vol. 30, no. 1, pp. 585-589, 2004.

[34] J. Zhang, G. Wang, F. Gao, C. Mao, F. Cao and X. Dong, “Influence of Sr/Ba ratio on the dielectric, ferroelectric and pyroelectric properties of strontium barium niobate ceramics,” *Ceramics International,* vol. 39, pp. 1971-1976, 2013.

[35] K. Matyjasek, J. Dec, S. Miga and T. Łukasiewicz, “Ferroelectric and Dielectric Characterization Studies,” *Condensed Matter Physics: Proceedings Paper,* vol. 16, pp. 1-10, 2013.

[36] S. M. Kaczmarek, M. Orlowski, T. Skibiñski, A. Jasik and L. Ivleva, “Ferroelectric properties of relaxor type SBN single crystals pure and doped with Cr, Ni, and Ce.,” *Rev. Adv. Mater. Sci.,* vol. 23, pp. 80-87, 2010.

[37] M. P. Trubelja, E. Ryba and D. K. Smith, “A study of positional disorder in strontium barium niobate,” *Journal of material science,* vol. 31, pp. 1435-1443, 1996.

[38] C. J. Huang, K. Li, X. Q. Liu, X. L. Zhu and X. M. Chen, “Effects of A1/A2-Sites Occupancy upon Ferroelectric Transition in $(Sr_xBa_{1-x})Nb_2O_6$ Tungsten Bronze Ceramics,” *J. am. Ceram. Soc.,* vol. 97, pp. 507-512, 2014.

[39] M.-S. Kim, P. Wang, J.-H. Lee, J.-J. Kim, H. Y. Lee and S.-H. Cho, “Site Occupancy and Dielectric Characteristics of Strontium Barium Niobate Ceramics: Sr/Ba Ratio Dependence,” *The Japan Society of Applied Physics,* vol. 41, 2002.

[40] S. N. Gvasaliya, R. A. Cowley, L. I. Ivleva, S. G. Lushnikov, B. Roessli and A. Zheludev, “Phase transition of the uniaxial disordered ferroelectric $Sr_{0.61}Ba_{0.39}Nb_2O_6$,” *J. Phys.: Condens. Matter,* vol. 26, no. 185901, pp. 1-6, 2014.

[41] V. A. Shikhova, V. Y. Shur, D. V. Pelegov and L. I. Ivleva, "Double Loops Formation in $Sr_{0.75}Ba_{0.25}Nb_2O_6$ Single Crystals in Relaxor Phase," *Ferroelectrics,* vol. 443, pp. 116-123, 2013.

[42] M. Cuniot-Ponsard, Strontium Barium Niobate Thin Films for Dielectric and Electro-optic applications, M. Lallart, Ed., Ferroelectrics - Material Aspects, 2011.

[43] P. V. Lenzo, E. G. Spencer and A. A. Ballman, "Electro-Optic Coefficients of Ferroelectric Strontium Barium Niobate," *Applied Physics Letter,* vol. 11, no. 1, pp. 23-24, July 1967.

[44] H. W. Huang, V. Dwight and R. R. Neuurgaonkar, "Anisotropic Glasslike Characteristics of Strontium Barium Niobate Relaxors," *Journal of Applied Physics,* vol. 76, pp. 490-496, 1994.

[45] T. Lukasiewicza, M. A. Swirkowicza, J. Decb, W. Hofman and W. Szyrski, "Strontium-barium niobate single crystals, growth and ferroelectric properties," *Journal of Crystal Growth,* vol. 310, pp. 1464-1469, 2008.

[46] V. V. Shvartsman, A. Y. Emelyanov and A. L. Kholkin, "Local hysteresis and grain size effect in $Pb(Mg_{1/3}Nb_{2/3})O_3$-$PbTiO_3$ thin films," *Applied Physics Letters,* vol. 81, 2002.

[47] A. L. Kholkin, S. V. Kalinin, A. Roelofs and A. Gruverman, "Review of ferroelectric domain imaging by piezoresponse force microscopy," in *Scanning Probe Microscopy: Electrical and Electromechanical Phenomena at Nanoscale*, New York, Springer Science+Business Media, 2007.

[48] R. Gysel, A. K. Tagantsev, I. Stolichnov, N. Setter and M. Pavius, "Ferroelectric film switching via oblique domain growth observed by cross-sectional nanoscale imaging," *Applied Physics Letters,* vol. 89, pp. 082906-082910, 2006.

[49] J. P. Cruz, E. Joanni and P. Vilarinho, "Thickness effect on the dielectric, ferroelectric, and piezoelectric properties of ferroelectric lead zirconate titanate thin films," *Journal of Applied Physics,* vol. 11, pp. 114106 (1-8), 2010.

[50] B. Chua, L. Lu, M. O. Lai and G. H. L. Wong, "Effects of complex additives on toughness and electrical properties of PZT ceramics," *Journal of Alloys and Compounds,* vol. 381, pp. 272-277, 2004.

[51] H. Li, Z. Yang , X. Zong and Y. Chang , "High electrical properties of W-additive Mn-modified PZT-PMS-PZN ceramics for high power piezoelectric transformers," *Materials Science and Engineering B: Solid-State Materials for Advanced Technology,* vol. 130, no. 1-2, pp. 288-294, 2006.

[52] S. Chu, T. Chen, I. T. Tsai and W. Water, "Doping effects of Nb additives on the piezoelectric and dielectric properties of PZT ceramics and its application on SAW device," *Sensors and Actuators, A: Physical,* vol. 113, no. 2, pp. 198-203, 2004.

[53] E. Dimitriu, F. Craciun and R. Ramer, “Influence of Li additive on dielectric and piezoelectric properties of PZT ceramics,” *Electrical Engineering,* vol. 3, pp. 641-645, 2007.

[54] C. Filipič, B. Vodopivec, J. Holc, A. Levstik, Z. Kutnjak and H. Beige, “Relaxor and incipient ferroelectric phases in 6.5/65/35 PLZT ceramics,” *Journal of the European Ceramic Society,* vol. 24, pp. 1565-1568, 2004.

[55] G. H. Haertling and C. E. Land, “Hot-Pressed (Pb, La)(Zr, Ti)O_3 Ferroelectric Ceramics for Electrooptic Applications,” *Jounra of American Ceramic Society,* vol. 54, no. 1, pp. 1-11, 1971.

[56] V. V. Shvartsman, A. L. Kholkin, A. Orlova, D. Kiselev, A. A. Bogomolov and A. Stemberg, “Polar nanodomains and local ferroelectric phenomena in relaxor lead lanthanum zirconate titanate ceramics,” *Applied Physics Letters,* vol. 86, p. 202907 (4 pp), 2005.

[57] K. Hirabayashi, “PLZT Electrooptic Ceramic Photonic Devices for Surface-Normal Operation in Trenches Cut Across Arrays of Optical Fiber,” *Journal of Lightwave Technology,* vol. 23, no. 3, pp. 1393-1492, 2005.

[58] G. Rosseti and T. Nishimura, “X-ray and phenomenological studi of lanthanum-modified lead zirconate tiatanates in the vicinity of the relaxor phase transition,” *Ferroelectrics,* vol. 70, pp. 1630-1637, 1991.

[59] S. Teslic and T. Egami, “Local atomic structure of PZT and PLZT studied bu pulsed neutron scattering,” *J. Phys. Chem. Solids,* vol. 57, no. 10, pp. 1537-1543, 1996.

[60] D. Viehland, S. J. Jang, L. E. Cross and M. Wuttig, “Internal strain relaxation and the glassy behavior of La-modified lead zirconate titanate relaxors,” *Journal of Applied Physics,* vol. 69, no. 9, pp. 6595-6602, 1991.

[61] B. Long, S. Jian, S. Ping and L. Zu-Hong, “Mapping Nanoscale Domains in a Sol-Gel-Derived (Pb, La) (Zr, Ti)O3 Thin Film Using Atomic Force Microscopy,” *Chin. Phys. Lett.,* vol. 20, no. 4, pp. 465-470, 2003.

[62] J. F. Scott, “Models for the frequency dependence of coercive field and the size dependence of remanent polarization in ferroelectric thin films,” *Integrated Ferroelectrics,* pp. 71-81, 2006.

[63] D. Griffiths, Introduction to electrodynamics, 3ª ed., New Jersey: Prentice Hall, 1999, p. 537.

[64] J. C. Burfoot and G. W. Taylor, Polar dielectrics and their applications, California: University of California Press, 1979.

[65] J. D. Jackson, Classical electrodynamics, New York: John Wiley & sons, Inc., 1962.

[66] A. Sawada, “Dielectric process of space-charge polariztion for an electrolytic cell with blocking electrodes,” *The Journal of Chemical Physics,* vol. 129, no. 6, 2008.

[67] G. C. Montanari and P. H. F. Morshuis, “Space charge phenomenolgy in polymeric insulating materials,” *IEEE Transactions on dielectrics and electrical Insulation,* vol. 12, no. 4, pp. 754-767, 2005.

[68] G. F. Ferreira, “Polarization in hopping transport,” *Journal of electrostatic,* vol. 11, pp. 113-117, 1981.

[69] A. Tagantsev and G. Gerra, “Interface-induced phenomena in polarization response of ferroelectric thin films,” *Journal of Applied Physics,* vol. 100, no. 5, 2006.

[70] K. M. Rabe, M. Dawber, C. Lichtensteiger, C. Ahn and J.-M. Triscone, “Modern Physics of Ferroelectrics: Essential background,” in *Modern Physics of Ferroelectrics: A modern perspective*, USA, Springer, 2007, pp. 1-30.

[71] D. Voss, M. Lucibella, K. G. Johnson and N. Bennett-Karasik, “March 1880: The Curie Brothers Discover Piezoelectricity,” American Physical Society Sites, 2016. [Online]. Available: https://www.aps.org/publications/apsnews/201403/physicshistory.cfm. [Accessed 28 december 2016].

[72] L. E. Cross and R. E. Newnhan, “History of Ferroelectrics,” *Ceramics and Civilization,* vol. 3, pp. 289-305, 1987.

[73] J. Valasek, “Properties of rochelle salt related to the piezoelectric effect,” *Physical Review,* vol. 20, pp. 639-664, 1922.

[74] G. Busch and P. Scherer, “A New Seignette-Electric Substance,” *Naturwiss,* vol. 23, pp. 737-738, 1935.

[75] C. A. Randall, R. E. Newnham and L. E. Cross, “History of the fisrt ferroelectric oxide, BatiO3,” *Materials Research Institute,* pp. 1-11, 1944.

[76] C. Kittel, Introduction to Solid State Physics, New york: John Wiley & Sons, Inc., 1953.

[77] W. Wersing, W. Heywang, H. Beige and H. Thomann, “The role of Ferroelectricity for piezoelectric materials,” in *Piezoelectricity: Evolution and Future of a Technology*, Spring, 2008, p. 571.

[78] H. Fang, Y. Wang, S. Shang and Z. K. Liu, “Naature of ferroelectric-paraelectric phase transition and origin of negative thermal expansion in $PbTiO_3$,” *Physical Review B-Condensed Matter and Materials Physics,* vol. 91, pp. 1-6, 2015.

[79] Z. K. Liu, Z. Mei and S. L. Shang, “Nature of ferroelectric-paraelectric transition,” *Philosophical Magazine Letters,* vol. 92, no. 8, pp. 399-407, 2012.

[80] M. Dawber, “Matt Dawber's Group,” Department of Physics and Astronomy, 21 11 2016. [Online]. Available: http://mini.physics.sunysb.edu/~mdawber/research.htm. [Accessed 30 dec 2016].

[81] S. V. Kalinin, A. N. Morozovska, L. Q. Chen and B. J. Rodriguez, “Local polarization dynamics in ferroelectric materials,” *Reports Progress on Physics,* vol. 73, no. 1, p. 056502, 2010.

[82] A. Std, “IEEE Standard Definitions of Primary Ferroelectric Terms,” *American National Standard,* vol. 180, pp. 1-13, 1986.

[83] Y. Xu, Ferroelectric Materials and Their Applications, Los Angeles, CA, USA: Elsevier Science Publishers, 1991.

[84] J. C. Slater, “Theory of the Transition in KH2PO4,” *The Journal of Chemical Physics,* vol. 9, no. 16, 1941.

[85] Y. Takagi, “Theory of the transition in KH2PO4 (I)*,” *J. Phys. Soc. Japan,* vol. 3, pp. 271-272, 1948.

[86] A. H. Wilson, Thermodynamics and Statistical Mechanics, London: University Press, 1966, p. 492.

[87] L. D. Landau and E. M. Lifshitz, Statistical Physics, 3ª ed., vol. 5, Pergamon Press Ltd., 1980.

[88] M. Marvan and J. Fousek, “Electrostatic Energy of Ferroelectrics with Nonhomogeneous Distributions of Polarization and Free Charges,” *Physica Status Solidi (b),* vol. 208, no. 2, 1998.

[89] E. B. Tadmor, U. V. Wagmare, G. S. Smith and E. Kaxiras, “Polarization switching in $PbTiO_3$: an ab initio finite element simulation,” *Acta Mater.,* vol. 50, pp. 2989-3002, 2202.

[90] N. B. Gharb, *Dielectric and piezoelectric nonlinearities in oriented* $Pb(Yb_{1/2}Nb_{1/2})O_3$*-*$PbTiO_3$ *thin films,* Pennsylvania State University, 2005, p. 313.

[91] A. L. Kholkin, N. A. Pertsev and A. V. Goltsev, “Piezoelectric and Acoustic Materials for Transducer Applications,” in *Piezoelectricity and Crystal Symmetry*, Springer, 2008, pp. 17-38.

[92] C. M. Fancher, S. Brewer, C. C. Chung, S. Röhrig, T. Rojac, G. Esteves, M. Deluca, N. Bassiri-Gharb and J. L. Jones, “Contribution of 180° Domain Wall Motion to Dielectric Properties Quantified from in situ X-Ray Diffraction,” *Acta Materialia,* vol. 126, pp. 36-43, 2017.

[93] S. Park and T. Shrout, “Characteristics of Relaxor-Based Piezoelectric Single crystals for Ultrasonic Transducers,” *IEEE Ultrassonic symposium,* pp. 935-942, 1996.

[94] G. A. Smolenski, V. A. Isupov, A. I. Agranovskaya and N. N. Krainik, "New ferroelectrics of complex composition," *Sov. Phys. Solid State (Engl. Translated),* vol. 2, no. 196, p. 2561, 1961.

[95] T. Granzow, T. Woike, M. Wöhlecke, M. Imlau and W. Kleemann, "Change from 3D-Ising to random field-Ising-model criticality in a uniaxial relaxor ferroelectric.," *Physical review letters,* vol. 92, no. 6, pp. 065701 (1-4), 2004.

[96] K. Uchino, Piezoelectric actuators and ultrasonic motors, vol. 1, Kluwer Academic Publishers, 1997.

[97] M. Miller, E. J. Sharp, G. Wood and R. R. Neugaonkar, "Time response of a cerium-doped $Sr_{0.75}Ba_{0.25}Nb_2O_6$ self-pumped phase-conjugate mirror," *Optcis Letters,* vol. 12, no. 5, pp. 340-342, 1987.

[98] A. A. Bokov and Z. -G. Ye, "Recent progress in relaxor ferroelectrics with perovskite structure," *Journal of Materials Science,* vol. 41, pp. 31-52, 2006.

[99] J. H. Park, K. S. Hong and S. J. Park, "Frequency dependence of the phase transition in $Pb(Mg_{1/3}Nb_{2/3})O_3$-$PbTiO_3$ relaxor ferroelectrics," *Ferroelectrics,* vol. 173, no. 1, pp. 191-206, 1995.

[100] J. Kreisel, B. Dkhil, P. Bouvier and J. -M. Kiat, "Effect of high pressure on relaxor ferroelectrics," *Physical Review B,* vol. 65, pp. 1-4, 2002.

[101] C. Caranoni, N. Menguy, B. Hilczer, M. Glinchuk and V. Stephanovich, "The nature of different behaviour of PSN and PST relaxors," *Ferroelectrics,* vol. 240, pp. 241-248, 2000.

[102] K. Okazaki, H. Igarashi, K. Nagata and A. Hasegawa, "Effects of grain size on the electrical properties of PLZT ceramics," *Ferroelectrics,* vol. 56, no. 2, pp. 82-87, 1974.

[103] H. Graetsch, "Changes of the crystal structure at the relaxor ferroelectric phase transition of strontium barium niobate (SBN53)," *Crystal Research and Technology,* vol. 49, no. 1, pp. 63-69, 2014.

[104] B. Noheda, D. E. Cox, G. Shirane, J. Gao and Z. -G. Ye, "Phase diagram of the ferroelectric relaxor (1-x)$PbMg_{1/3}Nb_{2/3}$-x$PbTiO_3$," *Physical Review B,* vol. 66, no. 5, pp. 054104 (1-10), 2002.

[105] G. A. Smolenskii, "Physical phenomena in ferroelectrics with diffuse phase transitions," *J. Phys. Soc. Jpn.,* vol. 28, no. 26, p. (Supl.), 1970.

[106] L. E. Cross, "Relaxor Ferroelectrics," in *Ferroelectrics*, vol. 76, 1987.

[107] R. E. Cohen, "First-Principles Theories of Piezoelectric Materials," in *Piezoelectricity*, vol. 114, Springer Series in Materials Science, 2008, pp. 471-492.

[108] G. Burns and F. H. DAcol, “Crystalline ferroelectrics with glassy polarization behavior,” *Physical Review B,* vol. 28, p. 2527, 1983.

[109] P. N. Timonin, “Dipole-glass concept and history-dependent phenomena in relaxors,” p. 9, 2010.

[110] M. D. Glinchuk and R. Farhi, “A random field theory based model for ferroelectric relaxors,” *Journal Physics: Condensed Matter,* vol. 8, pp. 6985-6996, 1996.

[111] W. Dmowski, S. B. Vakhrushev, I. K. Jeong, M. P. Hehlen, F. Trouw and T. Egami, “Local lattice dynamics and the origin of the relaxor ferroelectric behavior,” *Physical Review Letters,* vol. 100, no. 13, pp. 1-4, 2008.

[112] V. Bobnar and Z. Kutnjak, “Does Burns temperature exist in ferroelectric relaxors?,” *Ferroelectrics,* vol. 415, no. 1, pp. 14-19, 2011.

[113] M. Alguero, J. M. Gregg and L. Mitoseriu, Nanoscale Ferroelectric and Multiferroics: Key Processing and Characterization Issues, and Nanoscale Effects, vol. 1, Wiley, 2016.

[114] M. Roth, E. Mojaev, E. Dul'kin, P. Gemeiner and B. Dkhil, “Phase transition at a nanometer scale detected by acoustic emission within the cubic phase $Pb(Zn_{1/3}Nb_{2/3})O_3$-$xPbTiO_3$ relaxor ferroelectrics,” *Physical Review Letters,* vol. 98, no. 26, pp. 1-4, 2007.

[115] B. Dkhil, P. Gemeiner, A. Al-Barakaty, L. Bellaiche, E. Dul’kin, E. Mojaev and M. Roth, “Intermediate temperature scale T* in lead-based relaxor systems,” *Physical Review B,* vol. 80, no. 6, pp. 064103 (1-6), 2009.

[116] S. B. Vakhrushev, B. E. Kvyatkovsky, NaberezhnovA. A., N. M. Okuneva and B. P. Toperverg, “GLASSY PHENOMENA IN DISORDERED PEROVSKITE-LIKE CRYSTALS,” *Ferroelectircs,* vol. 90, pp. 173-176, 1989.

[117] Vakhrushev, S.; Nabereznov, A.; Sinha, S. K.; Feng, Y. P.; Egami, T.;, “Synchrotron X-Ray Scattering Study of Lead Magnoniobate Relaxor Ferroelectric Crystals,” *Journal of Physics and Chemistry of Solids,* vol. 57, pp. 1517-1523, 1996.

[118] G. Xu, G. Shirane, J. R. D. Copley and P. M. Gehring, “Neutron elastic diffuse scattering study of Pb(Mg1/3Nb2/3)O3,” *Physical Review B,* vol. 69, no. 9, p. 092105, 2004.

[119] C. Stock, R. Birgeneau, S. Wakimoto, J. S. Gardner, W. Chen, Z. -G. Ye and G. Shirane, “Universal static and dynamic properties of the structural transition in Pb(Zn1/3Nb2/3)O3,” *Physical Review B,* vol. 69, no. 21, pp. 094104 (1-10), 2004.

[120] G. Xu, “Probing local polar structures in PZN- x PT and PMN- x PT relaxor ferroelectrics with neutron and x-ray scattering,” *Journal of Physics: Conference Series,* vol. 320, no. 012081, pp. 1-10, 2011.

[121] A. Bokov, “Influence of disorder in crystal structure on ferroelectric phase transition,” *Journal of Experimental and Theoretical Physics,* vol. 84, pp. 994-1002, 1997.

[122] M. Glinchuk and R. Farhi, “A random field theory based model for ferroelectric relaxors,” *J. Phys.: Condens. Matter,* vol. 8, pp. 6985-6996, 1996.

[123] V. Westphal, W. Kleemann and M. Glinchuk, “DifFuse Phase Transitions and Random-Field-Induced Domain States of the "Relaxor" Ferroelectric PbMg1/3Nb2/303,” *Physical Review Letters,* vol. 68, no. 6, pp. 847-850, 1992.

[124] N. Mathan, E. Husson, G. Calvarn, J. R. Gavarri, A. W. Hewat and A. Morell, “A structural model for the relaxor PbMg1/3Nb2/3O3 at 5 K,” *Journal of Physics: Condensed Matter,* vol. 3, no. 42, p. 8159, 1991.

[125] V. A. Isupov, “Ferroelectric and Antiferroelectric perovskites PbB'o.5B"0.5O3,” *Ferroelectrics,* vol. 289, no. 131, 2003.

[126] V. Westphal, W. Kleemann and M. D. Glinchuk, “Diffuse Phase Transitions and Random-Field-Induced Domain States of the "Relaxor" Ferroelectric PbMg1/3Nb2/3O3,” *Physics Review Letters,* vol. 68, pp. 847-850, 10 February 1992.

[127] Y. Imry and S. Ma, “Random-Field Instability of the Ordered State of Continuous Symmetry,” *Physical Review Letters,* vol. 35, no. 21, pp. 1399-1401, 1975.

[128] V. M. Ishchuk, “Was it necessary to introduce the notion "relaxor ferroelectrics"? The problem of phase transitions in (Pb,Li-1/2-La-1/2)(Zr,Ti)O-3, (Pb,La)(Zr,Ti)O-3, Pb(Mg1/3Nb2/3)O-3, Pb(In1/2Nb1/2)O-3. And related materials. 1. Model conceptions,” *Ferroelectrics,* vol. 255, no. 1, pp. 73-109, 2001.

[129] R. E. Cohen, “Origin of ferroelectricity in perovskite oxides,” *Nature,* vol. 358, pp. 136-138, 1992.

[130] P. N. Timonin, “Griffith's phase in dilute ferroelectrics,” *Ferroelectrics,* vol. 199, no. 1, pp. 69-81, 1997.

[131] T. Egami, “Atomistic mechanism of relaxor ferroelectricity,” *Ferroelectrics,* vol. 267, no. 1, pp. 101-110, 2010.

[132] V. Botvun, S. Kamba, A. Pashkin, M. Savinov, P. Samoukhina, J. Petzelt, I. P. Bykov and M. D. Glinchuk, “Central-Peak Components and Polar Soft Mode in Relaxor PbMg1/3Nb2/3O3 Crystals,” *FErroelectrics,* vol. 298, no. 1, pp. 23-20, 2004.

[133] “Lorentz-type relationship of the temperature dependent dielectric permittivity in ferroelectrics with diffuse phase transition,” *Applied Physics Letters,* vol. 93, pp. 112906 (1-3), 2008.

[134] J. Wu and Q. Jia, “The heterogeneous energy landscape expression of KWW relaxation,” *Scientific Reports,* vol. 6, no. 20506, pp. 2-11, 16 Feb 2016.

[135] A. E. Glazounov and A. K. Tagantsev, “Direect evidence for Vögel-Fulcher freezing in relaxor ferroelectrics,” *Applied Physics Letters,* vol. 73, no. 6, pp. 856-858, 1998.

[136] M. Pechini.U. S. Patent 330 697, 11 July 1967.

[137] P. A. Lessing, “Mixed-Cation Oxide Powders via Polymeric Precursors,” *Ceramic bulleting,* vol. 68, no. 5, pp. 1002-1007, 1989.

[138] E. B. Araujo, B. O. Nahime, M. Melo, F. Dinelli, F. Tantussi, P. Baschieri, F. Fuso and M. Allegrini, “Processing and structural properties of random oriented lead lanthanum zirconate thin films,” *Materials Research Bulletin,* vol. 61, pp. 26-31, 2015.

[139] D. B. Mitzi, L. L. Kosbar, C. E. Murray, M. Copel and A. Afzali, “High-mobility ultrathin semiconducting films prepared by spin coating,” *Nature,* vol. 428, pp. 299-303, 18 March 2004.

[140] M. D. Tyona, “A theoretical study on spin coating technique,” *Advances in Materials Research,* vol. 2, pp. 195-208, 2013.

[141] H. M. Rietveld, *Acta Crystallogr.,* vol. 22, p. 151, 1967.

[142] Y. Zhao and J. Zhang, “Microstrain and grain-size analysis from diffraction peak width and graphical derivation of high-pressure thermomechanics,” *Applied Crystallography,* vol. 41, pp. 1095-1108, 2008.

[143] Y. T. Prabhu, K. V. Rao, V. S. S. Kumar and B. S. Kumari, “X-ray Analysis by Williamsin-Hall and Size-Strain Plot Methods of ZnO Nanoparticles with Fuel Variation,” *World Journal of Nano Science And Engineering,* vol. 4, pp. 21-28, 2014.

[144] G. K. Williamson and W. H. Hall, *Acta Metall.,* vol. 1, 1953.

[145] K. D. Vernon-Parry, “Scanning electron microscopy: an introduction,” *Analysis,* vol. 13, no. 4, pp. 40-44, 2000.

[146] A. Herpes, “Electrical characterization of manganite and titanate heterostructures,” Jülich, 2014, p. 165.

[147] P. Güthner and K. Dransfeld, “Local poling of ferroelectric polymers by scanning force microscopy,” *Applied Physics Letters,* vol. 61, pp. 1137 (1-9), 1992.

[148] F. Johann, Y. J. Ying, T. Jungk, A. Hoffmann, C. L. Sones, R. W. Eason, S. Mailis and E. Soergel, “Depth resolution of piezoresponse force microscopy,” *Applied Physics Letters,* vol. 94, no. 17, pp. 3-5, 2009.

[149] N. Balke, I. Bdikin, S. V. Kalinin and A. L. Kholkin, “Electromechanical imaging and spectroscopy of ferroelectric and piezoelectric materials: State of the art and prospects for the future,” *J. Am. Ceram. Soc.,* vol. 92, pp. 1629-1647, 2009.

[150] S. Hong, J. Woo, H. Shin, J. U. Jeon, E. Pak, E. Colla, N. Setter, E. Kim and K. No, "Principle of ferroelectric domain imaging using atomic force microscope," *Journal of Applied Physics,* vol. 89, no. 2, pp. 1377-1386, 2001.

[151] S. V. Kalinin, B. J. Rodriguez, S. Jesse, P. Maksymovich, K. Seal, M. Nikiforov, A. P. Baddorf, A. Kholkin and R. Proksch, "Local bias-induced phase transitions," *Mater. Today,* vol. 11, pp. 16-27, 2008.

[152] S. Jesse, A. P. Baddorf and V. Kalinin, "Switching spectroscopy piezoresponse force microscopy of ferroelectric materials," *Applied Physics Letters,* vol. 88, p. 062908, 2006.

[153] V. Shvartsman, A. Kholkin, M. Tyunina and J. Levoska, "Relaxation of Induced Polar State in Relaxor PbMg1/3Nb2/3O3 Thin Films studied by Piezoresponse Force Microscopy.," *Applied Physisc Letters,* Vols. 86, 222907, 2005.

[154] M. Cohen and G. Grest, "Dispersion of relaxation rates in dense liquid and glasses," *Physical Review B,* vol. 24, no. 7, pp. 4091-4094, 1981.

[155] D. J. Taylor, P. F. Fleig and S. L. Hietala, "Technique for Characterization of Thin Film Porosity," *Thin Solid Films,* vol. 332, pp. 257-261, 1998.

[156] A. Garahan, L. Pilon and J. Yin, "Effective Optical Properties of Absorbing Nanoporous and Nanocomposite Thin Films," *Journal Of Applied Physics,* vol. 101, pp. 014320(1-9), 2007.

[157] T. S. Dorofeeva and E. Seker, "Electrically Tunebla Pore Morphologu in Nanoporous Gold thin Films," *Nano Research,* vol. 8, pp. 2188-2198, 2015.

[158] N. Sultana and T. H. Khan, "Water Absorption and Diffusion Characteristics of Nanohydroxyapatite (nHA) and Poly(hydroxybutyrate-co-hydroxyvalerate-) Based Composite Tissue Engineering Scaffolds and Nonporous Thin Films," *Journal of Nanomaterials,* pp. 1-8, 2013.

[159] M. M. Braun and L. Pilon, "Effective Optical Properties of Non-absorbing Nanoporous Thin Films," *Thin Solid Films,* vol. 496, pp. 505-514, 2006.

[160] A. Navid and L. Pilon, "Effect of polarization and morphology on the optical properties of absorbing nanoporous thin films," *Thin sild Films,* vol. 516, pp. 4159-4167, 2008.

[161] C. Fan, J. P. Celis and J. R. Ross, "Effect of Substrate Pretreatment on the Porosity in Thin Nickel Electrodeposits," *Surface and Coatings Technology,* vol. 50, pp. 289-294, 1992.

[162] E. S. Toberer, M. Grossman, T. Schladt , F. F. Lange and R. Seshadri, "Epitaxial Manganese Oxide Thin Films with Connected Porosity: Topotatic Induction of Crystallografic Pore Alignment," *Chemistry of Materials,* vol. 19, pp. 4833-4838, 2 October 2007.

[163] S. Nakahara, “Microporosity Induced By Nucleatiion and Growth Processes in Crystalline and Non-Crystalline Films,” *Thin Solid Films,* vol. 45, pp. 421-432, April 1977.

[164] S. Ganesamoorthy, I. Bhaumik, R. Bhatt, A. K. Karnal, P. K. Gupta, S. Kumaragurubaran, R. Mohankumar, K. Kitamura, S. Takekawa and M. Nakamura, “A comparative study of dielectric relaxation in Sr.0.61Ba0.39Nb2O6 e Sr0.75Ba0.25Nb2O6 single crystals,” *Japanese Journal of Applied Physics,* vol. 47, pp. 1012-1015, 2008.

[165] A. Inforturna, P. Muralt, M. Cantoni, A. Tagantsev and N. Setter, “Microstructural and electrical properties of (Sr, Ba)Nb2O6 thin films grown by pulsed laser deposition,” *Journal of the european Ceramic Society,* vol. 24, pp. 1573-1577, 2004.

[166] C. Ellisalde and J. Ravez, “Relaxation mechanisms in Sr0.3Ba0.7Nb2O6,” *Journal of Materials Chemistry,* vol. 10, pp. 681-683, 2000.

[167] N. S. VanDamme, A. E. Sutherland, L. Jones, K. Bridger and S. R. Winzer, “Fabrication of optically transparent and electrooptic strontium barium niobate ceramics,” *Journal of the American Ceramic Society,* vol. 74, no. 8, pp. 1785-1792, 1991.

[168] C. Ang, Z. Yu and L. E. Cross, “Oxygen-Vacancy-Related Low-Frequency Dielectric Relaxation and Electrical Conduction in Bi:SrTiO3,” *Phys. Rev. B,* vol. 62, no. 1, p. 228, 1 July 2000.

[169] J. Li, Y. Pu, Z. Wang and J. Dai, “A comparative study of Sr0.7Ba0.3Nb2O6 relaxor ferroelectric ceramics prepared by conventional and microwave sintering techniques,” *Ceramics International,* vol. 39, pp. 5069-5075, 2013.

[170] G. A. Samara and E. L. Venturini, “Ferroelectric/Relaxor Crossover in Compositionally Disordered Peroviskites,” *Phase Transitions: A Multinational Journal,* vol. 79, pp. 21-20, 1 February 2007.

[171] V. V. Shvartsman and D. C. Lupascu, “Lead-Free Relaxor Ferroelectrics,” *J. Am. Ceramic. Soc.,* vol. 95, no. 1, pp. 1-26, 2012.

[172] H. Gui, B. Gu and X. Zhang, “Distribution of relaxation times in perovskite-type relaxor ferroelectrics,” *J. Appl. phys.,* vol. 78, p. 3, 1995.

[173] M. Delgado, E. V. Colla, P. Griffin and M. B. Weissman, “Field dependencce of glassy freezing in a relaxor ferroelectric,” *Physical Review B,* vol. 79, pp. 140102 (1-6), 2009.

[174] A. K. Tagantsev, “Vogel-Fulcher Relationship for the Dielectric Permittivity of Relaxor Ferroelectrics,” *Physical Review Letters,* vol. 72, pp. 7-14, 14 February 1994.

[175] A. Bokov and Z. Ye, “Double freezing of dielectric response in relaxor Pb(Mg1/3Nb2/3)O3 crystals,” *Physical Review B,* vol. 74, pp. 132102 (1-4), 2006.

[176] J. A. Gonzalo, “Effective Field Approach to Phase Transitions and Some Applications so Ferroelectrics,” *World Scientific Lecture Notes in Physics,* vol. 35, 1991.

[177] P. R. Das, B. Pati, B. C. Sutar and R. N. P. Choudhury, “Study of Structural and Electrical Properties of a New Type of Complex Tungsten Bronze Electroceramics; Li2Pb2Y2W2Ti4V4O30,” *Journal of Modern Physics,* vol. 3, pp. 870-880, 2012.

[178] T. Badapanda, R. K. Harichandan, S. S. Nayak, A. Mishra and S. Anwar, “Frequency and temperature dependence behaviour of impedance, modulus and conductivity of BaBi4Ti4O15 Aurivillius ceramic,” *Processing and Application of Ceramics,* vol. 8, no. 3, pp. 145-153, 2014.

[179] A. K. Tagantsev and A. E. Glazounov, “Mechanism of Polarization Response in the Ergodic Phase of a Relaxor Ferroelectric,” *Physical Review B,* vol. 57, pp. 18-21, September 1997.

[180] H. Yan, F. Inam, G. Viola, H. Ning, H. Zhang, Q. Jiang, T. Zenh, Z. Gao and M. Reece, “The Contribution of electrical Conductivity, Dielectric Permittivity, And Domain Switching In Ferroelectric Hysteresis Loops,” *Journal of Advanced Dielectrics,* vol. 1, pp. 107-118, 2011.

[181] J. Dec, W. Kleemann, V. Shvartsman, D. C. Lapascu and T. Łukasiewicz, “From mesoscopic to global polar order in the uniaxial relaxor ferroelectric Sr0.8Ba0.2Nb2O6,” *Applied Physics Letters,* vol. 100, pp. 052903 (1 - 4), 2012.

[182] V. V. Shvartsman and W. Kleemann, “Evolution of nanodomains in the uniaxial relaxor Sr0.61Ba0.39Nb2O6:Ce,” *IEEE Transactions on Ultrasonins Ferroelectrics and Frequency Control,* vol. 53, pp. pp. 2275-2279, 2006.

[183] J. R. Oliver, R. R. Neurgaonkar and L. E. Cross, “A Thermodynamic Phenomenology for Ferroelectric Tungsten Bronze Sr0.6Ba0.4Nb2O6 (SBN:60),” *Journal of Applied Physics,* vol. 64, pp. 37-47, 1988.

[184] A. Gruverman and A. Kholkin, “Nanoscale ferroelectrics: processing, characterization and future trends,” *Rep. Prog. Phys.,* vol. 69, pp. 2443-2474, 2006.

[185] H. Lee, T. H. Kim, J. J. Patzner, H. Lu, J.-W. Lee, H. Zhou, W. Chang, M. K. Mahanthappa, E. Y. Tsymbal, A. gruverman and C.-B. Eom, “Imprint Control of BaTiO3 Thin Films via Chemically Induced Surface,” *American Chemical Society: Nanoletters,* vol. 16, pp. 2400-2406, 2016.

[186] J. Karthick, R. K. Mangalam, J. C. Agar and L. M. Martin, “Large Built-in electric Fields due to Flexoelectricity in Compositionally Graded Ferroelectrc Thin films,” *Physical Reviw B,* vol. 87, pp. 1-6, 2013.

[187] M.-G. Han, M. S. Marschall, L. Wu, M. A. Schofield, T. Aoki, R. Twesten, J. Hoffman, F. J. Walker, C. H. Ahn and Y. Zhu, “Interface-induced nonswitchable domains in ferroelectric thin film,” *Nature Communications,* vol. 5, pp. 1-9, 18 Aug 2014.

[188] V.-c. Lo, W. W.-y. Chung, H. Cao and X. Dai, “Investigating the Effect of Oxygen Vacancy on the Dielectric and Electromechanical Propereties in Ferroelectric Ceramics,” *Journal of Applied Physics,* vol. 6, pp. 064105 (1-6), 18 Sept 2008.

[189] T. Chien, J. Liu, A. J. Yost, J. Chakhalian, J. W. Freeland and N. P. Guisinger, “Built-in electric Field Induced Mechanical Property Change at the Lanthanum Nickelate/Nb-Doped Strontion Titatnate Interfaces.,” *Scientific Reports,* vol. 6, pp. 1-9, 2016.

[190] R. Pirc and R. Blinc, “Spherical Random-bond-random-field Model of Relaxor Ferroelectrics,” *Physical Review B,* vol. 60, pp. 12470-13478, 1999.

[191] A. Wu, P. M. Vilarinho , V. V. Shvartsman, G. Suchaneck and A. L. Kholkin, “Domain populations in lead zirconate titanate thin films of different compositions via piezoresponse force microscopy,” *Nanotechnology,* vol. 16, no. 11, pp. 2587-2595, 2005.

[192] A. Gruverman, O. Auciello and H. Tokumoto, “Imaging and control of domains structures in ferroelectric thin films via scanning force microscopy,” *Annual Review Material Science,* vol. 28, pp. 101-123, 1998.

[193] J. Dec, V. V. Shvartsman and W. Kleemann, “Domainlike precursos clusters in the paraelectruc phase of the uniaxial relaxor Sr0.61Ba0.39Nb2O6,” *Applied Physics Letters,* vol. 89, no. 21, pp. 212901(1-3), 2006.

[194] A. Gannepalli, D. G. Yablon, A. H. Tsou and R. Proksch, “Mapping nanoscale elasticity and dissipation using dual frequency contact resonance AFM,” *Nanotechnology,* vol. 22, no. 355705, 2011.

[195] K. Yamanaka and S. Nakano, “Quantitative Elasticity Evaluation by Contact Resonance in an Atomic Force Microscope,” *Applied Physics A: Materials Science & Processing,* vol. 66, pp. S313-S317, 1 October 1998.

[196] N. A. Burnham, A. J. Kulik, G. Gremaud, P. -J. Gallo and F. Oulevey, “Scanning Local-acceleration Microscopy,” *Journal of Vacuum Science & Technology B: Microelectronics and Nanometer Structures,* vol. 14, no. 2, 1996.

[197] R. Proksch and S. V. Kalinin, *Piezoresponse Force Microscopy with Asylum Research AFMs,* St. Barbara, Ca, 2010, p. 24 pp..

[198] V. Nagarajan and A. Gruverman, “Nanoscale Polarization Relaxation in a Polycristalline Feroelectric Thin Film: Role of Local Environments,” *Applied Physics Letters,* vol. 86, no. 262910, pp. 1-3, 2005.

[199] A. Kholkin, K. Brooks , D. Taylor, S. Hiboux and N. Setter, “Self-polarization Effect in Pb(Zr, Ti) thin films,” *Integrated Ferroelectrics,* vol. 22, pp. 525-533, 1998.

[200] A. Gruverman, A. L. Kholkin , A. Kingon and H. Tokumoto, “Asymmetric nanoscale switching in ferroelectric thin films by scanning force microscopy,” *Applied Physics Letters,* vol. 78, no. 18, pp. 2751-2753, 2001.

[201] M. Melo, E. B. Araujo, A. P. Turygin, V. Y. Shur and A. L. Kholkin, "Physical properties of strontium barium niobate thin films prepared by polymeric chemical method," *Ferroelectrics,* vol. 496, January 2016.

[202] V. V. Shvartsman and A. L. Kholkin, "Spontaneous and induced surface piezoresponse in PbMg1/3Nb2/3O3 single crystals," *Z. Kristallogr.,* vol. 226, pp. 108-112, 2011.

[203] Y. Zhou, H. K. Chan, C. H. Lam and F. G. Shin, "Mechanism of Imprint Effect on Ferroelectric Thin Films," *Journal of Applied Physics,* vol. 98, no. 2, pp. 1-9, 2005.

[204] R. Ahluwalia and D. Srolovitz, "Size Effects in Ferroelectric thin film: 180º domains and Polarization Relaxation," *Physical Review B - Condensed Matter and Materials Physics,* vol. 76, no. 17, pp. 1-5, 2007.

[205] D. J. Kim, J. Y. Jo, Y. S. Kim, Y. J. Chang , J. S. Lee, J. G. Yoon, T. K. Song and T. W. Noh, "Polarization relaxation induced by a depolarization field in ultrathin ferroelectric BaTiO3 capacitors," *Physical Review Letters,* vol. 95, no. 23, pp. 1-4, 2005.

[206] R. R. Mehta, B. D. Silverman and J. T. Jacobs, "Depolarization fields in thin ferroelectric films," *Journal of Applied Physics,* vol. 44, no. 8, pp. 3379-3385, 1973.

[207] X. Y. Liu, Y. M. Liu, S. Takekawa, K. Kitamura, F. S. Ohuchi and J. Y. Li, "Nanopolar structures and local ferroelectricity of Sr0.61Ba0.39Nb2O6 relaxor crystal across curie temperature by piezoresponse force microscopy," *Journal of Applied Physics,* vol. 106, pp. 124106-124113, 2009.

[208] V. V. Efimov, E. A. Efimova, K. Iakoubovskii, S. Khasanov, D. I. Kochubey, V. V. Kriventsov, A. Kuzmin, B. N. Mavrin, M. Sakharov, V. Sikolenko, A. N. Shmakov and S. I. Tiutiunnikov, "EXAFS, X-ray diffraction and Raman studies of (Pb1-xLax)(Zr0.65Ti0.35)O3 (x = 0.04 and 0.09) ceramics irradiated by high-current pulsed electron beam," *Journal of Physics and Chemistry of Solids,* vol. 67, no. 9-10, pp. 2007-2012, 2006.

[209] B. H. Toby, "R factors in Rietveld analysis: How good is good enough?," *Powder Diffraction,* vol. 21, no. 01, pp. 67-70, 2006.

[210] G. Leclerc, B. Domengès, G. Poullain and R. Bouregba, "Elaboration of (111)-oriented La-doped PZT thin films on platinized silicon substrates," *Applied Surface Science,* vol. 253, pp. 1143-1149, 2006.

[211] S. Hoboux and P. Muralt, "Mixed titania-lead oxide seed layers for PZT growth on Pt(111): a study on nucleation, texture and properties," *Journal of the European Ceramic Society,* vol. 24, no. 6, pp. 1593-1596, 2004.

[212] G. Leclerc, G. Poullain, C. Yaicle, R. Bouregba and A. Pautrat, "Substrate and orientation influence on electrical properties of sputtered La-doped PZT thin films," *Applied Surface Science,* vol. 254, pp. 3867-3872, 2008.

[213] Z. J. Wang, R. Maeda and K. Kikuchi, “Development of phases and texture in sol-gel derived lead zirconate titanate thin films prepared by three-step heat-treatment process,” *Journal of Materials Science,* vol. 35, no. 23, pp. 5915-5919, 2000.

[214] T. Manjulavalli and A. Kannan, “Structural and optical properties of ZnS thin films prepared by chemical bath deposition method,” *Int. J. New. Hor. Phys.,* vol. 8, no. 11, pp. 396-402, 2015.

[215] A. M. El-Shabiny, G. A. El-Shobaky, I. F. Hewaidy and A. A. Ramadan, “Microstrain and lattice parameter of pure and Li2O-doped nickel oxide solid,” *Crystal Research and Technology,* vol. 23, no. 7, pp. 911-917, 1988.

[216] M. N. Pham, B. A. Boukamp, G. Runders, H. Bouwmeester and D. H. A. Blank, “Pulsed laser deposition of PZT/Pt composite thin films with high dielectric constants,” *Appl. Phys. A: Materials Science & Processing,* vol. 79, pp. 907-910, 2004.

[217] N. Tohge, E. Fujii and T. Minami, “Ferroelectric properties of PLZT films prepared by the sol-gel process using chemically modified metal-alkoxides,” *Journal of Materials Science: Materials in Electronics,* pp. 356-359, 1994.

[218] C. Li, Ö. Dag, T. D. Dao, T. Nagao, Y. Sakamoto, T. Kimura, O. Terasaki and Y. Yamauchi, “Electrochemical synthesis of mesoporous gold films toward mesospace-stimulated optical properties,” *Nature Communications,* vol. 6, pp. 6608-6616, 2015.

[219] A. Castro, P. Ferreira, B. J. Rodriguez and P. M. Vilarinho, “The role of nanoporosity on the local piezo and ferroelectric properties of lead titanate thin filmes,” *J. Mater. Chem. C,* vol. 3, p. 9, 2015.

[220] M. Karayianni and S. Pispas, “Self-Assembly of Amphiphilic Block Copolymers in Selective Solvents,” in *Fluorescence Studies of Polymer Containing Systems*, vol. 16, Springer Series on Fluorescence, 2016, pp. 27-64.

[221] N. Erdman, R. Campbell and S. Asahina, “Precise SEM Cross Section Polishing via Argon Beam Milling,” *Microscopy Today,* pp. 22-25, May 2006.

[222] G. Bertotti, I. D. Mayergoyz and D. Damjanovic, “Hysteresis in Piezoelectric and Ferroelectric Materials,” *The science of hysteresis,* vol. 1, pp. 337-465, 2006.

[223] V. Koval, G. Viola and Y. Tan, “Biasing Effects in Ferroic Materials, Ferroelectric Materials - Synthesis and Characterization,,” Dr. Aimé Peláiz-Barranco (Ed.), InTech, 2015.

[224] V. Bornand, S. Trolier-McKinstry, K. Takemura and C. Randall, “Orientation dependence of fatigue behavior in relaxor ferroelectric–PbTiO[sub 3] thin films,” *Journal of Applied Physics,* vol. 87, no. 8, pp. 3965(1-8), 2000.

[225] Y. Genenko, M. Glaum, M. J. Hoffmann and Albek., “Mechanisms of aging and fatigue in ferroelectrics,” *Materials Science and Engineering B: Solid-State Materials for Advanced Technology,* vol. 192, no. C, pp. 52-82, 2015.

[226] M. Ozgul, K. TAkemura, S. Trolier-McKinstry and C. Randall, “Polarization fatigue in Pb(Zn1/3Nb2/3)O3-PbTiO3 ferroelectric single crystals,” *Journal of Applied Physics,* vol. 89, no. 9, pp. 5100-5106, 2001.

[227] E. Fatuzzo and W. J. Merz, “Switching mechanism in Triglycine and other ferroelectrics,” *Physical Review,* vol. 116, p. 8 pp., October 1959.

[228] A. S. Sidorkin, L. Nesterenko, S. Ryabtsev and A. A. Sikorkin, “Frequency dependence of the coercive field and the internal bias field in ferroelectric thin films,” *Physics of the Solid State,* vol. 51, no. 7, pp. 1348-1350, 2009.

[229] M. H. Lente, A. Picinin, J. P. Rino and J. A. Eiras, “90° domain wall relaxation and frequency dependence of the coercive field,” *Journal of Applied Physics,* vol. 95, no. 5, pp. 2646-2653, 2003.

[230] M. Dawber, P. Chandra, P. B. Littlewood and J. F. Scott, “Depolarization corrections to the coercive field in thin-film ferroelectrics,” *Journal of Physics: Condensed Matter,* vol. 15, no. 24, pp. L393-L398, 2003.

[231] V. Fridkin and S. Ducharme, “General features of the intrinsec ferroelectric coercive fields,” *Physics of the Solid State,* vol. 43, no. 7, pp. 1320-1324, 2001.

[232] S. S. N. Bharadwaja, J. R. Kim, H. Ogihara, L. E. Cross, S. Trolier-McKinstry and C. Randall, “Critical slowing downmechanism and reentrant dipole glass phenomena in (1− x)BaTiO3-xBiScO3 (0.1 < x < 0.4): The high energy density dielectrics,” *Physical Review B - Condensed Matter and Materials Physics,* vol. 83, no. 2, pp. 1-9, 2011.

[233] H. Y. Guo, C. Lei and Z. G. Ye, “Re-entrant type relaxor behavior in (1-x) BaTiO3 - xBiScO 3 solid solution,” *Applied Physics Letters,* vol. 92, no. 17, pp. 17-20, 2008.

[234] C. Lei and Z. G. Ye, “Re-entrant-like relaxor behaviour in the new 0.99BaTiO3–0.01AgNbO3 solid solution,” *J. Phys.: Condens. Matter,* vol. 20, no. 232201, pp. 1-4, 2008.

[235] S. S. N. Bharadwaja, J. Kim, H. Ogihara, L. E. Cross, S. Trolier-Mckinstry and C. A. Randall, “Critical slowing downmechanism and reentrant dipole glass phenomena in (1− x)BaTiO3-xBiScO3 (0.1 < x < 0.4): The high energy density dielectrics,” *Physical Review B - Condensed Matter and Materials Physics,* vol. 83, no. 2, pp. 1-9.

[236] C. J. Huang, K. Li, S. Y. Wu, X. L. Zhu and X. M. Chen, “Variation of ferroelectric hysteresis loops with temperature in (SrxBa1-x)Nb2O6 unfilled tungstein bronze ceramics,” *Journal of Materiomics,* vol. 1, pp. 146-152, 2015.

[237] Y. Su and C. Landis, “Continuum thermodynamics of ferroelectric domain evolution: Theory, finite element implementation, and application to domain wall pinning,” *Journal of the Mechanics and Physics of Solids,* vol. 55, no. 2, pp. 280-305, 2007.

[238] A. Belov and W. Kreher, “Simulation of microstructure evolution in polycrystalline ferroelectrics-ferroelastics,” *Acta Materialia,* vol. 54, no. 13, pp. 3463-3469, 2006.

[239] M. Avrami, “Kinetics of Phase Change. I - General Theory,” *The Journal of Chemical Physics,* vol. 7, no. 12, pp. 1103-1114, 1939.

[240] K. Chong, F. Guiu and M. Reece, “Thermal activation of ferroelectric switching,” *Journal of Applied Physics,* vol. 103, no. 1, pp. 014101(1-7), 2008.

[241] D. Schrade, R. Mueller, B. X. Xu and D. Gross, “Domain evolution in ferroelectric materials: A continuum phase field model and finite element implementation,” *Computer Methods in Applied Mechanics and Engineering,* vol. 196, no. 41-44, pp. 4365-4374, 2007.

[242] V. Bobnar, Z. Kutnjak, R. Pirc and A. Levstik, “Electric - field - temperature phase diagram of the relaxor ferroelectric lanthanum-modified lead zirconate titanate,” *Physical Review B,* vol. 60, no. 9, pp. 6420-6428, 1999.

[243] C. V. Thompson, “Structure Evolution During Processing of Polycristalline films,” *Annu. Rev. Mater. Sci,* vol. 30, no. 12, pp. 159-190, 2000.

[244] A. Gruverman, “Piezoresponse force microscopy and recent advances in nanoscale studies of ferroelectrics,” *Journal of Materials Science: Frontiers of Ferroelectricity,* vol. 1, no. 1, pp. 1-10, 2006.

[245] L. Xie, Y. L. Li, R. Yu, Z. Y. Cheng, X. Y. Wei, X. Y. Wei, X. Yao, C. L. Jia, K. Urban, A. A. Bokov, Z. -G. Ye and J. Zhu, “Static and dynamic polar nanoregions in relaxor ferroelectric Ba(Ti1-xSnx)O3system at high temperature,” *Physical Review B,* vol. 85, no. 014118, pp. 1-5, 2012.

[246] B. P. Burton, E. Cockayne and U. V. Waghmare, “Correlations between nanoscale chemical and polar order in relaxor ferroelectrics and the lengthscale for polar nanoregions,” *Physical Review B - Condensed Matter and Materials Physics,* vol. 72, no. 6, pp. 2-6, 2005.

[247] L. Tian, A. Vasudevarao, A. N. Morozovska, E. A. Eliseev, S. V. Kalinin and V. Gopalan, “Nanoscale polarization profile across a 180° ferroelectric domain wall extracted by quantitative piezoelectric force microscopy,” *Journal of Applied Physics,* vol. 104, no. 7, pp. 074110 (1-11), 2008.

[248] Z. Kighelman, D. Damjanovic and N. Setter, “Electromechanical properties and self-polarization in relaxor PbMg1/3Nb2/3O3 thin films,” *Journal of Applied Physics,* vol. 89, no. 2, pp. 1393-1402, 2001.

[249] V. P. Afanasjev, A. A. Petrov, I. P. Pronin, E. A. Tarakanov, E. J. Kaptelov and J. Graul, “Polarization and self-polarization in thin PbZr1−xTixO3 (PZT) films,” *J. Phys. Condens. Matter,* vol. 13, pp. 8755-8763, 2001.

[250] E. B. Araujo, E. C. Lima, I. K. Bdikin and A. L. Kholkin, “Thickness dependence of structure and piezoeletric properties at nanoscale of polycrystalline lead zironate titanate thin films,” *Journal of Applied Physics,* vol. 113, p. 187206 (6 pp.), 2013.

[251] E. B. Araujo, E. C. Lima, I. K. Bdikin and A. L. Kholkin, “Imprint effect in PZT thin films at compositions around the morphotropic phase boundary,” *Ferroelectrics,* vol. 498, no. 1, pp. 18-26, 2016.

[252] V. V. Shvatsman, B. Dkhil and A. L. Kholkin, “Mesoscale Domains and Nature of the Relaxor State by Piezoresponse Force Microscopy,” *Annu. Rev. Matter. Res.,* vol. 43, pp. 10.1-10.27, 2013.

[253] R. C. Munoz, Vidal'G., M. Mulsow, J. G. Lisoni, C. Arenas, A. Concha, Mora'F. and R. Espejo, “Surface roughness and surface-induced resistivity of gold films on mica: Application of quantitative scanning tunneling microscopy,” *Physical Review B,* vol. 62, no. 7, pp. 4686-4697, 2000.

[254] D. Kiselev, I. K. Bdikin, E. Selezneva and A. L. Kholkin, “Grain size effect and local disorder in polycrystalline relaxors via scanning probe microscopy,” *Journal of Physics D: Applied Physics,* vol. 40, p. 7109, 2007.

[255] W. L. Li, T. D. Zhang, Y. F. Hou, Y. Zhao, D. Xu, W. P. Cao and W. D. Fei, “Giant piezoelectric properties of BZT–0.5BCT thin films induced by nanodomain structure,” *RSC Adv.,* vol. 4, p. 56933–56937, 2014.

[256] P. Sharma, T. Reece, D. Wu, V. M. Fridkin, S. Ducharme and A. Gruverman, “Nanoscale domain patterns in ultrathin polymer ferroelectric films.,” *Journal of physics. Condensed matter : an Institute of Physics journal,* vol. 21, no. 48, pp. 485902 (1-7), 2009.

[257] A. L. Kholkin, I. K. Bdkin, D. A. Kiselev, V. V. Shvartsman and S. -H. Kim, “Nanoscale characterization of polycrystalline ferroelectric materials for piezoelectric applications,” *J. Electroceram,* vol. 19, pp. pp. 81-94, 2007.

[258] A. Ferri, A. Da costa, S. Saitzek, R. Desfeux, M. detalle, G. S. Wang and D. Remiens, “Local Piezoelectric Hysteresis Loops for the Study of Electrical Properties of 0.7Pb(Mg1/3Nb2/ 3)O3-0.3PbTiO3 Thin Films: Bottom Electrode Dependence and Film Thickness Effect,” *Ferroelectrics,* vol. 362, no. 1, pp. 21-29, 2008.

[259] J. Zhu, X. Zhang, Y. Zhu and S. B. Desu, “Size effects of 0.8SrBi2Ta2O9 – 0.2Bi3TiNbO9 thin films,” *Journal of Applied Physics,* vol. 83, no. 3, pp. 1610-1612, 1998.

[260] Z.-N. Hu and V. C. Lo, “Thickness Dependence of the Coercive Field in Ferroelectric Thin Films,” *International Journal of Modern Phyisics B,* vol. 20, no. 22, pp. 3223-3231, 2006.

[261] W. Cao and C. A. Randall, “Grain size and domain size relations in bulk ceramic ferroelectric materials,” *Journal of Physics and Chemistry of Solids,* vol. 57, no. 10, pp. 1499-1505, 1995.

[262] A. Gruverman, B. J. Rodriguez, R. J. Nemanich and A. I. Kingon, “Nanoscale observation of photoinduced domain pinning and investigation of imprint behavior in

ferroelectric thin films," *Journal of Applied Physics,* vol. 92, no. 5, pp. 2734-2739, 2002.

[263] A. Gruverman, B. J. Rodriguez, A. I. Kingon, R. J. Nemanich, A. K. Tagantsev, J. S. Cross and M. Tsukada , "Mechanical stress effect on imprint behavior of integrated ferroelectric capacitors," *Applied Physics Letters,* vol. 83, no. 4, pp. 728-730, 2003.

[264] M. I. Molotskii and M. M. Shvebelman, "Dynamics of Ferroelectric Domain formation in an atomic force microscopy," *Philosophical Magazine,* vol. 85, no. 15, pp. 1637-1655, 2005.

[265] J. Kim, S. Hong , S. Bühlmann, Y. Kim, M. Park, Y. K. Kim and K. No, "Effect of deposition temperature of TiO2 on the piezoelectric property of PbTiO3 film grown by PbO gas phase reaction sputtering," *Journal of Applied Physics,* vol. 107, pp. 104112 (1-5), 2010.

[266] M. Tyunina, J. Levoska, K. Kundzinsh and V. Zauls, "Polar state in epitaxial films of the relaxor ferroelectric PbMg1/3Nb2/3O3," *Physical Review B,* vol. 69, no. 224101, pp. (1-10), 2004.

[267] A. L. Kholkin, V. V. Shvartsman, M. Woitas and A. Safari, "Local electromechanical properties and grain size effects in ferroelectric relaxors studied bu scanning piezoelectric microscopy," vol. 748, pp. 1-6, 2003.

[268] Y. Choi and S. Suresh, "Size effects on the mechanical properties of thin polycrystalline metal films on substrates," *Acta Materialia,* vol. 50, no. 7, pp. 1881-1893, 2002.

[269] T. Mishima, H. Fujioka, S. Nagakari, K. Kamigaki and S. Nambu, "Lattice image observatins of nanoscale ordered regions in Pb(Mg1/3Nb2/3)O3," *Japanese Journal of Applied Physics,* vol. 36, no. 6141, 1997.

[270] O. N. Bacus, *Estabilização da fase peroviskita e propriedades estruturais de filmes finos relaxores do sismtea PLZT,* Ilha Solteira, 2016, p. 88.

[271] M. Melo, E. B. Araujo, V. V. Shvartsman, V. Y. Shur and A. L. Kholkin, "Thickness effect on the structure , grain size , and local piezoresponse of self-polarized lead lanthanum zirconate titanate thin films," *Journal of Applied Physics,* vol. 054101, pp. 1-7, 2016.

[272] L. Tian, A. Vasudevarao, A. N. Morozovska, E. A. Eliseev, S. V. Kalinin and V. Gopalan, "Quantitative piezoelectric force microscopy: influence of tip shape, size, and contact geometry on the nanoscale resolution of an antiparallel ferroelectric domain wall," *Journal of Applied Physics,* vol. 104, 2008.

[273] R. L. Harrison, "Introduction to Monte Carlo Simulation," in *AIP Conf. Proc.*, 2010.

[274] A. L. Kholkin, C. Tantigate and A. Safari, “Electromechanical properties of PMN-PT thin films prepared by puldes laser deposition technique,” *Integrated ferroelectrics,* vol. 22, no. 1-4, pp. 515-523, 1998.

[275] X. M. Lu, F. Schlaphof, S. Grafström, C. Loppacher, L. M. Eng, G. Suchaneck and G. Gerlach, “Scanning force microscopy investigation of the Pb (Zr 0.25 Ti 0.75) O 3 / Pt interface,” *Applied Physics Letters,* vol. 81, p. 3215, 2002.

[276] K. W. Kwok, B. Wang, H. L. W. Chan and C. L. C. Choy, “Self-polarization in PZT films,” *Ferroelectrics,* vol. 271, pp. 69-74, 2002.

[277] G. C. A. M. Janssen, “Stress and strain in polycrystalline thin films,” *Thin solids Films,* vol. 515, no. 17, pp. 6654-6664, 2007.

[278] J. Curie and P. Curie, “Development, via compression, of electric polarization in hemihedral crystals with inclined faces,” *Bulletin de la Societe de Minerologique de France,* vol. 3, pp. 90-93, 1880.

[279] J. Curie and P. Curie, “Contractions and expansions produced by voltages in hemihedral crystals with inclined faces,” *Comptes Rendus,* vol. 93, pp. 1137-1140, 1881.

[280] B. Jaffe, Piezoelectric Ceramics, London: Academic Press, 1971.

[281] M. Yamada, N. Nada, M. SAitoh and K. Watanabe, “First-order quasi-phase matched LiNbO3 waveguide periodically poled by applying an external field for efficient blue second-harmonic generation,” *Applied Physics Letters,* vol. 62, pp. 435 (1-6), 1993.

[282] D. Fu and M. Itoh, “Ferroelectricity in Silver Perovskite Oxides,” in *Ferroelectrics - Material Aspects*, M. Lallart, Ed., 2011.

[283] J. Gardner and F. Morrison, “A-site size effect in a family of unfilled ferroelectric tetragonal tungsten bronzes: Ba4R0.67Nb10O30(R = La, Nd, Sm, Gd, Dy and Y),” *Dalton Transactions: Royal Society of Chemistry,* vol. 43, pp. 11687-11695, 2014.

[284] P. B. Jamieson, S. C. Abrahams and J. L. Bernstein, “Ferroelectric Tungsten Bronze-Type Crystal Structures. I. Barium Strontium Niobate Ba.0.27Sr0.76Nb2O5.78,” *The Journal of Chemical Physics,* vol. 48, no. 11, pp. 5048-5057, 1 June 1968.